POLYPUBLIE
Polytechnique Montréal

POLYTECHNIQUE MONTRÉAL
UNIVERSITÉ D'INGÉNIERIE

**Titre:** Metrology of Machine Tool Compliance under Quasi-Static Condition
Title:

**Auteur:** Babak Beglarzadeh
Author:

**Date:** 2022

**Type:** Mémoire ou thèse / Dissertation or Thesis

**Référence:** Beglarzadeh, B. (2022). Metrology of Machine Tool Compliance under Quasi-Static Condition [Thèse de doctorat, Polytechnique Montréal]. PolyPublie. https://publications.polymtl.ca/10342/
Citation:

**Document en libre accès dans PolyPublie**
Open Access document in PolyPublie

**URL de PolyPublie:** https://publications.polymtl.ca/10342/
PolyPublie URL:

**Directeurs de recherche:** J. R. René Mayer
Advisors:

**Programme:** PhD.
Program:

**Ce fichier a été téléchargé à partir de PolyPublie, le dépôt institutionnel de Polytechnique Montréal**
This file has been downloaded from PolyPublie, the institutional repository of Polytechnique Montréal

https://publications.polymtl.ca

**POLYTECHNIQUE MONTRÉAL**

affiliée à l'Université de Montréal

# METROLOGY OF MACHINE TOOL COMPLIANCE UNDER QUASI-STATIC CONDITION

**BABAK BEGLARZADEH**

Département de génie mécanique

Thèse présentée en vue de l'obtention du diplôme de *Philosophiae Doctor*

Génie mécanique

Mai 2022

© Babak Beglarzadeh, 2022.

**POLYTECHNIQUE MONTRÉAL**

affiliée à l'Université de Montréal

Cette thèse intitulée :

**METROLOGY OF MACHINE TOOL COMPLIANCE UNDER QUASI-STATIC CONDITION**

présentée par **Babak BEGLARZADEH**

en vue de l'obtention du diplôme de *Philosophiae Doctor*

a été dûment acceptée par le jury d'examen constitué de :

**Aouni LAKIS**, président

**René MAYER**, membre et directeur de recherche

**Oguzhan TUYSUZ**, membre

**Mathieu RITOU**, membre externe

# DEDICATION

*To my family*

*for their sincere love*

# ACKNOWLEDGMENT

First and foremost, I am deeply grateful for the continuous support, insight, motivation, and patience of my excellent supervisor, Prof. René Mayer, without his invaluable guidance, assistance, encouragement, and dedicated involvement in every step throughout the process, this thesis would not have been completed.

I would also like to extend my deepest gratitude to Prof. Andreas Archenti from KTH Stockholm for extended discussions, friendly guidance, expert advice, encouragement, and all the support he gave me.

I gratefully acknowledge my thesis committee: Prof. Mathieu Ritou, Prof. Aouni Lakis, and Prof. Oguzhan Tuysuz for reading my thesis, giving me enlightening comments, and their acceptance to be on the jury.

I would like to thank Guy Gironne and Vincent Mayer, CNC technicians, for performing the experimental test and also for their support at Virtual Manufacturing Research Laboratory (LRFV) in Polytechnique Montréal.

Many thanks to my colleague and friends, especially Saed Sepahi, Huy Vu Ngoc, and Elie Bitar-Nehme for their encouragement and support.

I wish to thank NSERC Canadian Network for Research and Innovation in Machining Technology (CANRIMT) and AeroCREATE for funding this Ph.D. research.

Finally, my deep and sincere gratitude to Fatemeh and Artina for their continuous and unparalleled love, help, and support. I am forever indebted to my parents for giving me the opportunities and experiences that have made me who I am. They selflessly encouraged me to explore new directions in life and seek my own destiny. This journey would not have been possible if not for them, and I dedicate this milestone to them. I am also grateful to my sister Solmaz for always being there for me as a friend.

# RÉSUMÉ

Les industries comme l'aérospatiale, l'automobile, etc. exigent une productivité élevée et une grande précision des pièces usinées, ce qui requiert une rigidité élevée des machines-outils. En outre, pour maintenir la machine dans l'état de performance souhaité, il est crucial de surveiller et de compenser la précision des machines. Cette thèse présente de nouveaux modèles, artefacts et méthodologies pour surveiller la précision d'une machine-outil en analysant à la fois sa compliance articulaire et sa compliance volumétrique. La compliance volumétrique de la machine est étudiée en fonction de la position, de l'orientation et de la charge.

Le nouveau modèle de compliance des articulations est mis au point et est estimé indirectement à différents niveaux de charge volumétrique radiale et de données de déplacement obtenu au moyen du test de la barre à double bille chargée (LDBB). Une matrice jacobienne numérique du changement de la longueur de la LDBB en fonction des compliances articulaires et des forces appliquées est générée en utilisant le modèle cinématique et de compliance du mécanisme en série. Les simulations et l'étude de la matrice jacobienne numérique indiquent une dépendance entre les compliances des axes X et Y en raison de la nature de l'essai. Il est démontré que les compliances dominantes sont les compliances le long des articulations X et Y soit $C_{XXX}$ et $C_{YYY}$. Le modèle permet de séparer la contribution de certains groupes de compliance pour guider les réparations et prévoir la déviation dans diverses conditions telles que lors de l'usinage. Étant donné que des erreurs géométriques peuvent aussi influencer les résultats de la LDBB, on introduit le modèle élasto-géométrique qui utilise le principe de superposition pour séparer les effets de la compliance des articulations et des erreurs géométriques sur la position radiale de l'outil par rapport à la pièce. Les paramètres du modèle élasto-géométrique sont ajustés avec les lectures LDBB pour différents niveaux de force en identifiant parmi les erreurs celles qui changent avec la force (effet de compliance) de celles qui ne changent pas (effets géométriques). Il a été démontré qu'au niveaux de force inférieur et supérieur, les erreurs géométriques et de compliance dominent, respectivement. La compliance étant supposée constante dans le premier modèle élaboré, cela peut être la cause du changement apparent des paramètres d'erreur géométrique à différents niveaux de force. Par conséquent, le modèle de compliance a été enrichi par une fonction linéaire de la force appliquée pour traiter toutes les données de niveau de force ensemble, de sorte que la géométrie estimée reste la même à tous les niveaux de force.

Un nouvel appareil d'essai, le Ball-Roller Bearing Device (BRBD) est présenté. La rigidité volumétrique de la machine est examinée par ce dispositif. La force et l'engagement sont calculés à partir du courant du servomoteur et des lectures de l'encodeur disponible via la commande numérique

de la machine, respectivement, ce qui en réduit le coût et augmente la robustesse. On observe que la rigidité de la machine augmente avec le niveau de force.

En résumé, ces travaux contribuent au développement de modèle et de l'appareillage de mesure pour évaluer la précision d'une machine-outil du point de vue de la compliance. Le modèle et le dispositif développés peuvent quantifier la compliance de la machine et déterminer son origine dans la structure de la machine, information utile  pour l'auto-étalonnage et l'auto-caractérisation de la machine-outil.

# ABSTRACT

Industries such as aerospace, automotive, etc. require high productivity and high accuracy of the machined part, which demand high stiffness of the machine tool. Furthermore, to keep the machine in the desired performance condition, it is crucial to monitor and compensate for the machine's compliance. This research presents modeling, novel artefact, and methodology developed to monitor the accuracy of the machine tool by analyzing both machine axes and volumetric compliance under loaded conditions. The machine's volumetric compliance can be studied as a function of position, orientation, and load.

A joint compliance model is developed and indirectly estimated using different levels of volumetric radial load and displacement data obtained via the Loaded Double Ball Bar (LDBB) test. A numerical Jacobian of the change in the LDBB length as a function of the machine joint compliances and the applied forces is generated by using the kinematic and compliance model of the serial mechanism. Simulations and investigation of the numerical Jacobian matrix reveal confounding among the X- and Y-axis compliances due to the nature of the test. It is shown that dominant compliances were the on-axis compliances including $C_{\mathrm{XXX}}$ and $C_{\mathrm{YYY}}$. This model allows, to separate the contribution of compliance to guide repairs and predict deflection under various conditions such as when machining. As geometric errors are also present during the LDBB tests an elasto-geometric model is presented which uses the principle of superposition to separate the effects of joint compliance and geometric errors on the radial position of the tool relative to the workpiece. The elasto-geometric model's parameters are tuned with LDBB reading at different force levels by identifying among the errors which are changing with force (compliance effect) and the ones which do not (geometric effects). It was shown that at the lower and higher force level, geometric and compliance errors are dominant, respectively. In the initial model, the compliance is assumed to be constant which appeared to be causing apparent changes in the geometric error parameters at different force levels. Consequently, the compliance model was enriched as a linear function of the applied force to process all force level data at once so that the estimated geometry is kept the same at all force levels.

A novel test apparatus, Ball-Roller Bearing Device (BRBD) is introduced to study the machine's volumetric stiffness without added force device or sensor. The force and engagement are calculated from the servo motor current and the encoder readings obtained from the CNC, respectively. It is observed that the machine volumetric stiffness increases as the load is increasing.

# TABLE OF CONTENTS

DEDICATION ..... III

ACKNOWLEDGMENT ..... IV

RÉSUMÉ ..... V

ABSTRACT ..... VII

TABLE OF CONTENTS ..... VIII

LIST OF TABLES ..... XI

LIST OF FIGURES ..... XIII

LIST OF SYMBOLS AND ABBREVIATIONS ..... XIX

CHAPTER 1 INTRODUCTION ..... 1

CHAPTER 2 LITERATURE REVIEW ..... 3

CHAPTER 3 GENERAL ORGANIZATION OF THE WORK ..... 26

CHAPTER 4 ARTICLE 1 MODELLING AND INDIRECT MEASUREMENT OF MACHINE TOOL EQUIVALENT JOINT COMPLIANCES ..... 28

4.1. Abstract ..... 28

4.2. Introduction ..... 29

4.3. Compliance Estimation Model ..... 30

4.4. Numerical Jacobian ..... 37

4.5. Simulation ..... 39

4.6. Results and discussion ..... 46

4.7. Uncertainty ..... 54

4.8. Conclusion ..... 56

4.9. Acknowledgements ..... 57

4.10. Reference ..... 58

CHAPTER 5 ARTICLE 2 MATHEMATICAL SEPARATION OF ELASTO-GEOMETRIC ERROR PARAMETERS FROM LOADED CIRCULAR TESTS ON A MACHINE TOOL .....59

5.1. Abstract .....59

5.2. Introduction .....60

5.3.Machine geometric and volumetric model .....63

5.4. Compliance model .....67

5.5. Elasto-geometric model .....68

5.6. Simulation .....70

5.6.1. SIMULATION RESULTS AND DISCUSSION .....72

5.7. Experimental Results and discussion .....78

5.7.1. GLOBAL (OVERALL) COMPLIANCE AND GEOMETRIC PARAMETERS.....80

5.7.2. LOCAL COMPLIANCE AND GEOMETRIC PARAMETERS.....85

5.8. Conclusion .....93

5.9. Acknowledgments.....94

5.10. References.....94

CHAPTER 6 SENSORLESS LOADED TEST FOR MACHINE TOOL STIFFNESS CHARACTERIZATION .....97

6.1. Abstract .....97

6.2. Introduction.....97

6.3. Ball-Roller Bearing Device.....98

6.4. Volumetric stiffness model .....101

6.5. Machine feed drive torque model .....102

6.6. Experimental validation .....106

6.7. Conclusion .....116

6.8. References.....117

CHAPTER 7 GENERAL DISCUSSION ..... 118

CHAPTER 8 CONCLUSION AND RECOMMENDATION ..... 121

8.1. Conclusion and contributions of the work ..... 121

8.2. Recommendations for future works ..... 122

REFERENCES ..... 124

# LIST OF TABLES

Table 4.1.The simulated compliance matrices for the X- and Y-axis is a block diagonal matrix where only the orange and green colored cells are used. .....35

Table 4.2. Simulated compliance ( mm/N ) of the X and Y axes simultaneously with the simulated value of all compliance terms. .....42

Table 4.3. Estimated compliance matrices ( mm/N ) for the X and Y axes simultaneously in the presence of non-zero simulated values of all compliance terms.....42

Table 4.4. Associated patterns which generated by the unique compliance terms, (One unit of the radial scale represents 15.0 µm). .....44

Table 4.5. Estimated compliance matrices ( mm/N ) for the X and Y axes simultaneously with the presence of a value of six compliance terms. .....45

Table 4.6. Estimated global compliance value ( mm/N ) of X and Y axes using all pressure data at once. .....48

Table 4.7. Estimated local compliance values for a different set of pressures. .....53

Table 4.8. Associated mean and standard deviation for each estimated compliance parameter. .....55

Table 5.1. A detailed description of relevant compliance and geometric errors. .....73

Table 5.2. LDBB response patterns generated by each compliance term (one unit of the radial scale represents 15.0 µm).....74

Table 5.3. LDBB response patterns generated by each geometric parameter (one unit of the radial scale represents 15.0 µm).....75

Table 5.4. Simulated and estimated compliance values and geometric errors. .....77

Table 5.5. Estimated global compliance value ( mm/N ) of X- and Y-axis using all force data at once. .....81

Table 5.6. Estimated global geometry value (rad, mm, or mm/m) of X- and Y-axis using all pressure data at once. .....81

Table 5.7. Estimated local compliance values (mm/N, rad/N, or rad/N mm) for different sets of two force levels. .....90

Table 5.8. Estimated local geometric values (rad, mm, or mm/m) for different sets of two force levels. .....90

Table 5.9. The fitting values for global, variable global, and local compliance predicted readings with different force levels. .....93

Table 6.1. Table 6.2. Motor constant value for X and Y feed drive axis [7]. .....104

Table 6.3. Pitch, transmission ratio and efficiency values of machine axes feed drive [7]. .....104

Table 6.4. Estimated parameters value (v) for machine X and Y feed drive axis .....105

Table 6.5. Measured setup (ball and roller-bearing) deflection in a single X_axis test.....109

Table 6.6. Measured ball, roller-bearing, and machine stiffness in a single X_axis test.....111

# LIST OF FIGURES

Figure 2.1. Deformation of spindle head by applying force in tool center point [3]. .....3

Figure 2.2. Tool deflection measurement in three different sections [3]. .....4

Figure 2.3. Schematic of the magnetic loading instrument. (A) Structure of the device and (B) cross-section perspective [14]. .....5

Figure 2.4. Stacked up a total deviation of the machine on the joints by spring model [21]. .....6

Figure 2.5. Schematic of the ultra-precision machine tool [22]. .....7

Figure 2.6. Tets setup for analysis of static stiffness of the guideway's in the radial direction [23]. ..8

Figure 2.7. Exploded model of horizontal machine tool and its component [25]. .....9

Figure 2.8. Finite element diagram for spindle structure with 1000 N applied force [25]. .....9

Figure 2.9. A hybrid model including a detailed mesh of machine bed [26]. .....10

Figure 2.10. Correlation between leaf venation and stiffened machine tool structures [27]. .....11

Figure 2.11. 3D schematic for machine tool support stiffness [29]. .....12

Figure 2.12. Preload and support stiffness dependency [30]. .....12

Figure 2.13. Different support placements were used in the experimental test, (a) First placement, (b) Second placement, (c) Third placement, and (d) Forth placement [30]. .....13

Figure 2.14. Machine tool loading device in quasi-static status. (a) Loaded double ball bar [32, 33]. (b) Stiffness workspace system [34]. .....14

Figure 2.15. Measurement of machine tool cartesian translational stiffness including LDBB and LVDT [40]. .....15

Figure 2.16. ELS model for machining system capability [49]. .....17

Figure 2.17. Schematic diagram of an elastically linked system which is modeled for the machine tool [50]. .....17

Figure 2.18. Combination of Bottom-Up and Top-Down modeling [52]. .....18

Figure 2.19. Block diagram model for machine tool servo drive system including disturbance force [56]. .....19

Figure 2.20. Block diagram of machine tool drive mechanism [57]. .....20

Figure 4.1. a) Five-axis CNC machining center with loaded telescopic double ball-bar mounted between the table and spindle balls. Only axes X and Y are used for the tests. b) CAD model of the laboratory 5-axis CNC machining center including loaded telescopic double ball-bar device (the CAD model differs from the real machine and is only shown to illustrate the overall machine geometry) .....31

Figure 4.2. Conceptual diagram of the LDBB test setup and its circular trajectory in the XY machine tool plane. Note that tx and ty as shown are negative. .....35

Figure 4.3. Free body diagram of the LDBB and main machine model components. .....38

Figure 4.4. 2-D conceptual diagram of the machine with the location of the on-axis, lateral, and torsional compliances (the cross-compliance terms are not illustrated). .....39

Figure 4.5. Data flow for the simulation for machine tool compliance. .....40

Figure 4.6. Figure 4.7. Simulated and predicted reading obtained from Table 2 and Table 3 . (One unit of the radial scale represents 15.0 µm). .....43

Figure 4.8. Simulated and predicted readings were acquired using compliance as simulated in Table 2 and as estimated in Table 5. (One unit of the radial scale represents 15.0 µm). .....46

Figure 4.9.Experimental and Predicted global loaded telescopic double ball bar readings for X and Y-axis simultaneously with six different levels of applied force without geometric errors. ρ_exp and ρ_pred are the experimental and predicted readings of a loaded telescopic double ball bar. .....49

Figure 4.10.Predicted readings of the loaded double ball bar (radial deviation versus the angle of the ball bar with the X-axis during the circular test) from the estimated global compliance parameters (CXXX, CXYX, CYYY , CCXY, CCYY, and CCCY) at the highest force (706 N). .....50

Figure 4.11. Predicted readings of the loaded double ball bar (radial deviation versus the angle of the ball bar with the X-axis during the circular test) from the estimated global compliance parameters (CXYX, CCXY, CCYY, and CCCY) at the highest force (706 N). .....51

Figure 4.12. Experimental and predicted loaded telescopic double ball bar readings with six different force levels without geometric errors and predicted using locally estimated compliance values. ρ_exp and ρ_pred are the experimental and predicted readings of a loaded telescopic double ball bar. .....52

Figure 4.13. Estimated local compliances obtained using data from two consecutive force levels (a dashed horizontal line from 76 to 706 N represents the unique global compliance value for each compliance term). .....54

Figure 4.14. Experimental repeated LDBB readings for 328 and 454 N. .....55

Figure 4.15. Type A uncertainty of global compliance parameters (CXXX, CXYX, CYYY, CCXY, CCYY, and CCCY). .....56

Figure 5.1. Schematic of the nominal model for the LDBB test and its circular path through the XY plane along with the machine with the topology of wCAFYXZSt where S stands for the spindle axis. Only the X- and Y-axis, shown in blue, are active during the LDBB circular test. Compliance and geometric parameters are shown in magenta and green color, respectively. .....64

Figure 5.2. 3D rendering of the target 5-axis machine tool (wCAFYXZSt) with the LDBB mounted. .....70

Figure 5.3. Data flow for the simulation of the elasto-geometric Model. .....72

Figure 5.4. The LDBB's simulated as well as integrated compliance and geometric readings with a given value of CXXX and EXX1 for seven different force levels (36,112, 238, 364, 490, 616, and 742 N). .....76

Figure 5.5. Simulated and predicted LDBB readings for values listed in Table 5.4 for eight different force levels (0, 36,112, 238, 364, 490, 616, and 742 N). ρG sim, ρC sim, ρComb sim, ρG pred, ρC pred, and ρComb pred is the simulated geometric, compliance, combined and predicted geometric, compliance, and combined readings respectively. .....78

Figure 5.6. Loaded double ball bar test setup. The direction of the test is clockwise. The work ball is fixed, and the tool ball is moving. The test is conducted in the XY plane. .....80

Figure 5.7. Experimental and predicted global loaded double ball bar readings for X and Y-axis simultaneously with seven different levels of applied force. ρ_exp and ρ_pred are the experimental and predicted readings of a loaded double ball bar. .....82

Figure 5.8. Predicted global loaded double ball bar readings for the X and Y-axis simultaneously with seven different levels of applied force. (a) Predicted combined readings (ρ_pred). (b) Predicted compliance readings (ρ_comp_pred). (c) Predicted geometric readings (ρ_geo_pred). .....83

Figure 5.9. Predicted readings of the loaded double ball bar (radial deviation versus the angle of the ball bar with the X-axis during the circular test) from the estimated global compliance parameters at the highest force (742 N). (a) CXXX, CXYX, CYYY , CCXY, CCYY, and CCCY. (b) CXYX, CCXY, CCYY, and CCCY.....84

Figure 5.10. Predicted readings of the loaded double ball bar (radial deviation versus the angle of the ball bar with the X-axis during the circular test) from the estimated global constant geometric parameters at the highest force (742 N). (a) EXX1, EYX2, EXY2, EYY1, EC0YX, EXt0, and EYt0. (b) EYX2, EXY2, EC0YX, EXt0, and EYt0.....84

Figure 5.11. Experimental and predicted local loaded telescopic double ball bar readings for X and Y-axis simultaneously with seven different levels of applied force. ρ_exp and ρ_pred are the experimental and predicted readings of a loaded telescopic double ball bar. (a) Includes the 112 N force level results and the predicted traces are obtained using parameters estimated using the following two adjacent force levels ([36, 112], [112, 238], etc.). (b) Without 112 N force level and using the following two adjacent force levels ([36, 238], [238, 364], etc.).....86

Figure 5.12. Predicted local loaded telescopic double ball bar readings for the X and Y-axis simultaneously with seven different levels of applied force. (a) Predicted local combined readings (ρ_pred). (b) Predicted local compliance readings (ρ_comp_pred). (c) Predicted local geometric readings (ρ_geo_pred). .....88

Figure 5.13. Predicted readings of the loaded double ball bar (radial deviation versus the angle of the ball bar with the X-axis during the circular test) from the estimated local compliance parameters at the highest force (742 N). (a) CXXX, CXYX, CYYY , CCXY, CCYY, and CCCY. (b) CXYX, CCXY, CCYY, and CCCY.....89

Figure 5.14. Predicted readings of the loaded double ball bar (radial deviation versus the angle of the ball bar with the X-axis during the circular test) from the estimated local geometric parameters at the highest force (742 N). (a) EXX1, EYX2, EXY2, EYY1, EC0YX, EXt0, and EYt0. (b) EYX2, EXY2, EC0YX, EXt0, and EYt0. .....89

Figure 5.15. Estimated local compliances were acquired employing data from two adjacent force levels (dashed and dotted lines from 36 to 742 N depict the constant and variable global compliance value obtained by using all force results, respectively). .....91

Figure 5.16. Estimated local geometric parameters were acquired employing data from two continuous force levels (dashed and dotted lines from 36 to 742 N depict the constant and variable unique global geometric parameter value for each compliance term, respectively).....92

Figure 6.1. A schematic of BRBD and machine equivalent deflection. (a) Before commanding displacement. (b) After commanding displacement. (c) Free body diagram of BRBD. kTB, kWB, kRB, kB, and δEnc represent tool branch workpiece branch stiffness, roller bearing stiffness, ball stiffness, and encoder displacement, respectively. .....99

Figure 6.2. Photos of BRBD (left) mounted on a machine tool ready to test (right).....100

Figure 6.3. Huron KX8 five-axis vertical machine tool with BRBD mounted on it. .....100

Figure 6.4. Schematics of applied torques through the machine tool feed drive during the BRBD test. .....103

Figure 6.5. Estimated inertial, viscous, coulomb, and disturbance force for the maximum displacement of 200 µm. (a) X-axis. (b) Y-axis. .....105

Figure 6.6. Installed dynamometer table and BRBD device on the machine tool.....106

Figure 6.7. Comparison of dynamometer measured force (Dyn) and current-based force (Cur) for different commanded displacements with 1000 mm/min feed rate. .....107

Figure 6.8. Set up stiffness measurement with the dial indicator at X-direction and 1000 mm/min feed rate.....108

Figure 6.9. Dial indicator readings as a function of encoder commanded displacement. (a) Ball deflection. (b) Roller bearing deflection. (c) Machine deflection. .....110

Figure 6.10. Compensated volumetric stiffness (kVM) for various commanded displacements (40, 80, 120, 160 and 200 µm). .....112

Figure 6.11. Measuring the stiffness of the rig by adding certain weights (11.89, 24.97, 31.90, 56.85, 68.75, 79.77, 91.66, 104.74, and 111.68 N) and measuring the displacement by a dial indicator. .113

Figure 6.12. Stiffness validation setup with BRBD, rig, and dynamometer table. (a) setup without the rig. (b) setup with the rig.....114

Figure 6.13. Stiffness variation for different commanded displacements. (a) setup with the rig. (b) setup without the rig.....115

Figure 6.14. Machine volumetric compliance without a rig, with the rig, and predicted with rig for different commanded displacements. CVM, CVM_wr, and CVM_wr_pred represent machine volumetric compliance without a rig, with the rig, and predicted with the rig. ..... 116

# LIST OF SYMBOLS AND ABBREVIATIONS

| | |
|---|---|
| BRBD | Ball Roller Bearing Device |
| CAE | Computer-Aided Engineering |
| CMM | Coordinate Measuring Machine |
| CSV | Collinear Stiffness Value |
| DOE | Design Of Experiments |
| ELS | Elastically Linked System |
| FEM | Finite Element Method |
| FFT | Fast Fourier Transform |
| FRF | Frequency Response Function |
| FSF | Form Shaping Function |
| GUM | Guide To The Expression Of Uncertainty In Measurement |
| HMM | Hybrid Modeling Methods |
| HTM | Homogeneous Transformation Matrix |
| ISO | International Standard Organization |
| LDBB | Loaded Double Ball Bar |
| LVDT | Linear Variable Differential Transformers |
| NCCP | Non-Contact Capacitive Probes |
| RMSE | Root Mean Square Error |
| RSV | Rotational Stiffness Value |
| SMM | Single Module Methods |
| SSV | Screw Stiffness Value |
| SWS | Stiffness Workspace System |
| TSV | Translational Stiffness Value |
| VMSS | Virtual Machining System Simulator |
| WCS | Workpiece Coordinate System |

# CHAPTER 1 INTRODUCTION

Machine tool precision is a significant attribute. Identifying error sources, their physical cause, and their contribution to machine precision are key factors in the design of high precision machines. Machine tool accuracy is affected by factors such as static stiffness, dynamic stability, geometry, and thermal expansion.

Machine compliance causes inaccuracies when forces are present such as the weight of the workpiece, the cutting forces during machining, and the inertial forces during its rapid motion when machining. Stiffness is the ability to resist deflection. The machine design, construction, wear and tear, and various malfunctions may affect its stiffness. Machine stiffness is a major criterion of performance for high-speed machining. Monitoring compliance may also reveal mechanical degradation and failures. Machine maintenance is greatly facilitated if problems can be detected early on and diagnosed to avoid unexpected machine breakdown, or making bad parts.

## 1.1. Problem definition

There are methods regarding loading the machine with weights or using force pistons and displacement sensors. Nonetheless, these are intrusive methods incompatible with Industry 4.0 style machine monitoring which requires simplicity, automation, and robustness. To evaluate and quantify machine tool stiffness numerous sensors and devices have been proposed A machine tools static compliance and hysteresis measurement procedure is suggested in ISO 230-1:2012. It uses an internally generated force resulting from a commanded motion that is resisted by the load cell and the machine structure. The relevant deflection is the difference between the commanded motion and the apparatus motion measured by a displacement sensor. One drawback of this approach is that the machine is not in motion as it is during machining and the test is unidirectional for a single setup. Another limitation is that there is a very limited separation of the source of any observed compliance.

## 1.2. Objectives

The primary objective of this research project is to establish indirect approaches to estimate the compliance of machine tools under machining feed rate conditions. The secondary objectives are:

1. Indirectly estimate joint compliance model from an LDBB load.
2. Develop an elasto-geometric model to separate the geometric errors and compliance-related effects from an LDBB test.
3. Evaluate machine compliance under the loaded condition without added sensors or loading devices.

## 1.3. Hypotheses

In this thesis, the following hypothesis applies:

The tested machine tools follow rigid body kinematics but with compliances at the joints only.

.

# CHAPTER 2 LITERATURE REVIEW

This chapter presents a short review of machine tool stiffness/compliance research. Since the machine tools have different parts, the stiffness/compliance of those parts will be reviewed individually. However, in the case of volumetric stiffness/compliance, all those parts may contribute.

## 2.1. Tool stiffness

Tool deflection specifically in a milling process affects the finished part accuracy. A tool can deflect significantly due to cutting forces depending on its stiffness which is partly dependent on the ratio of its length to diameter so-called slenderness [1-4]. As shown in Figure 2.1 the tool center point (P7) deflects the most. Additionally, as shown in Figure 2.2, section C deflects more in comparison with the A and B sections. The main purpose of online monitoring of tool stiffness and tool deflection compensation is to adapt tool path and trajectory during the machining process.

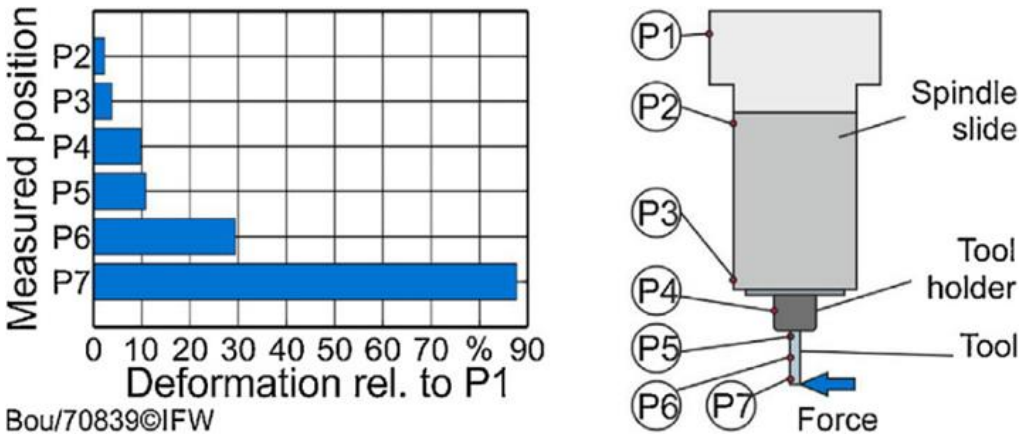


Figure 2.1. Deformation of spindle head by applying force in tool center point [3].

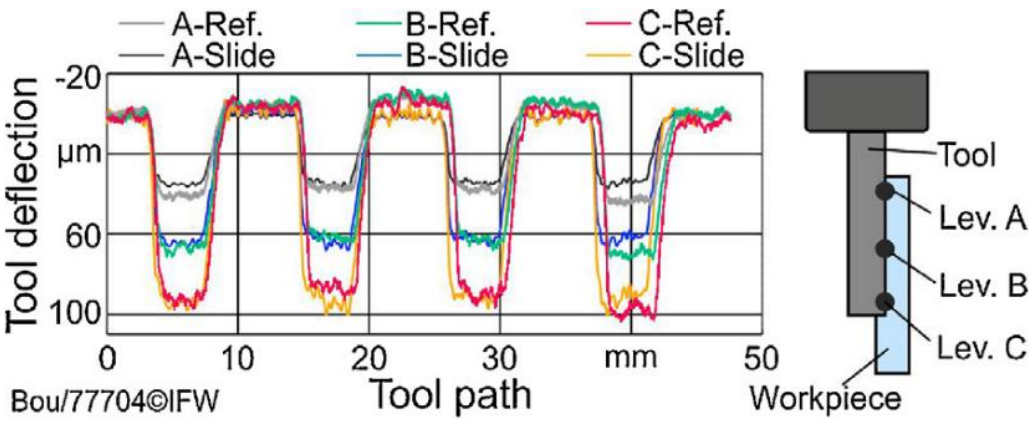


Figure 2.2. Tool deflection measurement in three different sections [3].

The cutting force causes a displacement of the tool tip via a stiffness chain which includes the tool, tool holder, spindle, and machine tool [5]. Depending on the tool stiffness it was observed that the tool contribution was between 30.5 and 55% of the total deflection. Cutting force and displacement are measured by the dynamometer and the inductive/eddy current sensor installed on the spindle, respectively.

Tooltip radial stiffness is associated with the kinematic chain displacement including the tool and workpiece branches [6]. To represent both kinematic chain displacements, an equivalent system is used. The value of the total stiffness is between 11.367 and 11.429 N/µm. From the experimental test, 79% of the total maximum error comes from static stiffness behavior of the turning center under load and 21 % comes from a quasi-static source such as thermal error, axis acceleration, etc.

Considering tool stiffness, most of the compliance errors come from both tool deflection and angular deformation of the collet [7]. Machine stiffness can be divided into several categories such as a tool, tool holder, and spindle stiffness. For instance, in a micro-milling experiment, the main compliance is related to the tool where it assigned 80-90 % of the total tool tip compliance to itself.

In the stiffness model at the tooltip, a point transformation matrix is used to transfer both force and displacement, and the multiplication of those matrices leads to the stiffness matrix at the tooltip [8, 9]. To analyze the machine's stiffness, all the parts stiffness such as axes, tool, and spindle should be considered. The Jacobian matrix can be used to transfer the displacement from the joint and cutter tool to the workpiece coordinate system (CSW).

Measuring the volumetric static stiffness of the machine tool requires the entire stiffness of the machine at the center of the tool. To quantify stiffness value, experimental tests are performed and the applied force to the tool center point and then resultant displacement are measured by the dynamometer and displacement sensors, respectively [10, 11].

## 2.2. Spindle stiffness

Non-contact measurement of the rotating spindle is conducted by using a magnetic loading device as shown in Figure 2.3 [12-17]. It attracts the dummy tool attached to the spindle and the spindle displacement is measured with eddy-current sensors at speeds up to 5000 $min^{-1}$. The frequency response function (FRF) can be estimated from the measured force and displacement of the spindle in the applied force direction. The first mode of natural frequency and damping of the spindle increase with the temperature of the spindle housing. Spindle stiffness also changes with speed.

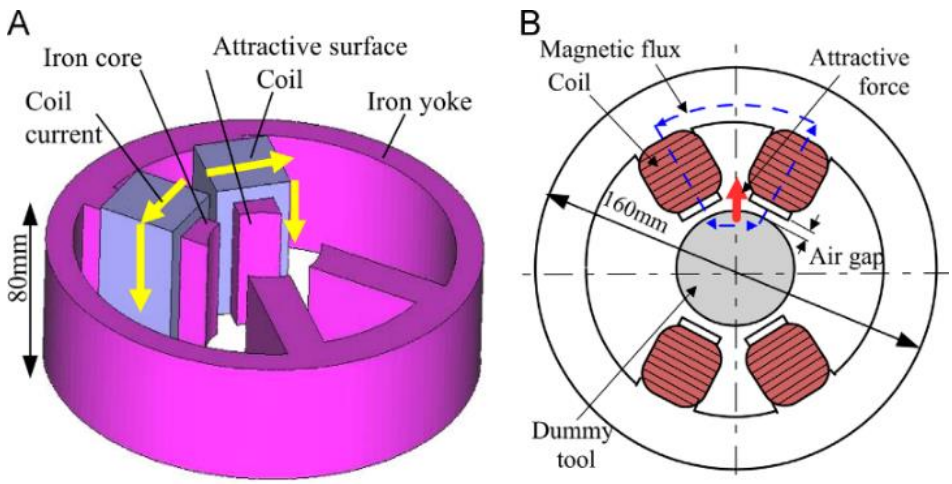


Figure 2.3. Schematic of the magnetic loading instrument. (A) Structure of the device and (B) cross-section perspective [14].

Machine tool stiffness can be monitored by using a cutting force and displacement sensor [18]. Up and down cutting tests in X- and Y- directions are used to produce a dynamic load measured by a dynamometer. To identify the spindle stiffness at various temperatures, a cutting test with different feed rates is used and it is shown that the generated temperature which increases by spindle rotation, has not much effect on the variation of spindle stiffness. The relationship between the displacement of the spindle and cutting force for various spindle speeds is linear. Furthermore, it is represented that the monitoring error comes from the spindle displacement because of the thermal effect and spindle stiffness modeling.

Tool holder-spindle stiffness is studied using different types of tool holder-spindle connections [19, 20]. Different methods including static test, FEM, and FRF are employed to estimate joint stiffness parameters. Mathematical modeling is used to evaluate the tool deflection at the cutting point where it could be minimized by increasing the tool, tool holder, and spindle shaft diameter and decreasing their length. Dynamic and static stiffness at tooltip which is modeled as a 2-DOF spring depends on spindle geometry, tool stiffness, bearings, housing, and all machine structure.

## 2.3. Joint stiffness

The top-down equivalent stiffness method is used to determine and calculate the contribution of joint stiffness to machine total deviation under loaded conditions [21]. The machine structure is modeled by several springs as shown in Figure 2.4. The maximum and the minimum deviation are observed between Pr1 - Pr2 and Pr6 points respectively. Hence, it is possible to measure the joint deflection based on the force-deviation model by using the acted force and torque.

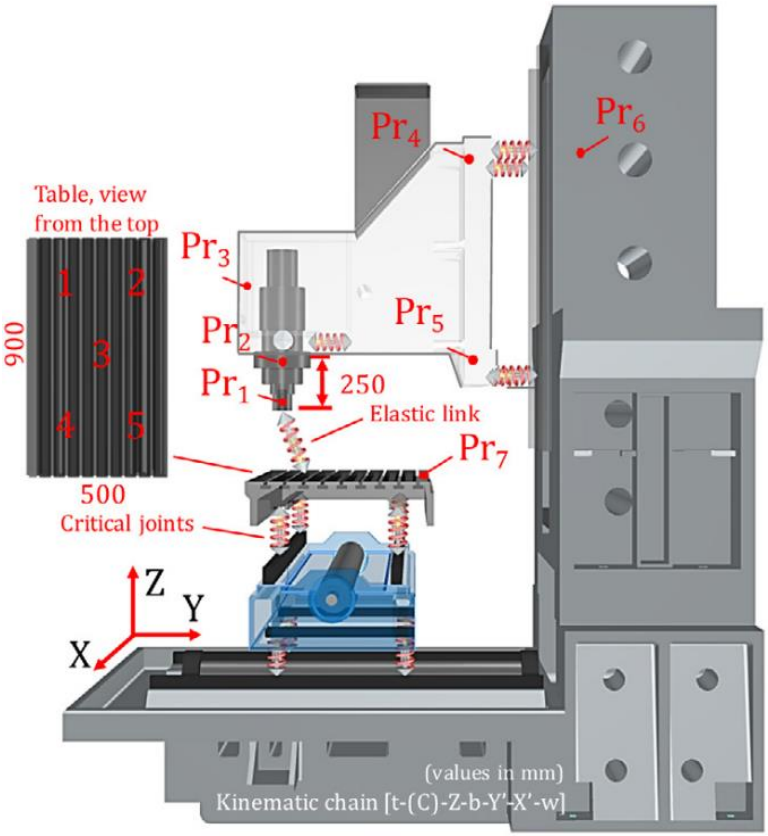


Figure 2.4. Stacked up a total deviation of the machine on the joints by spring model [21].

Hydrostatic guideways and bearings stiffness of ultra-precision machines can be obtained based on the virtual prototype machine [22]. Normal, lateral, and axial directions are used for the four load

applications and displacement points are used to estimate the normal, lateral, and axial compliance of the X, Y, and Z-axis feed systems. An optimization problem is used to minimize the error between measured and predicted compliances. It is found that the estimated normal and lateral stiffness of all three-linear axis and the C rotary axis were higher than the designed values due to machining error, assembling error, deformation of the machine structure, etc.  Figure 2.5 illustrates the schematic of an ultra-precision machine tool.

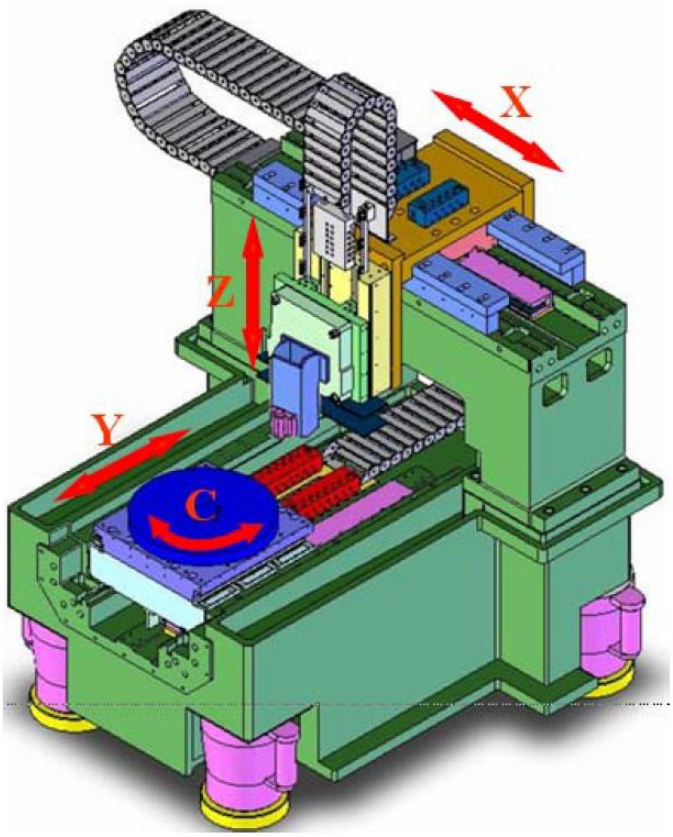


Figure 2.5. Schematic of the ultra-precision machine tool [22].

The analytical Hertzian theory is used to examine the static stiffness of the guideway's linear motion [23]. Normal, lateral, and angular directions are used for the static stiffness experiment. Figure 2.6 represents the experimental setup for the analysis of machine tool guideways in the radial direction. To measure the deviation in the movement a pneumatic cylinder and external mass on the carriages are used. The stiffness curves for the guides are nonlinear in all directions whereas this nonlinearity is more obvious when there is no preload. The static stiffness in the radial direction is larger than in the reverse radial and lateral direction. The highest angular deflections are at higher traveling speeds

and reversal backlash with high value can be viewed in the pitch and roll direction, specifically at higher speeds.

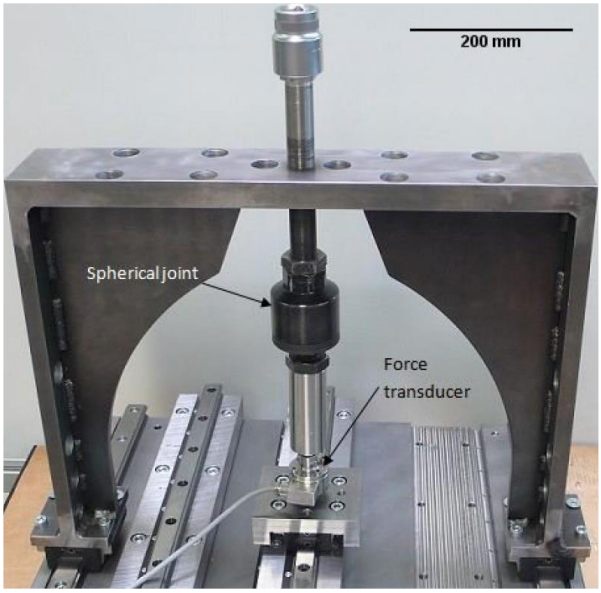


Figure 2.6. Tets setup for analysis of static stiffness of the guideway's in the radial direction [23].

## 2.4. Structural stiffness

Stiffness is the ability of a mechanical system to support external loads to resist extensive variation in machine geometry which is a key factor in the machine and system design [24]. The top-down design method can be used for machine stiffness that is built based on multi-body system theory to model the entire machine deflection [25]. To create a 3D model of the machine, the static equilibrium equations are applied and then the finite element method is used to validate the proposed method. Figure 2.7 represents the exploded model of a horizontal machine tool and stiffness coefficients. To evaluate machine displacement the force is applied to the machine structure. The machine structure is deflected due to the constant force which is applied to the machine spindle in the X-direction and the resultant deflection is measured by eddy current sensors.

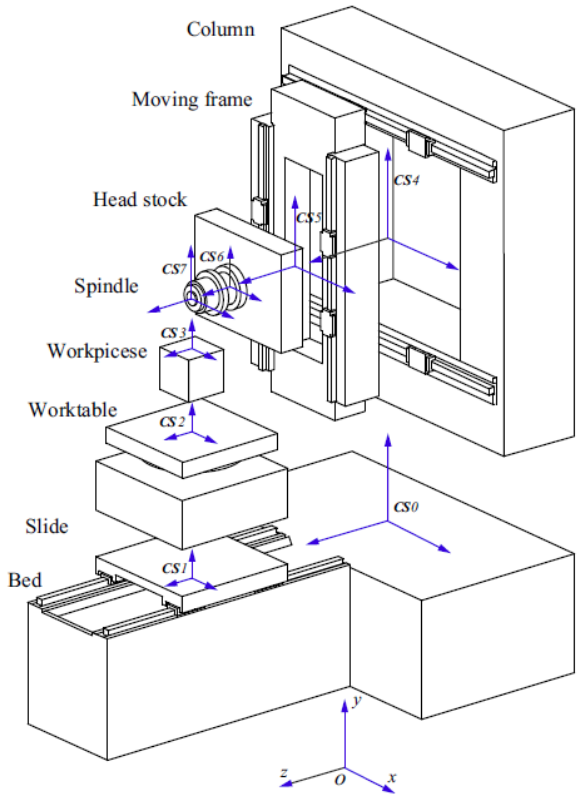


Figure 2.7. Exploded model of horizontal machine tool and its component [25].

To model the machine's total stiffness each part is considered separately and each part's stiffness is considered as a spring where it gives the resultant displacement in the force direction [25]. To validate the computational model, the finite element method is used. As shown in Figure 2.8 the spindle structure is deformed under 1000 N force in the Z direction.

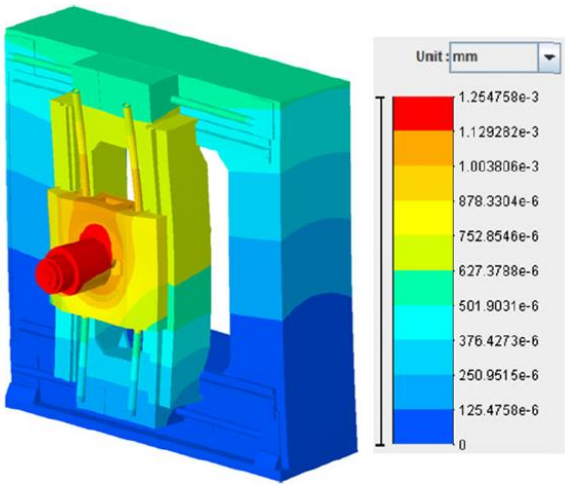


Figure 2.8. Finite element diagram for spindle structure with 1000 N applied force [25].

The Design of Experiments (DoE) method is applied to the machine stiffness evaluation which is connecting spindle structure stiffness relevant to the machine's entire stiffness [25].

CNC machine stiffness can be analyzed using the computer-aided engineering (CAE) technique such as finite element models [26]. In this technique, the model is divided into two single module methods (SMM) and hybrid modeling methods (HMM). Figure 2.9 shows a hybrid model including a detailed mesh of machine bed. In SMM, the auto-meshing method is used and the applied force to the tooltip and work-piece is considered as the equivalent force on each module. The other coupled parts which connect two components are considered as the constraints such as the column and bed. In HMM, creating a hybrid model is proposed for the machine which includes adjusting the boundary conditions and the application of load. To analyze the machine stiffness by SMM, some factors should be considered such as the right location of the module where the force will apply, defining the boundary condition properly, especially the bed, and obtaining the right local stiffness to illustrate each module stiffness. In analyzing the machine stiffness by HMM, the unit force, which is applied at the work-piece and the tooltip, can be transferred as an internal force to the machine structure. Subsequently, the mentioned force can be transferred to the nodes in the interfacial zone, which is between the two connected modules. the HMM is more accurate and efficient in comparison with SMM.

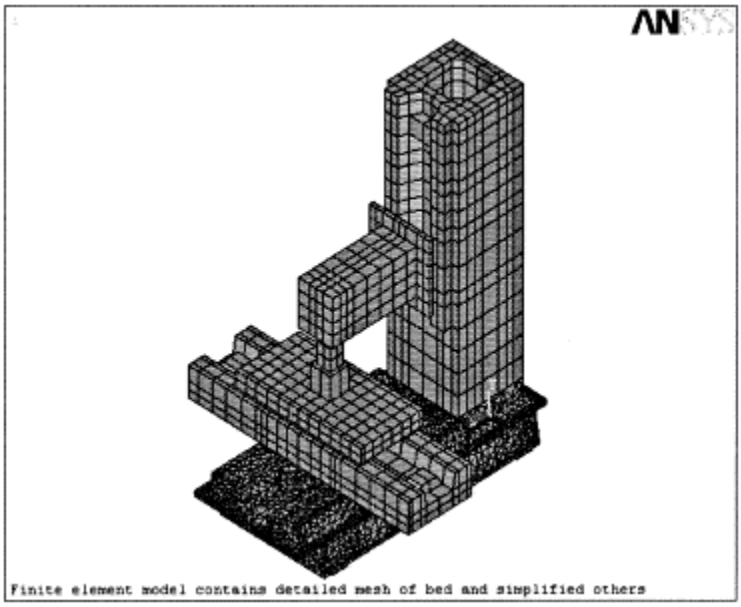


Figure 2.9. A hybrid model including a detailed mesh of machine bed [26].

Designing the stiffener layout inside large machine tools is proposed by the self-optimal growing rule by the ramifications of the plant [27]. The optimal load-bearing topology is created by using the leaf venation for a high stiffness machine tool. The approach can be used for re-designing the machine tool. One of the compliance effective tools is the leaf venation and the growth procedure is used for the complex structure in a machine tool. The growth-based method is the eco-efficient design tool for the generation of stiffener fundamentals in a machine tool.

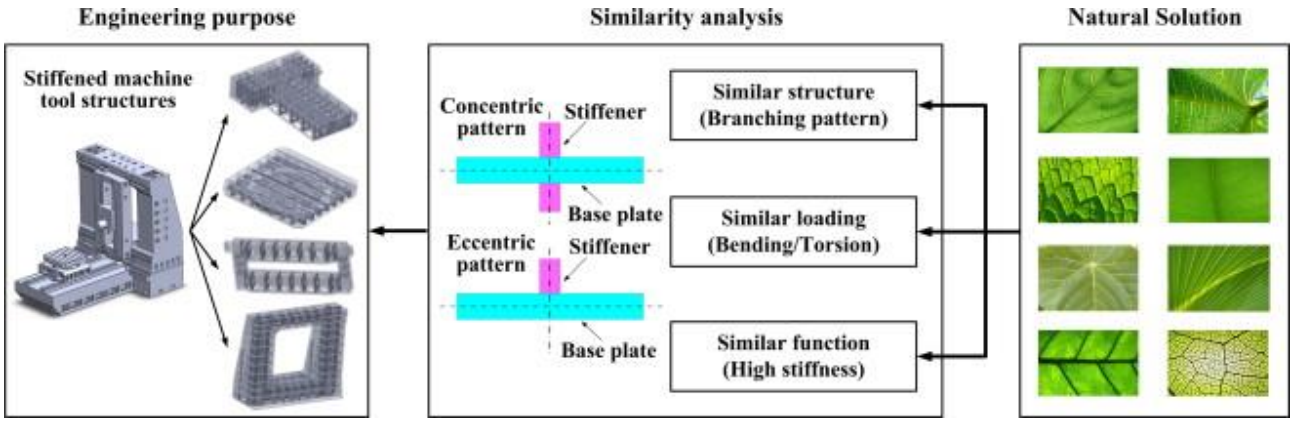


Figure 2.10. Correlation between leaf venation and stiffened machine tool structures [27].

The structure deforms owing to the loads produced by the machining process in different directions. Those loads can affect the tool displacement and machining inaccuracy [28]. Numerical modeling and simulation of different loads are used to analyze their impact on the stresses and deformation developed in the machine frame. The method is used to modify the machine frame components during the optimization of the designed part. Figure 2.10 illustrates the dependency between leaf venation and stiffened machine tool structures

## 2.5. Support stiffness

Machine tool support stiffness is investigated by using contact stiffness in a three-placement position including the front, rear, and center of the bed [29-31]. By using the contact stiffness model and applying proper location for the machine tool support, both grounds and drive disturbance vibration are decreased. Furthermore, the stiffness in an arbitrary direction is determined by the contact stiffness in the interfaces as well as the bulk stiffness of the supports and ground. In the proposed model the contact stiffness is obtained by multiplication of the unit stiffness contact with the real contact region. Figure 2.11 shows the 3D stiffness schematic for machine supports.

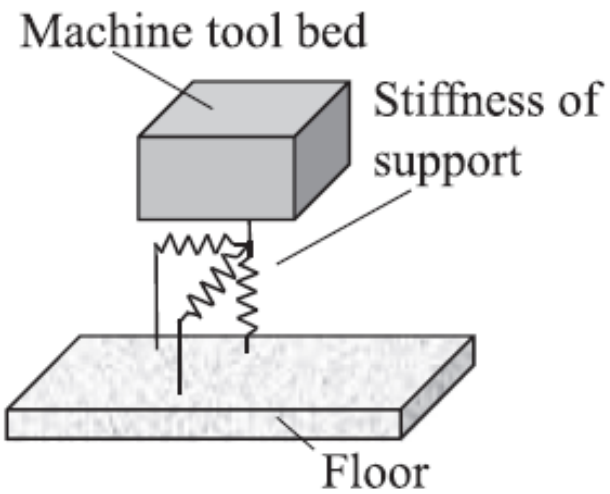


Figure 2.11. 3D schematic for machine tool support stiffness [29].

As shown in Figure 2.12 to investigate the machine tool support stiffness based on the contact stiffness, the relationship between the preloading and the stiffness of the support should be adjusted to stay in the critical region where the bulk stiffness is smaller than the contact stiffness. The increase of support stiffness strongly depends on the arrangement of the support placement. Figure 2.13 shows different support placements for the machine tool bed.

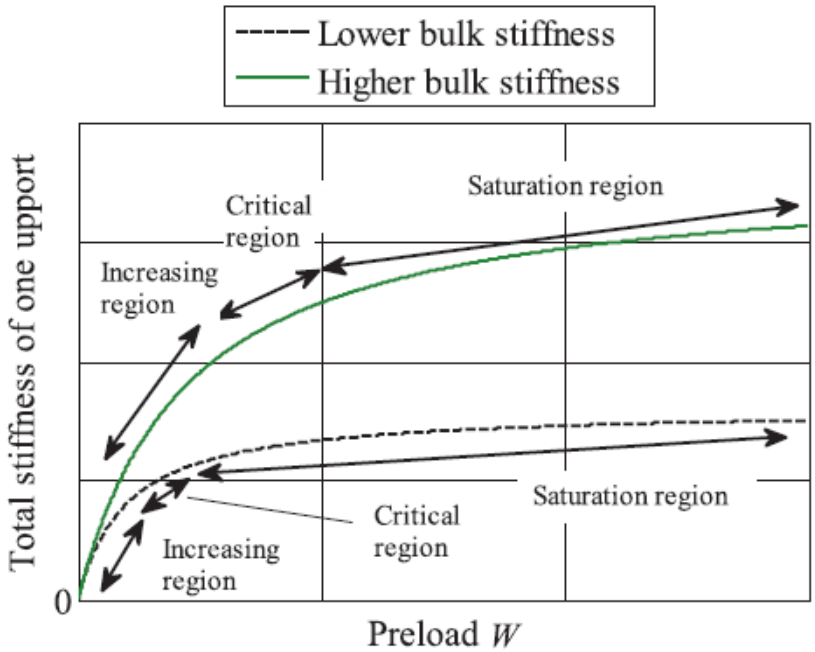


Figure 2.12. Preload and support stiffness dependency [30].

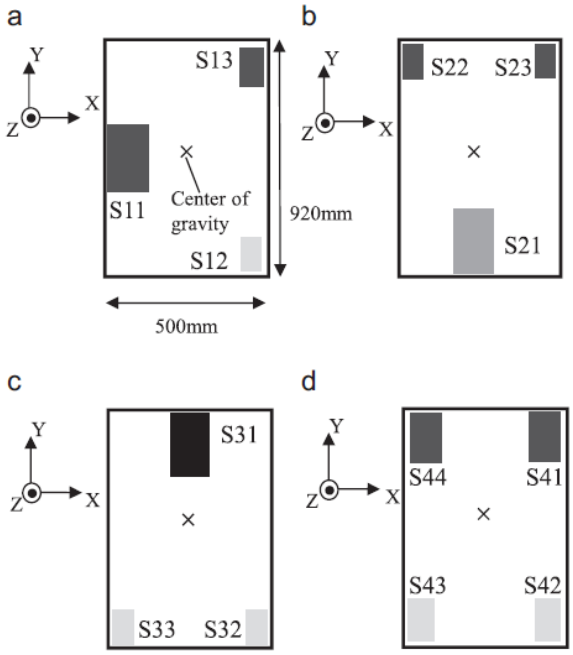


Figure 2.13. Different support placements were used in the experimental test, (a) First placement, (b) Second placement, (c) Third placement, and (d) Forth placement [30].

## 2.6.Volumetric stiffness

The volumetric stiffness is analyzed using loading devices such as the Loaded Double Ball Bar (LDBB) [32, 33] and the Stiffness Workspace System (SWS) [34]. The LDBB apparatus uses a pneumatic cylinder and a displacement sensor. It is an extension of the double ball bar (DBB) apparatus adopted, according to international standards, as a circular test instrument [35, 36]. The LDBB applies a force to the machine tool structure [37]. In both LDBB and SWS, the load is applied between the tool holder and work table of the machine, and this relative displacement is measured. Consequently, the volumetric quasi-static stiffness can be calculated in the machine's working volume.

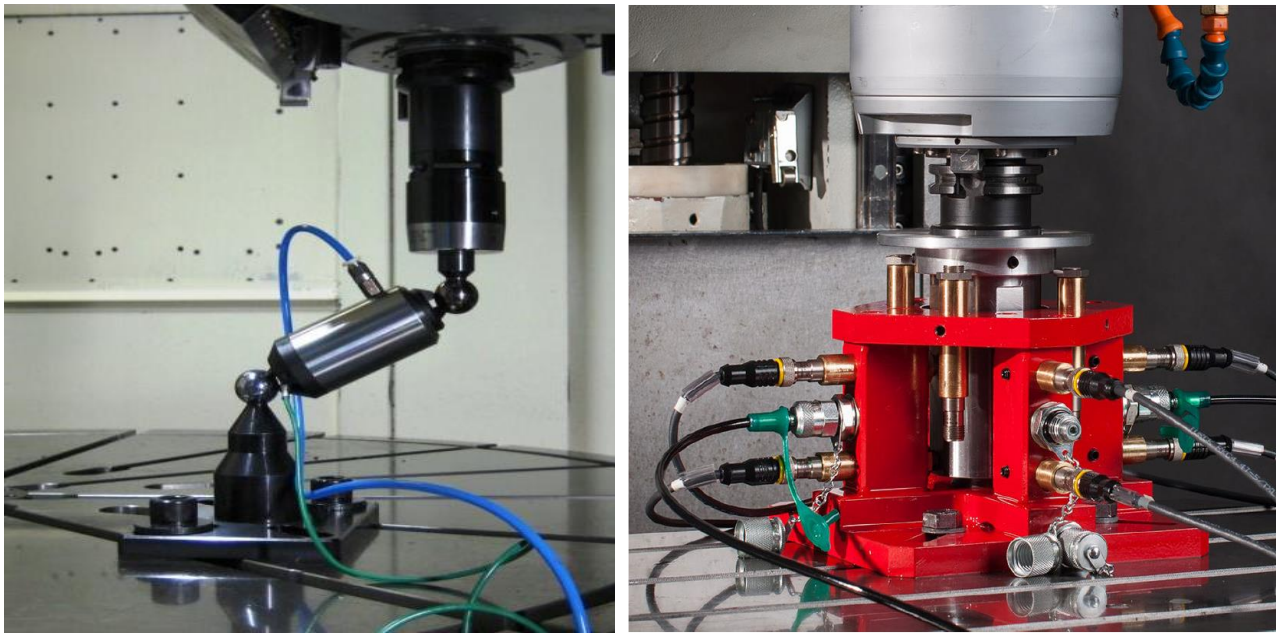

(a) (b)

Figure 2.14. Machine tool loading device in quasi-static status. (a) Loaded double ball bar [32, 33]. (b) Stiffness workspace system [34].

It is found that the volumetric stiffness depends on both the direction of applied force and its position in the workspace. Figure 2.14 shows the LDBB and SWS installed on the machine tool to measure the stiffness.

Direction dependency of both tool and workpiece compliance was defined as a frequency response function of the displacement between the tool, workpiece, and the cutting force [38, 39]. The frequency response function of the acceleration to the excitation force was acquired through an FFT analyzer and by integrating it, compliance was obtained. The compliance in both the X and Y direction was larger than in the Z-direction because the tool response and axial stiffness of the Z-axis were larger than the radial stiffness. The compliance maximum value in the X direction was almost twice as large as those in the Y and Z directions. The C rotary axis effect on the tool and workpiece compliance was considered by the compliance map. The bending direction and clamping condition of the C axis were important due to the influence on the direction dependency of compliance. It was shown that the clamping of the rotational axis increases the cutting vibration. The compliance map illustrated that the value of the compliance varied by up to 60 % with the changes in the clamping condition and the rotation angle. The rotation angle would affect more the direction which had smaller stiffness.

Machine tool volumetric stiffness including translational and rotational stiffness was measured by load and displacement sensors [40-42]. Load and displacement were measured by using LDBB and Linear Variable Differential Transformers (LVDT), respectively. For measuring the machine volumetric displacement another type of sensor such as Non-Contact Capacitive Probes (NCCPs) also was used. In the measurement process, the machine spindle tracks the circular trajectory inscribed by the movement of the machine rotary axis. Figure 2.15 shows the experimental setup for measuring the machine tool cartesian translational stiffness using LDBB and LVDT.

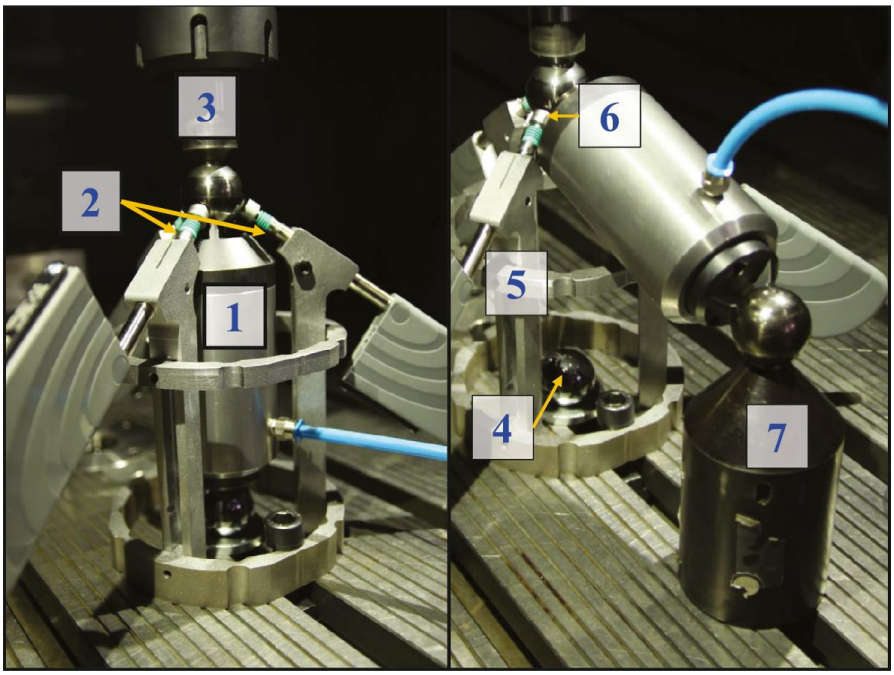


Figure 2.15. Measurement of machine tool cartesian translational stiffness including LDBB and LVDT [40].

## 2.7. Stiffness modeling

Modeling the static stiffness in the work space was used to evaluate the machine tool stiffness [43]. The machining space method was a suitable tool for designing the machine tool structure. This method was a connector between the spatial stiffness and the prediction of the resulting error in the machine tool. The load and deformation of each element are modeled with a stiffness matrix. The combination of the stiffness model for the whole machine was developed by synthesizing the deformation with the load transfer matrix. The six-directional static stiffness was developed within the parametric model to evaluate and design the machine tool stiffness.

Collinear stiffness value (CSV) was defined with a known configuration in a working space [44-48]. CSV includes translational stiffness value (TSV), rotational stiffness value (RSV) and screw stiffness value (SSV). CSV had a non-negative and positive value in singular and regular configuration respectively. The minimal CSV was applied in the regular configuration to estimate the local stiffness for the specified configuration in the working space. Form Shaping Function (FSF) was an important tool for machine design optimization. To make a connection between the applied force and the resultant displacement, the $6 \times 6$ stiffness matrix was defined as a ratio of a wrench to displacement. It is important to consider stiffness value in a design stage and limit the collinear stiffness value in a definite regular configuration. For machine stiffness evaluation, the minimal collinear stiffness value and its partial component including a translational stiffness value (TSV), rotational stiffness value (RSV), and screw stiffness value was used. In the machine working volume, the specified limits should be smaller than the both minimum translational and screw stiffness values. The collinear stiffness value is a potent tool for the evaluation of machine stiffness based on the configuration and structure of the machine to analyze different types of machine tool kinematics. Form shaping function (FSF) was used to evaluate machine tool kinematic, geometric, and compliance error and it gives important information about the machine layout and structure optimization which could be considered in the early design stage.

Machine tool accuracy was analyzed using the Elastically Linked System (ELS) model which connects the tool and workpiece position to the machined part geometrical error [49-53]. Figure 2.16 depicts a detailed explanation of the Elastically Linked System which depends on the machine tool structure, control system, and process.

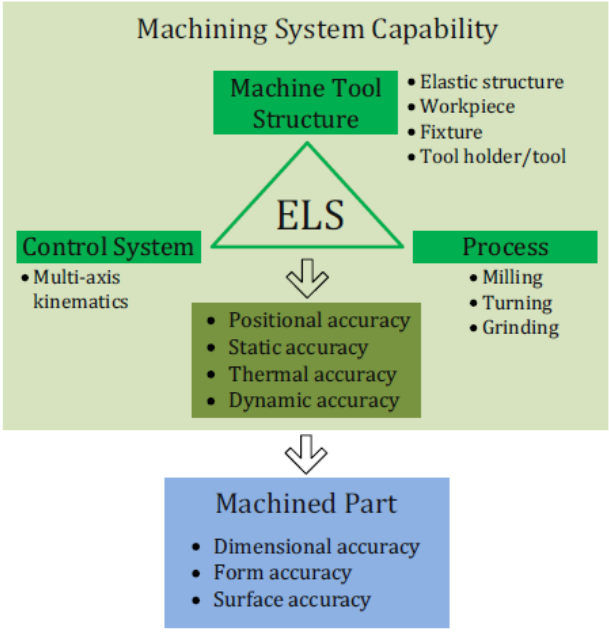


Figure 2.16. ELS model for machining system capability [49].

Additionally, machining system capability was connected to the accuracy of the machined part through the ELS model [53, 54]. Figure 2.17 represents the elastically linked system in which the LDBB instrument was considered as the connecting link between the tool and workpiece. The deviation of the system was calculated for the specified tool path. As shown in Figure 2.17, each element was considered as a spring and its displacement was counted for both the total deviation of the system and the maximum cutting force.

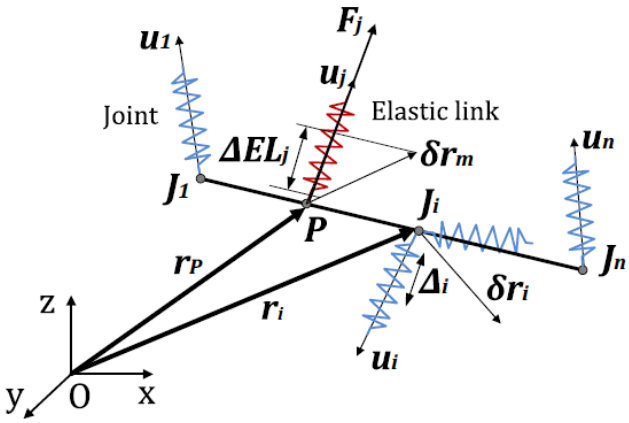


Figure 2.17. Schematic diagram of an elastically linked system which is modeled for the machine tool [50].

Bottom-Up and Top-Down methods were used for the analysis of machine tool errors in quasi-static status and loaded conditions [52]. These procedures were divided into two different direct and indirect measurements (laser interferometry and loaded double ball bar measurement). Both methods use the computational model to estimate machine geometric errors and static stiffness, and finally predict the errors under quasi-static and loaded conditions. Figure 2.18 depicts the detailed synthesis of the two-mentioned method.

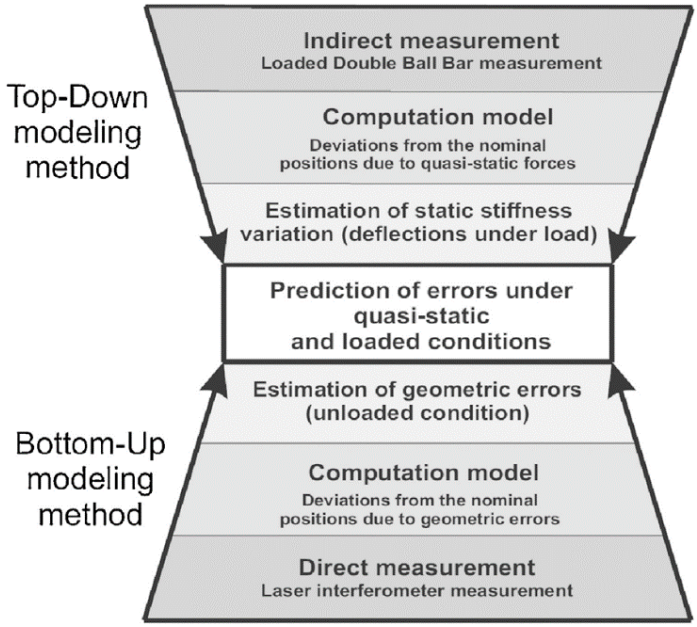


Figure 2.18. Combination of Bottom-Up and Top-Down modeling [52].

A top-down method was performed in different positions by using an LDBB to obtain optimum working space. It was claimed that stiffness is both direction and position-dependent. To characterize the stiffness in the machine coordinate system, the position and directional dependent stiffness were estimated by measuring the point stiffness in a spherical coordinate system. The point stiffness includes the stiffness both in the X and Y direction. If the loads were applied by the LDBB, it will be deviated from its nominal position, and to quantify the deviation, it is necessary to use the stiffness both in the X and Y direction. Virtual Machining System Simulator (VMSS) [55] was used to represent the quasi-static error and quantify it by simulating the interaction of the machine tool structure and cutting process based on the synthesis of the bottom-up and top-down model.

Static and dynamic stiffness of machine tools servo drive with disturbance force was modeled by a closed-loop control system [56]. Servo drive system stiffness was defined as the influence of disturbance forces on the position deviation. Figure 2.19 shows the model which is a closed-loop

control system including integrator gain (ki), input position ($X_i$), output position ($X_o$), damping quotient (b), sampling period (T), position loop gain ($K_v$), damping of the electrical parts (D), nominal angular frequency ($\omega$) of the electrical parts, total stiffness of the mechanical transmission elements ($K_{vk}$), coefficient of transformation of rotation in translation (kg), disturbance force (F), disturbance force gain ($K_f$), a gain of the mechanical transmission damping ($k_b$), Laplace operator (s), a mass of the mechanical parts (m), etc. Sensitivity to the load disturbance is the key parameter in the servo drive system which is the stiffness of the system. Increasing the damping of the electrical parts, sampling period and mass of the mechanical transmission elements will decrease the dynamic stiffness. On the contrary, the high value for the damping gradient of the mechanical transmission parts, the nominal angular frequency of the electrical element, position gain, and the total stiffness of the mechanical transmission elements will enhance the dynamic stiffness.

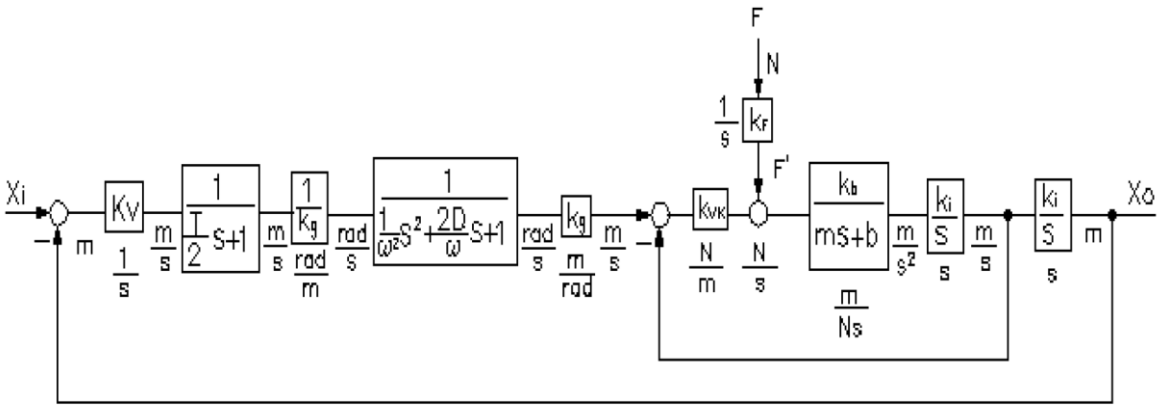


Figure 2.19. Block diagram model for machine tool servo drive system including disturbance force [56].

Machine tool feed drive system stiffness was modeled by a block diagram [57]. In the block diagram, the mechanical transmission elements were considered which include axis servo motors and a power train.

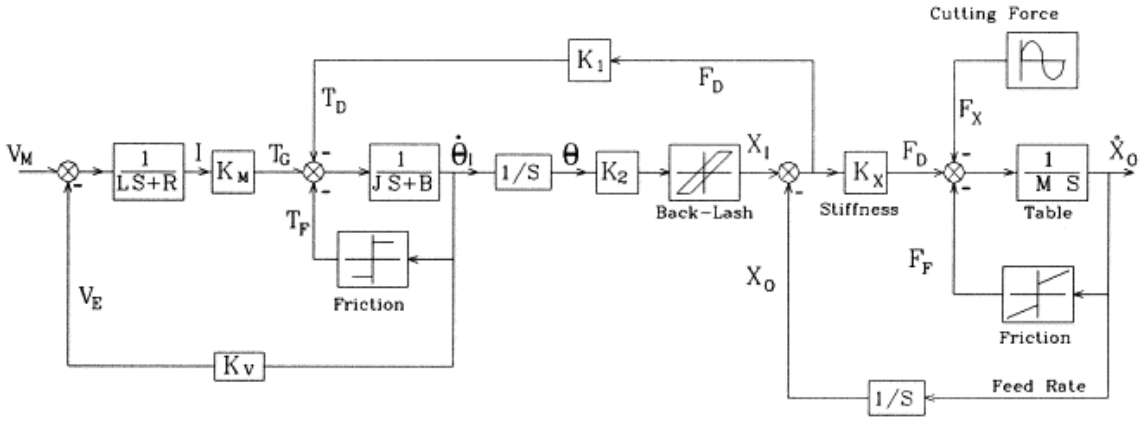


Figure 2.20. Block diagram of machine tool drive mechanism [57].

Figure 2.20 shows the relationship between the input voltage and cutting force of the machine axis feed drive system. To model Coulomb and viscous friction coefficients in the machine drive, the preloads elements were used. The total backlash in the machine drive system was shown by the hysteresis elements and it also affects the transverse movement of the table in a certain direction. The effect of stiffness, friction, backlash, and table mass can be monitored to optimize the drive condition. The application of such a model can be a design-validation tool that can demonstrate the effect of parameter variation on the performance of drive and machine tool settings.

The stiffness of the machine feed drive was examined using the feedforward procedure which is represented the effect of the stiffness on the machine performance. The axial stiffness of the machine feed drive was modeled as a spring-mass system for one and two ends thrust systems [58].

Machine volumetric stiffness measurement was performed by applying a known load to the machine table during the positioning of the working axis and measuring the displacement with the laser interferometer [59, 60]. The modified stiffness measurement which took place instantly after the beginning of the programmed position was more reasonable than the conventional measurement which was affected by the nonlinear behavior of the machine table during the loading process. Static stiffness after sliding was also introduced to better understand the differences between static stiffness and stiffness in motion. This method allows for a better assessment of machine working conditions and identifying faults such as assembly errors. A load speed increases the stiffness value [61]. The effect of hysteresis measurement as a function of the load on the machine stiffness was also studied [62]. It was shown that the hysteresis changes due to the dissipative force which occurs during the loading of the machine structures. This measurement method gives better insight into machine diagnostic and machinery development.

In summary, the aforementioned methods and models are mainly focused on machine tool components stiffness, separately. Furthermore, those methods are applicable in the analysis of machine volumetric compliance. Nonetheless, the new model is required to establish the relationship between joint and volumetric compliance under the loaded condition. None of the previously mentioned models and approaches are considered the effect of both machine compliance and geometry under the loaded status. Besides, the apparatus which are used for the analysis of the machine stiffness contains varieties of external sensors which is not of interest due to both sensor and setup errors. Consequently, novel models and measuring apparatus are needed to evaluate machine tool accuracy from the compliance point of view. Those needed models and apparatus will be introduced and presented in this thesis.

## 2.8. References


1. Denkena, B., K.M. Litwinski, and H. Boujnah, *Process Monitoring with a Force Sensitive Axis-slide for Machine Tools.* Procedia Technology, 2014. 15: p. 416-423.

2. Denkena, B., D. Dahlmann, and H. Boujnah, *Sensory Workpieces for Process Monitoring – An Approach.* Procedia Technology, 2016. 26: p. 129-135.

3. Denkena, B. and H. Boujnah, *Feeling machines for online detection and compensation of tool deflection in milling.* CIRP Annals, 2018. 67(1): p. 423-426.

4. Denkena, B., B. Bergmann, and M. Witt, *Feeling Machine for Process Monitoring of Components with Stock Allowance.* Machines, 2021. 9(3).

5. Salgado, M.A., et al., *Evaluation of the stiffness chain on the deflection of end-mills under cutting forces.* International Journal of Machine Tools & Manufacture, 2005. 45(6): p. 727-739.

6. Olvera, D., et al., *Analysis of the tool tip radial stiffness of turn-milling centers.* The International Journal of Advanced Manufacturing Technology, 2011. 60(9-12): p. 883-891.

7. Uriarte, L., et al., *Error budget, and stiffness chain assessment in a micromilling machine equipped with tools less than 0.3mm in diameter.* Precision Engineering, 2007. 31(1): p. 1-12.

8. Rong Yan, F.P., Bin Li, *A Method of General Stiffness Modeling for Multi-axis Machine Tool.* ICIRA, Part II, 2008. LNAI 5315: p. 1013-1021.

9. Yan Rong, P.F., Chen Wei, Yang Jianzhong, Linsen, *Closed-Loop Stiffness Modeling and Stiffness Performance Analysis for Multi-axis Process System.* ICIRA, Part II, 2010. LNAI 6425: p. 754-765.

10. Aachen, W.R. *Static and dynamic flexibility behaviour of machine tools*. 2018; Available from:https://www.wzl.rwthaachen.de/cms/www_content/en/9ca627d9a8ad2da3c1256fb2004537f7.htm.

11. Laboratory, R.s.A.T. *Measurement of Machine Tool Static Stiffness*. 2018; Available from: http://www.rcmt.cvut.cz/zkuslab/en/text/36.

12. Atsushi Matsubara, T.F., Iwao Yamaji, and Soichi Ibaraki *MEASUREMENT OF SPINDLE STIFFNESS FOR THE MONITORING SYSTEM OF CUTTING FORCES.* ASME, 2008: p. 4.

13. Taku YAMAZAKI, A.M., Tomaya FUJITA, Toshiyuki MURAKI, Kohei ASANO, Kazuyuki KAWASHIMA, *Measurement of Spindle Rigidity by using a magnet loader.* Journal of Advanced Mechanical Design, Systems, and Manufacturing, 2010. 4(5): p. 985-994.

14. Matsubara, A., T. Yamazaki, and S. Ikenaga, *Non-contact measurement of spindle stiffness by using magnetic loading device.* International Journal of Machine Tools and Manufacture, 2013. 71: p. 20-25.

15. Matsubara, A., et al., *Non-contact Measurement of Dynamic Stiffness of Rotating Spindle.* Procedia CIRP, 2014. 14: p. 484-487.

16. Yamazaki, T., A. Matsubara, and S. Ikenaga, *Measurement of Rigidity Change of Preload Switching Spindle.* International Journal of Automation Technology, 2012. 6(2): p. 175-179.

17. Sawamura, R., S. Ikenaga, and A. Matsubara, *Development of Dynamic Loading Device for Rotating Spindle of Machine Tools.* Key Engineering Materials, 2012. 523-524: p. 544-549.

18. Sarhan, A.A.D. and A. Matsubara, *Investigation about the characterization of machine tool spindle stiffness for intelligent CNC end milling.* Robotics and Computer-Integrated Manufacturing, 2015. 34: p. 133-139.

19. Agaplou, J.S., *A Methodology to Measure Joint Stiffness Parameters for Toolholder-Spindle Interfaces.* Journal of Manufacturing Systems, 2005. 24(1): p. 13-20.

20. Agapiou, J.S., *Estimating the Static Stiffness for a Spindle-Toolholder-Tooling System.* Machining Science and Technology, 2008. 12(1): p. 77-99.

21. Archenti, A. and M. Nicolescu, *A top-down equivalent stiffness approach for prediction of deviation sources in machine tool joints.* CIRP Annals, 2017. 66(1): p. 487-490.

22. W.J. Lee and S.l. Kim, *Joint Stiffness Identification of an Ultra-Precision Machine for Machining Large-Surface Micro-Features.* International Journal of Precision Engineering and Manufacturing, 2009. 10(5): p. 115-121.

23. Rahmani, M. and F. Bleicher, *Experimental and Analytical Investigations on Normal and Angular Stiffness of Linear Guides in Manufacturing Systems.* Procedia CIRP, 2016. 41: p. 795-800.

24. Rivin, E.I., *Handbook on Stiffness and Damping in Mechanical Design*. 2010, Three Park Avenue, New York, NY 10016, USA: ASME.

25. Shi, Y., et al., *A new top-down design method for the stiffness of precision machine tools.* The International Journal of Advanced Manufacturing Technology, 2015. 83(9-12): p. 1887-1904.

26. David Te-Yen Huang, J.-J.L., *On obtaining machine tool stiffness by CAE techniques.* International Journal of Machine Tools and Manufacture, 2001. 41: p. 1149-1163.

27. Li, B., J. Hong, and Z. Liu, *Stiffness design of machine tool structures by a biologically inspired topology optimization method.* International Journal of Machine Tools and Manufacture, 2014. 84: p. 33-44.

28. Vrtiel, Š., Š. Hajdu, and M. Behúlová, *Analysis of the machine frame stiffness using numerical simulation.* IOP Conference Series: Materials Science and Engineering, 2017. 266: p. 012015.

29. Kono, D., et al., *Stiffness model of machine tool supports using contact stiffness.* Precision Engineering, 2013. 37(3): p. 650-657.

30. Kono, D., et al., *A method for stiffness tuning of machine tool supports considering contact stiffness.* International Journal of Machine Tools and Manufacture, 2015. 90: p. 50-59.

31. Kono, D., et al. *Measurement of contact stiffness for stiffness estimation of machine tool supports*. in *Key Engineering Materials*. 2012. Trans Tech Publ.

32. Archenti, A., et al., *A new method for circular testing of machine tools under loaded condition.* Fifth Cirp Conference on High Performance Cutting 2012, 2012. 1: p. 575-580.

33. Archenti, A. and M. Nicolescu, *Accuracy analysis of machine tools using Elastically Linked Systems.* Cirp Annals-Manufacturing Technology, 2013. 62(1): p. 503-506.

34. Pawełko, P., et al., *A new measurement system to determine stiffness distribution in machine tool workspace.* Archives of Civil and Mechanical Engineering, 2021. 21(2).

35. Y. Kakino, Y.I., A. Shinohara, *Accuracy Inspection of NC Machine Tools by Double Ball Bar Method*. 1993, Japan: Hanser Pub Inc

36. *Renishaw Ball bar 20 software.* 2018.

37. Andreas Archenti, M.N., Guillame Casterman, Sven Hjelm, *A New Method for Circular Testing of Machine Tools Under Loaded Condition.* 5th CIRP Conference on High Performance Cutting 2012, 2012. 1: p. 575-580.

38. Kono, D. and A. Matsubara, *Investigation on Direction Dependency of Tool-Workpiece Compliance of Machine Tool.* Procedia CIRP, 2016. 46: p. 529-532.

39. Kono, D., Y. Moriya, and A. Matsubara, *Influence of rotary axis on tool-workpiece loop compliance for five-axis machine tools.* Precision Engineering, 2017. 49: p. 278-286.

40. Laspas, T., N. Theissen, and A. Archenti, *Novel methodology for the measurement and identification for quasi-static stiffness of five-axis machine tools.* Precision Engineering, 2020. 65: p. 164-170.

41. Theissen, N., et al., *Measurement for the identification of static and quasi-static rotational stiffness.* Precision Engineering, 2021. 72: p. 215-223.

42. Theissen, N.A., Gonzalez, M., Laspas, T., Archenti, A., *Measurement, and identification of dynamic translational stiffness matrix on machine tools under static preloads*, in *European Society for Precision Engineering and Nanotechnology*. 2021.

43. Gao, X., et al., *Stiffness modeling of machine tools based on machining space analysis.* The International Journal of Advanced Manufacturing Technology, 2016. 86(5-8): p. 2093-2106.

44. Portman, V., *Deterministic metrology of platform-type machine tools.* International Journal of Machine Tools and Manufacture, 2000. 40: p. 1423-1442.

45. Portman, V., *Stiffness Evaluation of Machines and Robots_ Minimum Collinear Stiffness Value Approach.* Proceedings of the 9th Biennial ASME Conference on Engineering Systems Design and Analysis, 2008: p. 1-8.

46. Shneor, Y. and V.T. Portman, *Stiffness of 5-axis machines with serial, parallel, and hybrid kinematics: Evaluation and comparison.* CIRP Annals, 2010. 59(1): p. 409-412.

47. Portman, V.T., et al., *Machine Stiffness Rating: Characterization and Evaluation in Design Stage.* Procedia CIRP, 2015. 36: p. 111-116.

48. Portman, V.T., et al., *Form-shaping function theory expansion: stiffness model of multi-axis machines.* The International Journal of Advanced Manufacturing Technology, 2014. 76(5-8): p. 1063-1078.

49. Archenti, A. and M. Nicolescu, *Accuracy analysis of machine tools using Elastically Linked Systems.* CIRP Annals, 2013. 62(1): p. 503-506.

50. Archenti, A., *Prediction of machined part accuracy from machining system capability.* CIRP Annals, 2014. 63(1): p. 505-508.

51. Archenti, A., *A Computational Framework for Control of Machining System Capability : From Formulation to Implementation*, in *Department of Production Engineering Machine and Process Technology*. 2011, KTH Royal Institute of Technology: Stockholm, Sweden.

52. Szipka, K., T. Laspas, and A. Archenti, *Measurement and analysis of machine tool errors under quasi-static and loaded conditions.* Precision Engineering, 2018. 51: p. 59-67.

53. Archenti, A. and T. Laspas, *Accuracy and Performance Analysis of Machine Tools*, in *Metrology*, W. Gao, Editor. 2019, Springer Singapore: Singapore. p. 215-244.

54. Szipka, K., T. Laspas, and A. Archenti, *Mechanistic Approach for the Evaluation of Machine Tools Quasi-Static Capability.* 2017: p. 229-243.

55. Nikolas Theissen, T.L., Károly Szipka, Andreas Archenti. *Virtual machining simulator: analysis of machine tool accuracy*. in *8th Swedish Production Symposium, SPS 2018*. 2018. Stockholm, Sweden: Procedia manufacturing.

56. Zoran PANDILOV, V.D., *STATIC AND DYNAMIC STIFFNESS OF CNC MACHINE TOOL SERVO DRIVES.* Journal of Machine Engineering, 2010. 10(4): p. 106-114.

57. M. Ebrahimi, R.W., *Analysis, modeling and simulation of stiffness in machine tool drives.* Computers & Industrial Engineering, 2000. 38.

58. Wang, B., J. Zuo, and M. Wang, *Analysis and Compensation of Stiffness in Cnc Machine Tool Feed System.* Journal of Advanced Manufacturing Systems, 2011. 10(01): p. 77-84.

59. Stejskal, T., et al., *Measurement of Static Stiffness after Motion on a Three-Axis CNC Milling Table.* Applied Sciences, 2017. 8(1): p. 15.

60. Stejskal, P.D.a.T., *Analytical, and Experimental Research of Machine Tool Accuracy*, in *Machine Tools*, Ľ.Š.a.J. Marek, Editor. 2020: IntechOpen.

61. Stejskal, T., et al., *Specific principles of work area stiffness measurement applied to a modern three-axis milling machine.* The International Journal of Advanced Manufacturing Technology, 2019. 102(5-8): p. 2541-2554.

62. Stejskal, T., et al., *Experimental assessment of the static stiffness of machine parts and structures by changing the magnitude of the hysteresis as a function of loading.* Open Engineering, 2019. 9(1): p. 655-659.

# CHAPTER 3 GENERAL ORGANIZATION OF THE WORK

The subject of the thesis was formed by Chapter 1 (introduction) and Chapter 2 (literature review). This Chapter presents the overall structure of the thesis including the article's overview. The subsequent three chapters (4, 5, and 6) include published/submitted papers which are the principal contribution of this Ph.D. research. The last two chapters of the thesis are a general discussion in Chapter 7 and a conclusion in Chapter 8.

The tests associated with Chapters 4 and 5 are conducted on the Hermle C50 machine in the center for Design and Management of Manufacturing Systems (DMMS) at KTH university. The tests in Chapter 6 are carried out on the Huron KX8 five-axis vertical machine in the Virtual Manufacturing Research Laboratory (Polytechnique Montréal) using a novel loading apparatus so-called a Ball roller bearing device (BRBD).

The article entitled “Modelling and indirect measurement of machine tool equivalent joint compliances”, which was published in November 2021in the CIRP Journal of Manufacturing Science and Technology, is in Chapter 4. The research work, presented therein, explores equivalent joint compliances that are estimated from LDBB readings using a kinematic and compliance model of the machine. The compliance parameters include the main, cross, and rotary compliances. There was confounding between the compliances of the X- and Y-axis. By using all force levels at once the global compliance is estimated whereas using only two force levels shows the variation of compliance with force. It is found that X-and Y-axis on-axis compliances $C_{XXX}$ and $C_{YYY}$ are the dominant compliances. As the force level increases, the dominant compliances also increase by approximately 5%. The values for $C_{XXX}$ and $C_{YYY}$ were 7.61E-05 and 6.05E-05 mm/N, respectively.

Chapter 5 is the article entitled “Mathematical separation of elasto-geometric error parameters from loaded circular tests on a machine tool”, which was submitted in February 2022 in the International Journal of Machine Tools and Manufacture. In this paper, an elasto-geometric model is introduced which uses the superposition principle to separate machine compliance and geometric errors. The model parameters are estimated by the reading of the LDBB device at different force levels. It is found that at a lower force, geometric errors are dominant while at the highest force level compliance errors dominate. By using adjacent force levels, the variation of both estimated compliance and geometry parameters with changes in force level is observed. As the force level increased, the majority of the compliance parameters also increased. The dependency of the compliance to the force

level is examined by a linear compliance model. The RMSE of the predicted reading for global constant and variable compliance were 0.0011 and 0.0009 mm, respectively. Both constant and linearly variable compliance models are represented with over 91% fit to the experimental data.

Chapter 6 presents the sensorless loaded test for machine tool stiffness characterization. The novel apparatus so-called Ball Roller Bearing Device (BRBD) is introduced to measure the machine tool volumetric stiffness. The volumetric compliance measurement procedure uses a circular test with commanded radial engagement between the ball and roller-bearing which causes a radial force to develop. The force and engagement are calculated from servo motor current and encoder reading. Setup compliance is measured with a dial indicator and the calculated machine tool compliance is compensated for it. The estimated force from servo motor current is validated by a dynamometer table. The calculated compliance is also validated using a known compliance value from a rig artefact added to the machine tool table.

# CHAPTER 4 ARTICLE 1 MODELLING AND INDIRECT MEASUREMENT OF MACHINE TOOL EQUIVALENT JOINT COMPLIANCES

B. Beglarzadeh [a], J.R.R. Mayer [a], A. Archenti [b]

[a] Department of Mechanical Engineering, Polytechnique Montreal, Montreal, QC, H3T 1J4, Canada

[b] Department of Production Engineering, KTH Royal Institute of Technology, Brinellvägen 68, Stockholm SE-10044, Sweden

* Published on 29 October 2021 in the CIRP Journal of Manufacturing Science and Technology

## 4.1. Abstract

Machine tools require high geometric accuracy and stiffness. Both of these characteristics affect the radius of a radially loaded circular test. By using various loads, the machine's volumetric compliance can be studied as a function of position, orientation, and load. Further processing of the data using a kinematic and compliance model of the machine allows the equivalent joint compliances to be estimated. This model also allows to produce the characteristic patterns of loaded telescopic double ball bar readings associated with each compliance term. The compliance model contains numerous superfluous and confounded terms that are pruned from the model. The analytical model is then used to produce a numerical identification Jacobian that is further applied to estimate the compliances from test data gathered at various force levels. By using all force data at once global compliance values are estimated whereas using only adjacent force level data allows observing the change in compliance with force. The new nomenclature is introduced where each compliance term has three subscripts. The first subscript is the direction of the displacement, the second subscript is the applied force direction, and the third subscript is the relevant joint or axis. The dominant compliances are the X-axis and on-axis compliance $C_{\mathrm{XXX}}$ (confounded with the lateral compliance of the Y-axis $C_{\mathrm{XXY}}$) and $C_{\mathrm{YYY}}$ (confounded with $C_{\mathrm{YYX}}$). It is observed that as the load increases from 76 to 706 N (by increments of 126 N), the dominant compliances increase by around 5%. Type A uncertainties of the calculated compliances are estimated from repeated measurements and are found to be relatively small. Some non-dominant compliances, such as the torsional compliance of the Y-axis $C_{\mathrm{CCY}}$ account for deflection of less than 0.5 % of that for the main compliances and has a negative value which is mechanically unexpected. It is explained in detail in the results and discussion section.

**Keywords:** Joint compliance, machine tool, measurements, numerical simulation

## 4.2. Introduction

High accuracy of machined parts and high productivity depends on machine tools having high accuracy and stiffness. An elastically linked system (ELS) was introduced [1] in the form of a loaded double ball bar (LDBB) that can apply a radial load between a ball at the tool attachment and another on the workpiece table and simultaneously measure the radial volumetric displacement during a circular test. The ELS concept was used [2] to study the relationship between machining system capability represented by geometric /kinematic errors and static deflection due to compliance and the machined part accuracy. The approach is based on the circular loaded measurement and the computational model in accordance with ELS multi-body simulation. The finite element model is used to consider the tool and workpiece contribution to the total deviation. The equivalent stiffness approach proposed in [3] models the machine compliance by seven sets of judiciously located three-axis linear springs within the machine structure and which stiffnesses are then quantified by the ELS technique.

Tool deflection was monitored by a “Feeling” approach in [4]. This technique allows online measurements of process force and tool stiffness in spite of disturbance in a working area. Metallic resistive strain gauges are incorporated in selected machine tool parts such as the spindle slides and spindle head to measure the process force. A calibration matrix is used to convert the strain gauge signals to force signals. The calibration matrix determined by linear regression uses components strain signal and reference external force signal. The discrepancy between the actual and nominal tool path caused by tool deflection is determined by stiffness measurement through the machine-integrated cycle which is based on controlled contact between the tool and workpiece whereby, while the spindle is locked, the tool moves towards the workpiece until a contact force is detected. From that position, the tool moves further by nominal pre-set distances. Since the tool is more compliant than the workpiece with reference to the conducted experiments, most of the pre-set distance becomes tool deflection. The tool is modeled as a cantilever beam and its stiffness is computed based on the pre-set distances and the variation in measured force.

Dynamic radial stiffness of a rotating spindle [5, 6] is measured by using a new magnetic loading device that attracts a dummy tool connected to the spindle. The spindle shaft and tool displacement are measured using Eddy current sensors and the applied load is measured using a dynamometer.

They found that the speed had less impact on the hardening (stiffness increase) than the spindle temperature.

The static stiffness of a machine tool's single linear motion guide was measured in all five constrained degrees of freedom in [7]. Some results were compared with a Hertzian contact theory model which was found to overestimate the stiffness. A maximum force of 10 kN was applied to measure stiffness in the compressed and tensile directions. Both the direction and sense of the force affected the stiffness. Non-linear behavior is also observed, especially at lower loads, with a tendency to stiffen with increasing load.

The impact of contact stiffness of the joint interface on the structural dynamics of the machine tool was examined in [8]. A theoretical model based on the fractal theory was used to compute the contact stiffness. The experimental test setup was designed to validate the simulated contact stiffness. The experimental test consisted of two models including fractal contact and a dynamic model. According to these two models, the impact of the interfacial contact stiffness on the structural dynamics of the machine tool was examined. It was indicated that by decreasing the preloads at two joints by 15%, the maximum displacement was increased by 1.74% and 2.90%, correspondingly. In this regard, it was shown that the sensitivity of joint interface among the column and lathe bed was higher.

Uncertainty of the measurement results is defined in GUM [9]. Type A uncertainty is the standard deviation of the repeated measurements.

Aforementioned models mainly focused on volumetric compliance. This paper explores the indirect estimation of joint compliance using a novel analytical model from the volumetric radial load and displacement data obtained via a circular loaded test. The physical mechanism causing compliance is not considered nor is the arrangement of guides constituting a particular joint. Joint compliance refers to a punctual location where the compliance is assumed to be acting. The model establishes the relationship between the joint and volumetric compliance and the joint compliance is estimated on the basis of a loaded circular test. This indirect method allows, given sufficiently rich tests to be determined, to separate the contribution compliance to guide repairs. The same model can then also be used to predict deflection under different conditions such as when machining.

## 4.3. Compliance Estimation Model

The loaded telescopic double ball-bar (LDBB) is shown, conceptually, mounted on a five-axis machine tool with a wCAFYXZt topology in Figure 4.1. The loaded telescopic double ball-bar applies a partial wrench, in the form of equal and opposite radial forces at the tool ball (attached to the spindle

unit via HSK100 interface) and the workpiece ball, and measures part of the resulting twist, in the form of the change in distance between the two balls, which is along the loaded telescopic double ball-bar axis.

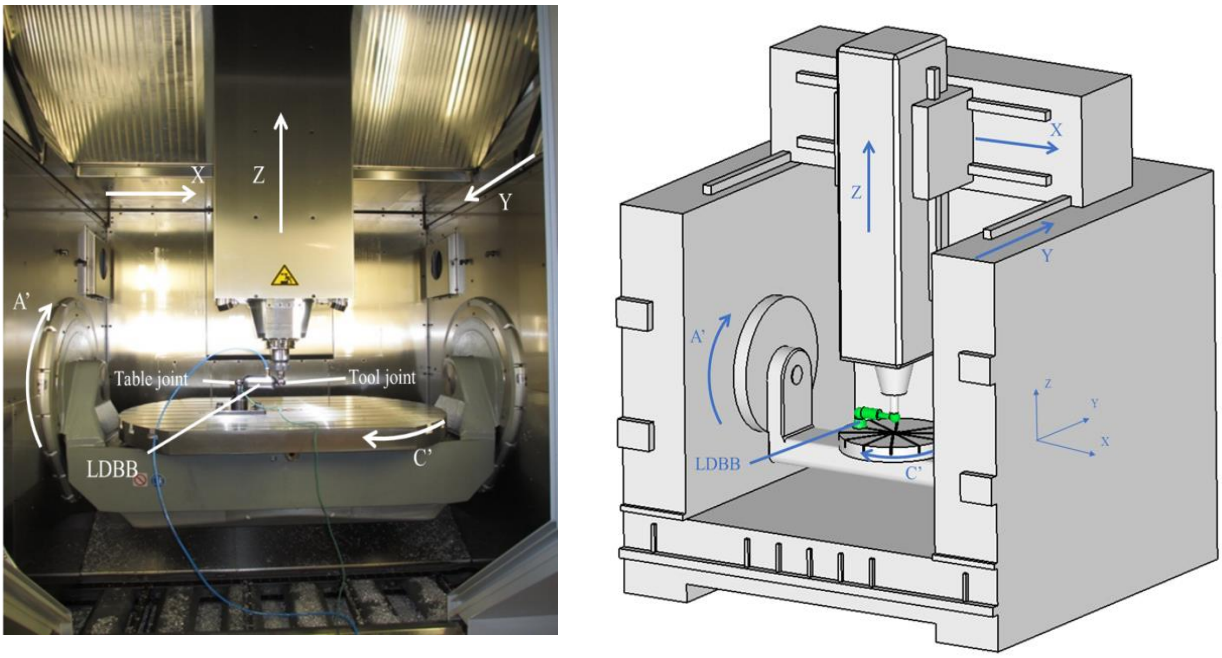


(a) (b)

Figure 4.1. a) Five-axis CNC machining center with loaded telescopic double ball-bar mounted between the table and spindle balls. Only axes X and Y are used for the tests. b) CAD model of the laboratory 5-axis CNC machining center including loaded telescopic double ball-bar device (the CAD model differs from the real machine and is only shown to illustrate the overall machine geometry)

These quantities are volumetric as they occur within the machine work envelope. The volumetric stiffness equation at the tool, t, is defined as [10]:

$$W_{\mathrm{t}} = K_{\mathrm{t}}.\Delta D_{\mathrm{t}} \tag{4.1}$$

where $W_{\mathrm{t}}$, $K_{\mathrm{t}}$ and $\Delta D_{\mathrm{t}}$ are the wrench, stiffness matrix, and displacement twists, respectively.

The general tool wrench, $W_{\mathrm{t}}$, has six components, three forces, and three torques along and around Cartesian axes:

$$W_{\mathrm{t}} = (F_{\mathrm{X}}, F_{\mathrm{Y}}, F_{\mathrm{Z}}, M_{\mathrm{X}}, M_{\mathrm{Y}}, M_{\mathrm{Z}})^{T} \tag{4.2}$$

The general displacement twists, $\Delta D_{\mathrm{t}}$, has three translational and three angular components. The compliance matrix is the inverse of the stiffness matrix, therefore [10]:

$$C_t = K_t^{-1} \tag{4.3}$$

By substituting Eq.(4.3) in Eq.(4.1), [10]:

$$\Delta D_t = C_t W_t \tag{4.4}$$

$\Delta D_{\mathrm{t}}$ can also be modeled by considering the joint compliances. First the joint wrenches, $W_{\mathrm{joint}}$, are calculated as reactions wrench to the tool wrench as follows:

$$W_{\mathrm{joint}} = J^{\mathrm{T}} W_{\mathrm{t}} \tag{4.5}$$

using the transposed geometric Jacobian $J^{\mathrm{T}}$. Those wrenches are then applied to the joint compliance to produce the joint displacement twists $\Delta D_{\mathrm{joint}}$

$$\Delta D_{\mathrm{joint}} = C_{\mathrm{joint}} W_{\mathrm{joint}} \tag{4.6}$$

By substituting (4.5) in (4.6) the resulting joint displacement twists are generated:

$$\Delta D_{\mathrm{joint}} = C_{\mathrm{joint}} J^{\mathrm{T}} W_{\mathrm{t}} \tag{4.7}$$

Finally, the joint displacement twists are propagated using the small twist approximation using the geometric Jacobian $J$ which expresses the sensitivity of the tool displacement twist $\Delta D_{\mathrm{t}}$ to small twists occurring at the joint locations:

$$\Delta D_{\mathrm{t}} = J \Delta D_{\mathrm{joint}} \tag{4.8}$$

Combining Eq.(4.4) with Eq.(4.8) establishes the relation between the applied tool wrench and the tool displacement twists due to the joint compliances [10]

$$\Delta D_{\mathrm{t}} = J C_{\mathrm{joint}} J^{\mathrm{T}} W_{\mathrm{t}} \tag{4.9}$$

The relation between the volumetric and joint compliance of a serial kinematics machine is then apparent [10]:

$$C_{\mathrm{t}} = J C_{\mathrm{joint}} J^{\mathrm{T}} \tag{4.10}$$

Eq.(4.9) can be understood as follows: the wrench $W_{\mathrm{t}}$ applied at the tool is first multiplied by $J^{\mathrm{T}}$ to calculate the applied wrench at each joint, or location where compliances are defined, then the joint

wrenches are multiplied by their respective compliances $C_{\text{joint}}$ to generate joint displacement twists which are then propagated back to the tool using $J$.

The general elastic model Eq.(4.9) is now contextualized to the use of the loaded telescopic double ball bar. The loaded telescopic double ball-bar only measures, $\rho$, the change in the relative distance between the tool ball and the workpiece ball. For a small change in the relative coordinates of the two balls, $\rho$ can be approximated by the projection, or dot product, of the relative translational displacement twist between the two balls with the unit vector, $\hat{b}$, describing the nominal axis of the loaded telescopic double ball bar, which is also its sensitive direction, as defined by the two end balls centers. The loaded telescopic double ball-bar response is then approximated by:

$$\rho = \hat{b}^{\mathrm{T}} \Delta D_{\mathrm{t}} \tag{4.11}$$

Therefore, by multiplying both sides of Eq.(4.9) by the transposed sensitive direction unit twist, $\hat{b}^{\mathrm{T}}$, Eq.(4.9) becomes:

$$\hat{b}^{\mathrm{T}} \Delta D_{\mathrm{t}} = \hat{b}^{\mathrm{T}} J C_{\text{joint}} J^{\mathrm{T}} W_{\mathrm{t}} \tag{4.12}$$

So that

$$\rho = \hat{b}^{\mathrm{T}} J C_{\text{joint}} J^{\mathrm{T}} W_{\mathrm{t}} \tag{4.13}$$

This equation can be summarized as follows: the sub-terms $J^{\mathrm{T}} W_{\mathrm{t}}$, $C_{\text{joint}} J^{\mathrm{T}} W_{\mathrm{t}}$, $J C_{\text{joint}} J^{\mathrm{T}} W_{\mathrm{t}}$ and $\hat{b}^{\mathrm{T}} J C_{\text{joint}} J^{\mathrm{T}} W_{\mathrm{t}}$ is the joint wrench, displacement at the joints due to its compliance, and the joint wrench, displacement at the workpiece, and displacement in the loaded telescopic double ball-bar sensitive direction, respectively.

In the test that will be presented, only two linear axes of a wFYXt machine topology, shown in Figure 4.2 are involved in the 2D circular test so that only forces in the XY plane and torques around z are considered for the wrenches and similarly only displacements in the XY plane and rotations around the Z-axis are considered for the twists.

The corresponding 2D compliance terms are retained and so the complete two axes compliance matrix has this form:

$$C_{\text{joint}_{6\times6}} = \begin{bmatrix} C_{\text{XXX}} & C_{\text{XYX}} & C_{\text{XCX}} & 0 & 0 & 0 \\ C_{\text{YXX}} & C_{\text{YYX}} & C_{\text{YCX}} & 0 & 0 & 0 \\ C_{\text{CXX}} & C_{\text{CYX}} & C_{\text{CCX}} & 0 & 0 & 0 \\ 0 & 0 & 0 & C_{\text{XXY}} & C_{\text{XYY}} & C_{\text{XCY}} \\ 0 & 0 & 0 & C_{\text{YXY}} & C_{\text{YYY}} & C_{\text{YCY}} \\ 0 & 0 & 0 & C_{\text{CXY}} & C_{\text{CYY}} & C_{\text{CCY}} \end{bmatrix} \tag{4.14}$$

where each compliance term has three subscripts representing from left to right the nature of the displacement caused, the nature of the applied force or torque, and the joint where the displacement and force are located.

Eq.(4.15) renders explicit the Jacobian definition in the X and Y directions, and around Z at the X and Y-joint.

$$J = \begin{bmatrix} \frac{\partial E_{\text{VX}}}{\partial E_{\text{XX}}} & \frac{\partial E_{\text{VX}}}{\partial E_{\text{YX}}} & \frac{\partial E_{\text{VX}}}{\partial E_{\text{CX}}} & \frac{\partial E_{\text{VX}}}{\partial E_{XY}} & \frac{\partial E_{\text{VX}}}{\partial E_{YY}} & \frac{\partial E_{\text{VX}}}{\partial E_{CY}} \\ \frac{\partial E_{\text{VY}}}{\partial E_{\text{XX}}} & \frac{\partial E_{\text{VY}}}{\partial E_{\text{YX}}} & \frac{\partial E_{\text{VY}}}{\partial E_{\text{CX}}} & \frac{\partial E_{\text{VY}}}{\partial E_{XY}} & \frac{\partial E_{\text{VY}}}{\partial E_{YY}} & \frac{\partial E_{\text{VY}}}{\partial E_{CY}} \\ \frac{\partial E_{\text{VC}}}{\partial E_{\text{XX}}} & \frac{\partial E_{\text{VC}}}{\partial E_{\text{YX}}} & \frac{\partial E_{\text{VC}}}{\partial E_{\text{CX}}} & \frac{\partial E_{\text{VC}}}{\partial E_{XY}} & \frac{\partial E_{\text{VC}}}{\partial E_{YY}} & \frac{\partial E_{\text{VC}}}{\partial E_{CY}} \end{bmatrix} \tag{4.15}$$

where $E_{\text{VX}}$ , $E_{\text{VY}}$ and $E_{\text{VC}}$ are the volumetric errors in the X and Y directions, and around Z (so it is called a C error), respectively. Additionally, $E_{\text{XX}}$, $E_{\text{YX}}$ and $E_{\text{CX}}$, are the geometric translational and rotational deviations at the X-joint in the X and Y directions, and around Z, respectively. Similar terms are defined for the Y-joint.

Table 4.1 depicts this reduced 2D compliance matrix for the X- and Y-axis with row and column headings to facilitate its interpretation.

Table 4.1.The simulated compliance matrices for the X- and Y-axis is a block diagonal matrix where only the orange and green colored cells are used.

| $C_{\text{joint}_{6\times6}}$ | | | | | | | |
|---|---|---|---|---|---|---|---|
| | Wrench components | | | | | | |
| Twist components | | $F_{XX}$ | $F_{YX}$ | $M_{CX}$ | $F_{XY}$ | $F_{YY}$ | $M_{CY}$ |
| | $\delta_{XX}$ | $C_{XXX}$ | $C_{XYX}$ | $C_{XCX}$ | 0 | 0 | 0 |
| | $\delta_{YX}$ | $C_{YXX}$ | $C_{YYX}$ | $C_{YCX}$ | 0 | 0 | 0 |
| | $\delta_{CX}$ | $C_{CXX}$ | $C_{CYX}$ | $C_{CCX}$ | 0 | 0 | 0 |
| | $\delta_{XY}$ | 0 | 0 | 0 | $C_{XXY}$ | $C_{XYY}$ | $C_{XCY}$ |
| | $\delta_{YY}$ | 0 | 0 | 0 | $C_{YXY}$ | $C_{YYY}$ | $C_{YCY}$ |
| | $\delta_{CY}$ | 0 | 0 | 0 | $C_{CXY}$ | $C_{CYY}$ | $C_{CCY}$ |

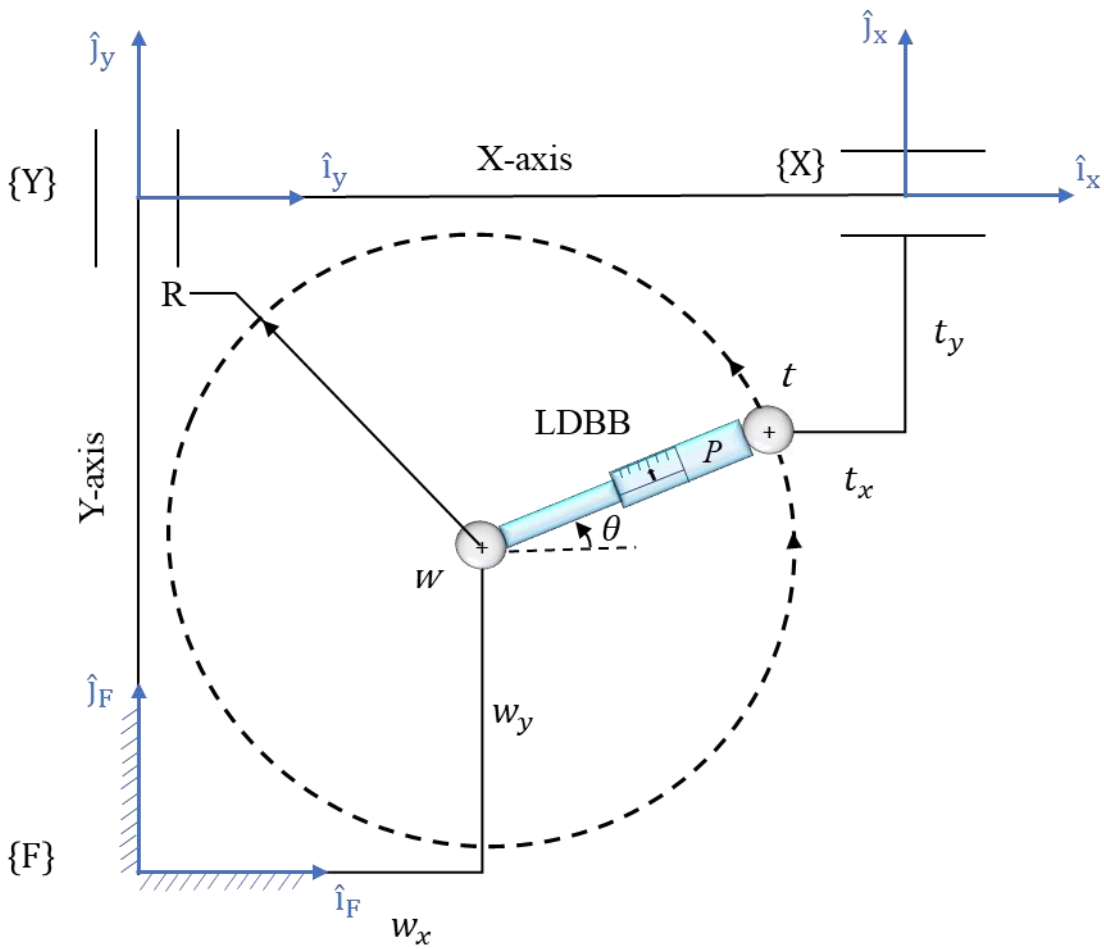


Figure 4.2. Conceptual diagram of the LDBB test setup and its circular trajectory in the XY machine tool plane. Note that $t_x$ and $t_y$ as shown are negative.

Accordingly, the general wrench at the tool, and at all locations where compliance is defined have the general form:

$$W_t = (F_{\mathrm{X}}, F_{\mathrm{Y}}, M_{\mathrm{Z}})^{\mathrm{T}}. \tag{4.16}$$

The LDBB sensitive direction is:

$$\hat{b} = [\cos(\theta) \quad \sin(\theta) \quad 0 \ ]^T \tag{4.17}$$

where θ is the angular position of the loaded telescopic double ball bar on its circular trajectory, see Figure 4.2. For the Jacobian matrix, only relevant columns ($E_{\mathrm{XX}}$, $E_{\mathrm{YX}}$, $E_{\mathrm{CX}}$, $E_{\mathrm{XY}}$, $E_{\mathrm{YY}}$, and $E_{\mathrm{CY}}$) are kept and the rest of the columns are removed due to test limitations to the XY plane. For example, $E_{\mathrm{CX}}$ is a small geometric angular deviation around the z-axis occurring at joint X. The six geometric deviations are small deviations in x, y, and around z occurring at the X- and Y-axis joints. For a test consisting of a complete circular test (2π radians) with one reading along the circle, Eq.(4.18) is used:

$$\rho_{1\times1} = \hat{B}^{\mathrm{T}}_{1\times3} \ J_{3\times 3\mathrm{n}} \ C_{\mathrm{joint}_{3\mathrm{n}\times3\mathrm{n}}} \ J^{\mathrm{T}}_{3\mathrm{n}\times3} \ W_{3\times1} \tag{4.18}$$

If *m* measurements are gathered and there are *n* compliance locations along the kinematic chain, (*n*=2 for two axes), then *m* occurrence of (4.13) are assembled in a single system to yield Eq.(4.19):

$$\rho_i = \hat{B}^{\mathrm{T}}{}_i \ J_i \ C_{\mathrm{joint}} \ J^{\mathrm{T}}{}_i \ W_i \qquad i = 1, \mathrm{m} \tag{4.19}$$

where,

$$\hat{B}_i = \begin{bmatrix} \cos\theta_i \\ \sin\theta_i \\ 0 \end{bmatrix} \qquad i = 1, \mathrm{m} \tag{4.20}$$

$$J_i = \begin{bmatrix} 1 & 0 & -t_{\mathrm{y}} & 1 & 0 & -t_{\mathrm{y}} \\ 0 & 1 & t_{\mathrm{x}} & 0 & 1 & x_i + t_{\mathrm{x}} \\ 0 & 0 & 1 & 0 & 0 & 1 \end{bmatrix} \qquad i = 1, \mathrm{m} \tag{4.21}$$

where $t_{\mathrm{x}}$, $t_{\mathrm{y}}$ and $x_i$ are the coordinates of the tool ball in the X-axis frame and the joint coordinates for axis X respectively, as shown in Figure 4.2, and finally:

$$W_i = \begin{bmatrix} F_{\mathrm{X}_i} \\ F_{\mathrm{Y}_i} \\ M_{\mathrm{Z}_i} \end{bmatrix} \qquad i = 1, \mathrm{m} \tag{4.22}$$

In Eq.(4.22), the term $M_{Z_i}$ is equal to zero because the ball bar cannot apply torque as friction forces between the ball and its socket are assumed negligible.

## 4.4. Numerical Jacobian

In order to estimate the compliance values the relationship between the observed ball bar length change and the compliance at the joints is linearized using a computed wrench Jacobian matrix as follows:

$$\rho_{\mathrm{m}\times 1} = J_{\mathrm{W}_{\mathrm{m}\times\mathrm{n}}} C_{\mathrm{n}\times 1} \tag{4.23}$$

where the $J_{\mathrm{W}}$ is the derivatives of loaded telescopic double ball-bar change ($\partial\rho$) with respect to the compliance ($\partial C$) at the joints in the following:

$$J_{\mathrm{W}_{i,j}} = \frac{\partial \rho_i}{\partial C_j} \qquad \begin{array}{l} i = 1, \mathrm{m} \\ j = 1, 9\mathrm{n} \end{array} \tag{4.24}$$

An approximate solution in the least square for the required compliance changes needed to produce the measured displacements is given by:

$$C_{\mathrm{n}\times 1} = J^{+}_{\mathrm{W}_{\mathrm{n}\times\mathrm{m}}} \rho_{\mathrm{m}\times 1} \tag{4.25}$$

where $J^{+}_{\mathrm{W}}$ is the pseudo-inverse of the linearized wrench Jacobian.

Figure 4.3 shows the free body diagram of the loaded telescopic double ball-bar and main machine model components. $F_{\mathrm{b}}$ is the generated force by the loaded telescopic double ball-bar.

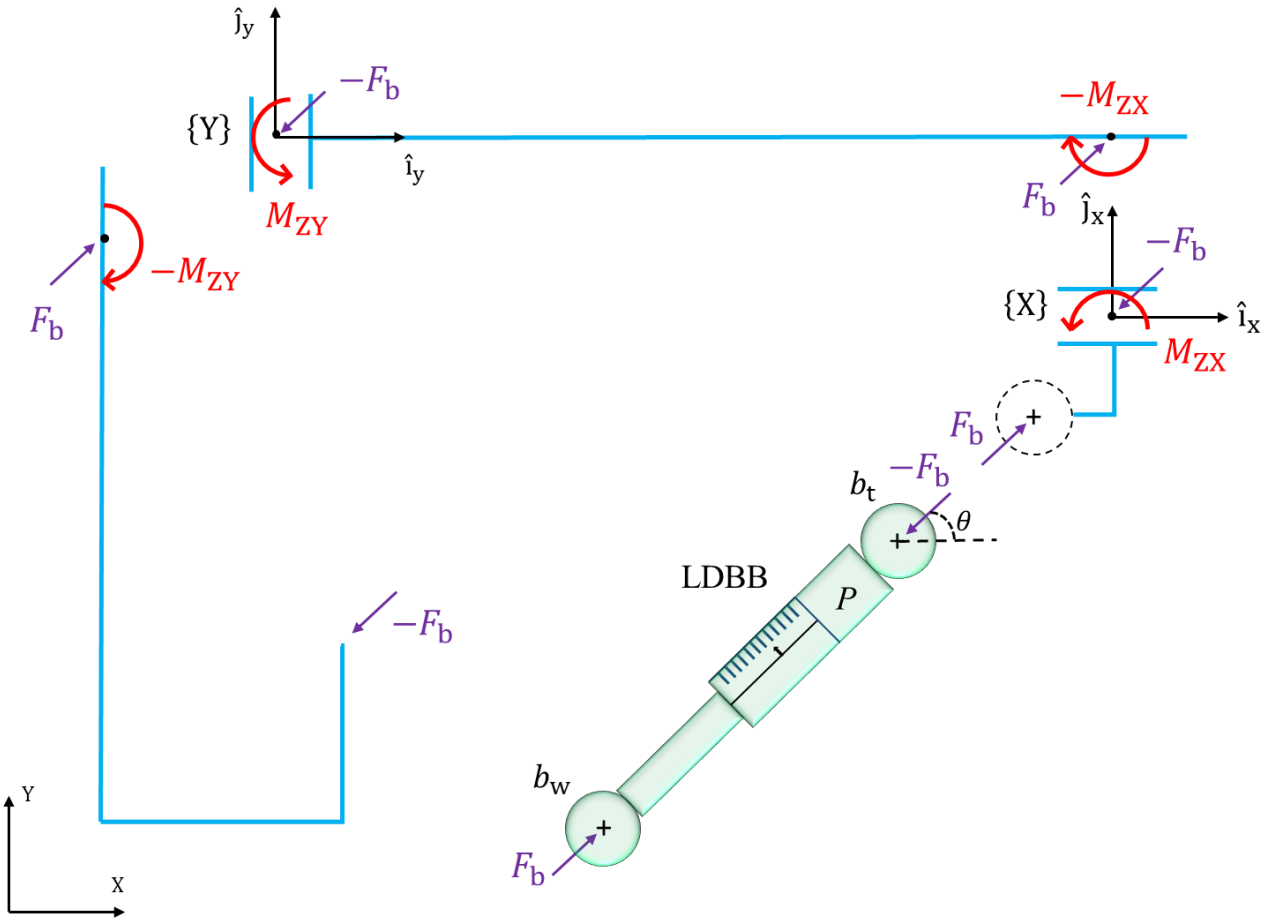


Figure 4.3. Free body diagram of the LDBB and main machine model components.

Figure 4.4 illustrates conceptually the on-axis compliance terms $C_{XXX}$ and $C_{YYY}$, the lateral terms $C_{YYX}$ and $C_{XXY}$ as well as the torsional terms $C_{CCX}$ and $C_{CCY}$. The cross-compliance terms are not shown.

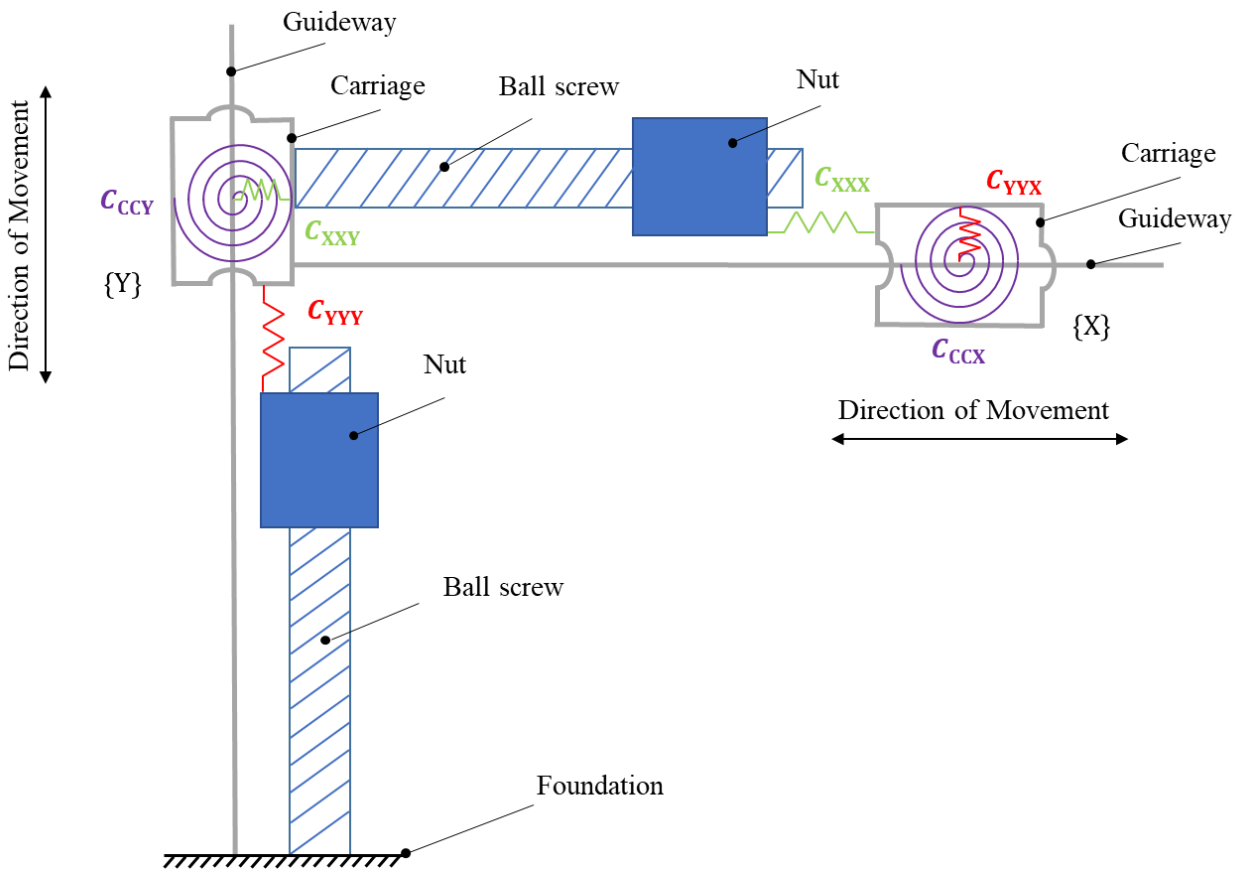


Figure 4.4. 2-D conceptual diagram of the machine with the location of the on-axis, lateral, and torsional compliances (the cross-compliance terms are not illustrated).

## 4.5. Simulation

The compliance estimation process using the loaded telescopic double ball-bar is first validated through simulations. Figure 4.5 presents the data flow for the simulation and estimation of the 2-axis linear axis of the 5 -axis machine tool.

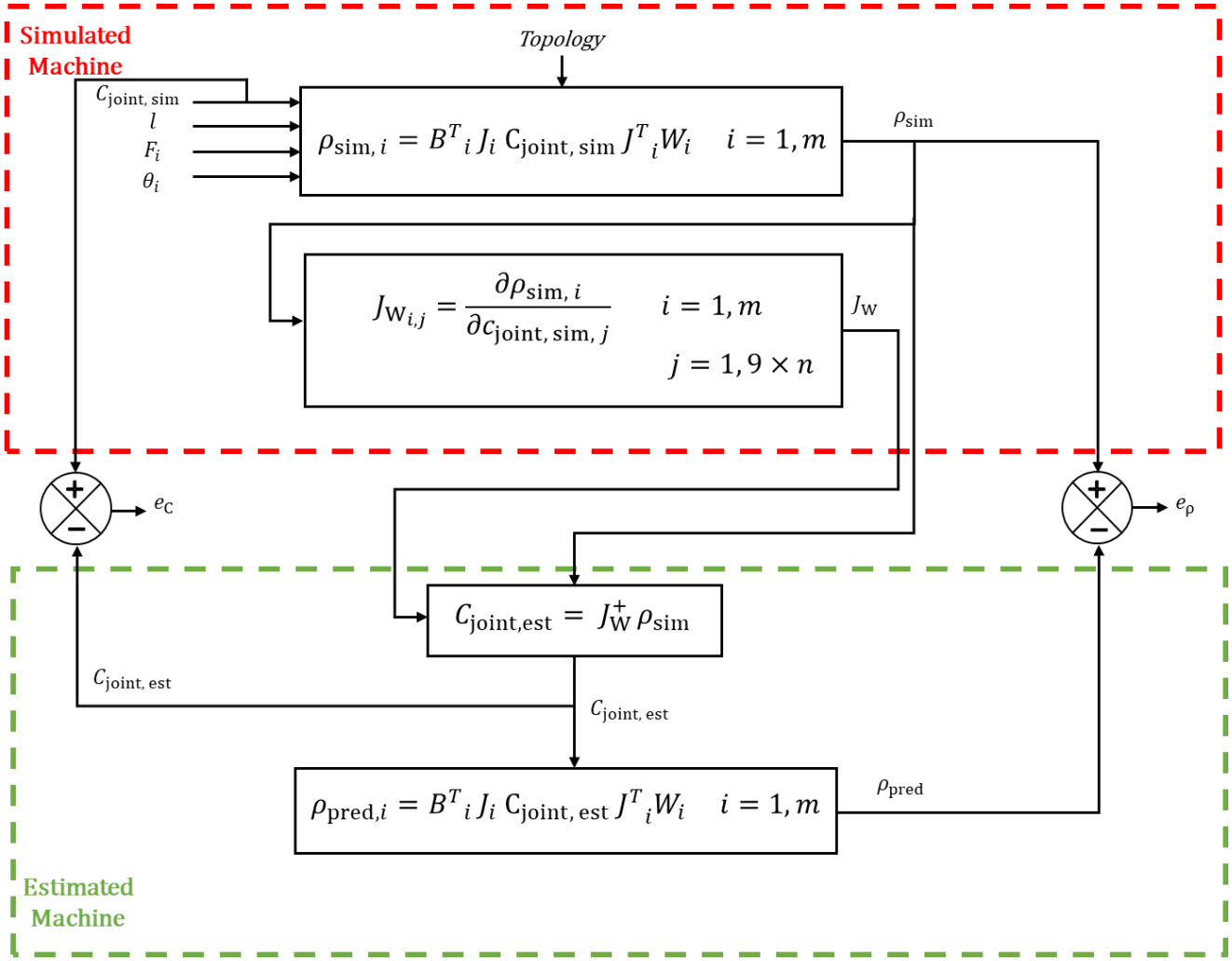


**W**: simulated wrench at the tool

**F**: loaded telescopic double ball-bar force

**l**: loaded telescopic double ball-bar length

ɵ: loaded telescopic double ball-bar rotation angle

***C* joint, sim**: simulated compliance for each axis

***C* joint, est**: estimated compliance for each axis

***ρ*sim**: simulated loaded telescopic double ball-bar reading

***ρ*pred**: predicted loaded telescopic double ball-bar reading

***e*c**: compliance error

***e*ρ**: loaded telescopic double ball-bar reading error

Figure 4.5. Data flow for the simulation for machine tool compliance.

As depicted in the simulated machine in Figure 4.5, joint compliance values based on values in the literature review are assigned to the machine joints (axes) using $C_{\mathrm{joint,sim}}$. The wrench at the tool, $W$, applied by the loaded telescopic double ball-bar causes wrenches at the joints calculated using Eq.(4.5). Then Eq.(4.19) calculates the loaded telescopic double ball-bar length change readings one at a time due to the compliance and resulting wrench at the tool. As shown in the estimated machine in Figure 4.5, the simulated compliance matrices are estimated using Eq.(4.25). Furthermore, Eq.(4.19) is used to predict simulated loaded telescopic double ball-bar readings by having estimated compliance matrices. The simulated and predicted loaded telescopic double ball-bar readings are compared for confirmation of the intermediate simulated values.

### 4.5.1. Simulation results and discussion

The compliance terms relevant for the 2D case are simulated as non-zero values as listed in Table 4.2 The loaded telescopic double ball bar has a nominal length of R=150 mm and the applied force is F=100 N. Table 4.3 shows the estimated compliances. As Table 4.3 indicates, the estimated values differ significantly from the simulated ones. However, as Figure 4.7 shows, the simulated and predicted reading obtained from the simulated and estimated compliances of Table 4.2 and Table 4.3 are similar. In order to better understand the reason for this, separate simulations are conducted for each compliance. As indicated in Table 4.4, the compliance terms $\mathrm{C_{XXX}}$ and $\mathrm{C_{XXY}}$ produce the same loaded telescopic double ball-bar readings. Compliances $C_{\mathrm{XXX}}$ and $C_{\mathrm{XXY}}$ are always subjected to the same force and cause displacements always in the same directions so that they cannot be distinguished in their effect; they are confounded. Other confounded compliances can be recognized by visual inspection of Table 4.4. Compliance terms including $C_{\mathrm{XYX}}$, $C_{\mathrm{YXX}}$, $C_{\mathrm{XYY}}$ and $C_{\mathrm{YXY}}$ generate the same readings. $C_{\mathrm{YYX}}$ and $C_{\mathrm{YYY}}$ are also producing the same readings pattern. For the rotary compliance terms, $C_{\mathrm{XCY}}$, $C_{\mathrm{CXY}}$ produce identical readings. $C_{\mathrm{YCY}}$, $C_{\mathrm{CYY}}$ yield similar readings. It is worth mentioning that the only compliance term which has a unique shape and readings is $C_{\mathrm{CCY}}$, an angular compliance term. Finally, there are five compliance terms including $C_{\mathrm{XCX}}$, $C_{\mathrm{YCX}}$, $C_{\mathrm{CXX}}$, $C_{\mathrm{CYX}}$ and $C_{\mathrm{CCX}}$ which produce no readings and cannot be estimated from the data.

Table 4.2. Simulated compliance ( $^{mm}/_{N}$ ) of the X and Y axes simultaneously with the simulated value of all compliance terms.

| $C_{\text{joint}_{6\times6}}$ simulated | | | | | | | |
|---|---|---|---|---|---|---|---|
| | | Wrench components | | | | | |
| | | $F_{XX}$ | $F_{YX}$ | $M_{CX}$ | $F_{XY}$ | $F_{YY}$ | $M_{CY}$ |
| Twist components | $\delta_{XX}$ | 1.1E-04 | 1.2E-04 | 1.3E-06 | 0 | 0 | 0 |
| | $\delta_{YX}$ | 2.1E-04 | 2.2E-04 | 2.3E-06 | 0 | 0 | 0 |
| | $\delta_{CX}$ | 3.1E-06 | 3.2E-06 | 3.3E-08 | 0 | 0 | 0 |
| | $\delta_{XY}$ | 0 | 0 | 0 | 4.4E-04 | 4.5E-04 | 4.6E-06 |
| | $\delta_{YY}$ | 0 | 0 | 0 | 5.4E-04 | 5.5E-04 | 5.6E-06 |
| | $\delta_{CY}$ | 0 | 0 | 0 | 6.4E-06 | 6.5E-06 | 6.6E-08 |

Table 4.3. Estimated compliance matrices ( $^{mm}/_{N}$ ) for the X and Y axes simultaneously in the presence of non-zero simulated values of all compliance terms.

| $C_{\text{joint}_{6\times6}}$ Estimated | | | | | | | |
|---|---|---|---|---|---|---|---|
| | | Wrench | | | | | |
| | | $F_{XX}$ | $F_{YX}$ | $M_{CX}$ | $F_{XY}$ | $F_{YY}$ | $M_{CY}$ |
| Twist | $\delta_{XX}$ | 2.75E-04 | 3.3E-04 | 0 | 0 | 0 | 0 |
| | $\delta_{YX}$ | 3.3E-04 | 3.85E-04 | 0 | 0 | 0 | 0 |
| | $\delta_{CX}$ | 0 | 0 | 0 | 0 | 0 | 0 |
| | $\delta_{XY}$ | 0 | 0 | 0 | 2.75E-04 | 3.3E-04 | 5.5E-06 |
| | $\delta_{YY}$ | 0 | 0 | 0 | 3.3E-04 | 3.85E-04 | 6.05E-06 |
| | $\delta_{CY}$ | 0 | 0 | 0 | 5.5E-06 | 6.05E-06 | 6.6E-08 |

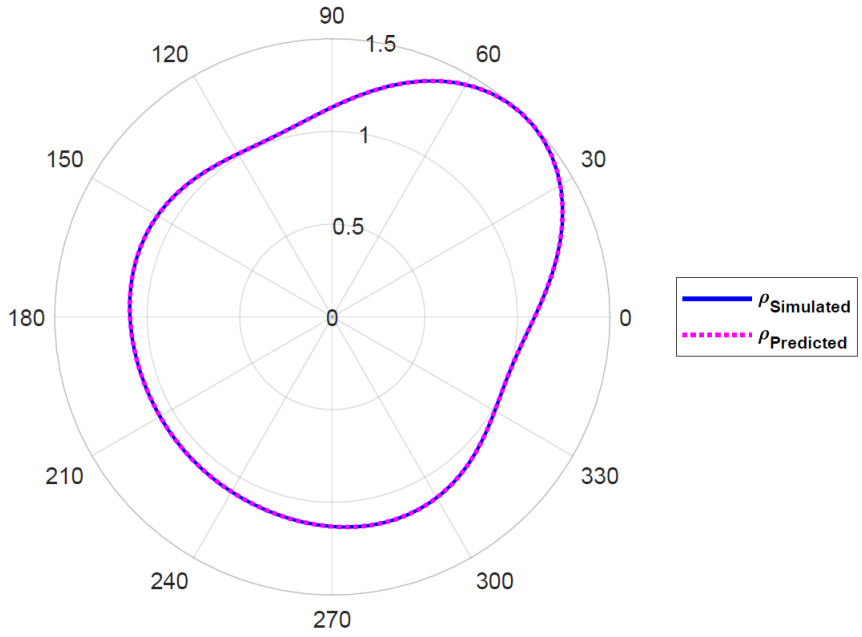


Figure 4.6. Figure 4.7. Simulated and predicted reading obtained from Table 4.2 and Table 4.3. (One unit of the radial scale represents 15.0 µm).

Table 4.4. Associated patterns which generated by the unique compliance terms, (One unit of the radial scale represents 15.0 µm).

| List of compliances each producing the pattern shown | | |
|---|---|---|
| $C_{XXX}$ , $C_{XXY}$ | $C_{XCY}$, $C_{CXY}$ | $C_{XYX}$, $C_{YXX}$, $C_{XYY}$ , $C_{YXY}$ |
| 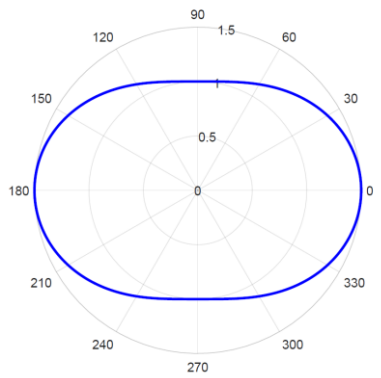 | 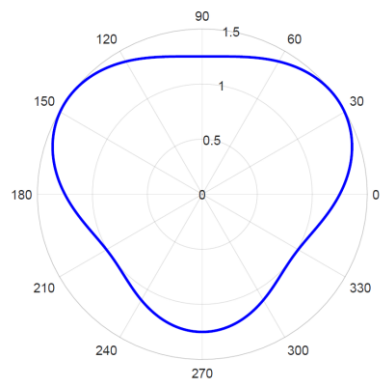 | 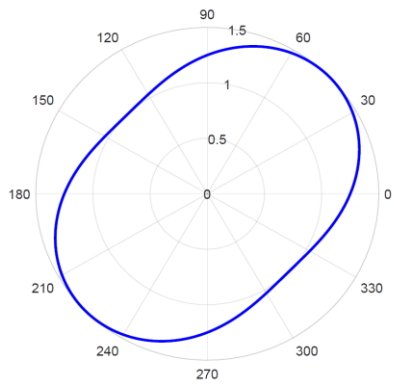 |
| $C_{YCY}$, $C_{CYY}$ | $C_{YYX}$, $C_{YYY}$ | $C_{CCY}$ |
| 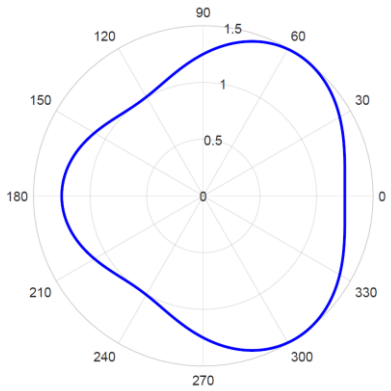 | 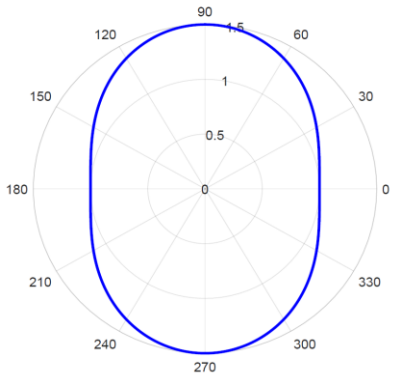 | 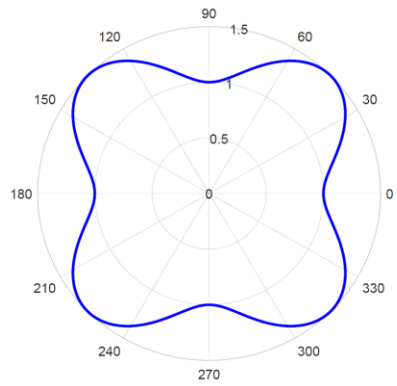 |

The numerical Jacobian has 18 columns which corresponds to each compliance terms. By using the MATLAB command, the condition number and rank of the numerical Jacobian matrix are 1.7e+34 and 6, respectively. The rank illustrates that there are only six independent columns out of 18 in the matrix. If identical numerical Jacobian matrix columns exist all but one of the corresponding terms are removed. Terms corresponding to null columns are also removed. The final set of retained compliances includes $C_{\mathrm{XXX}}$, $C_{\mathrm{XYX}}$, $C_{\mathrm{YYY}}$, $C_{\mathrm{CXY}}$, $C_{\mathrm{CYY}}$ and $C_{\mathrm{CCY}}$. After pruning, the condition number reduces to 9742 and the rank of the numerical Jacobian matrix remains equal to six. To verify that the retained compliance terms are sufficient to explain the readings due to any values of the full set of compliances, a supplementary simulation is conducted with the simulated compliance terms in Table 4.2 and only estimating the retained six compliance terms. Table 4.5 lists the six estimated

compliances. Figure 4.8 demonstrates that the predicted loaded telescopic double ball-bar readings using the six estimated compliances of Table 4.5 are similar to those simulated using the simulated non-zero values for all compliances from Table 4.2. As a result, it can be said that the six estimated compliances are equivalent compliances as they are compliances that would produce similar readings to a potentially different set of actual compliances. The circular test is not sufficiently rich to allow to separate the contributing compliances.

Table 4.5. Estimated compliance matrices ( $^{mm}/_{N}$ ) for the X and Y axes simultaneously with the presence of a value of six compliance terms.

| $C_{\text{joint}_{6\times6}}$ Estimated | | | | | | | |
|---|---|---|---|---|---|---|---|
| | | Wrench | | | | | |
| | | $F_{XX}$ | $F_{YX}$ | $M_{CX}$ | $F_{XY}$ | $F_{YY}$ | $M_{CY}$ |
| Twist | $\delta_{XX}$ | 5.5E-04 | 1.32E-03 | 0 | 0 | 0 | 0 |
| | $\delta_{YX}$ | 0 | 0 | 0 | 0 | 0 | 0 |
| | $\delta_{CX}$ | 0 | 0 | 0 | 0 | 0 | 0 |
| | $\delta_{XY}$ | 0 | 0 | 0 | 0 | 0 | 0 |
| | $\delta_{YY}$ | 0 | 0 | 0 | 0 | 7.7E-04 | 0 |
| | $\delta_{CY}$ | 0 | 0 | 0 | 1.1E-05 | 1.21E-05 | 6.6E-08 |

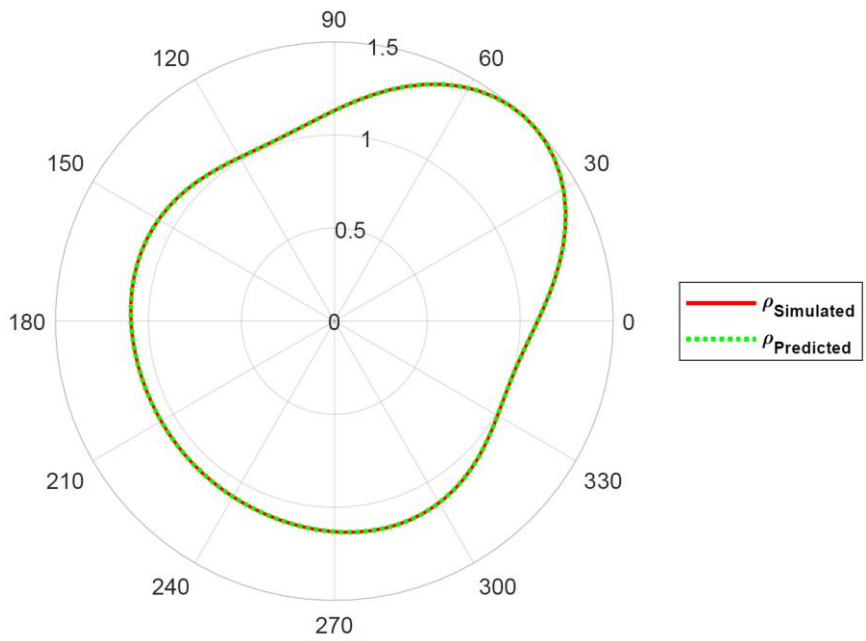


Figure 4.8. Simulated and predicted readings were acquired using compliance as simulated in Table 4.2 and as estimated in Table 4.5. (One unit of the radial scale represents 15.0 µm).

## 4.6. Results and discussion

The test is conducted in the XY plane of the machine illustrated in Figure 4.1. The length of the loaded telescopic double ball bar was 150 mm and the feed rate was 2000 mm/min. Length change readings are taken over a full circle starting with the tool ball relative to the workpiece ball aligned with the negative X-axis. Seven different runs are performed with levels of pressure of 0.4, 1, 2, 3, 4, 5, and 6 bars applied to the loaded telescopic double ball-bar device corresponding to forces of 36, 112, 238, 364, 490, 616, and 742N, respectively. Using Eq.(4.26) the lowest force (36N) is taken as a reference near zero force thus assumed to only be affected by such error sources as geometric errors and those readings are deducted from the raw readings at other force levels in order to eliminate effects assumed not to vary with the applied force.

$$\begin{aligned}
\Delta\rho_{112-36} &= \rho_{112\text{ N}} - \rho_{36\text{ N}} \\
\Delta\rho_{238-36} &= \rho_{238\text{ N}} - \rho_{36\text{ N}} \\
\Delta\rho_{364-36} &= \rho_{364\text{ N}} - \rho_{36\text{ N}} \\
\Delta\rho_{490-36} &= \rho_{490\text{ N}} - \rho_{36\text{ N}} \\
\Delta\rho_{616-36} &= \rho_{616\text{ N}} - \rho_{36\text{ N}} \\
\Delta\rho_{742-36} &= \rho_{742\text{ N}} - \rho_{36\text{ N}}
\end{aligned} \tag{4.26}$$

As mentioned above, a similar process is used for the corresponding force levels, where the lowest force level (36 N) is subtracted from the rest of the forces. Eq.(4.27) illustrates the force subtraction process for each corresponding force separately.

$$\begin{aligned}
\Delta F_{112-36} &= F_{112\,\mathrm{N}} - F_{36\,\mathrm{N}} \\
\Delta F_{238-36} &= \mathrm{F}_{238\,\mathrm{N}} - F_{36\,\mathrm{N}} \\
\Delta F_{364-36} &= F_{364\,\mathrm{N}} - F_{36\,\mathrm{N}} \\
\Delta F_{490-36} &= F_{490\,\mathrm{N}} - F_{36\,\mathrm{N}} \\
\Delta F_{616-36} &= F_{616\,\mathrm{N}} - F_{36\,\mathrm{N}} \\
\Delta F_{742-36} &= F_{742\,\mathrm{N}} - F_{36\,\mathrm{N}}
\end{aligned} \tag{4.27}$$

### 4.6.1. Global (overall/aggrigated) compliance

To estimate the global compliance of the machine tool, as depicted in Eq.(4.28) all the corresponding force data from 76 to 706 N (differential forces) are fed to the estimator to generate one set of compliance values. In Eq.(4.28), $J_{\Delta\mathrm{F}}^{+}$ is the pseudo-inverse of the numerical Jacobian generated by the change of relevant force in the specific local force interval. Subsequently, that set of estimated compliance is used to predict all the loaded telescopic double ball-bar readings as illustrated in Figure 4.9. The estimated compliance values for the X- and Y-axis when using all force levels at once are listed in Table 4.6.

$$\begin{bmatrix} C_{\mathrm{XXX}_{\mathrm{est}}} \\ C_{\mathrm{XYX}_{\mathrm{est}}} \\ C_{\mathrm{YYY}_{\mathrm{est}}} \\ C_{\mathrm{CXY}_{\mathrm{est}}} \\ C_{\mathrm{CYY}_{\mathrm{est}}} \\ C_{\mathrm{CCY}_{\mathrm{est}}} \end{bmatrix}_{6\times1} = \begin{bmatrix} \boldsymbol{J}_{\Delta\mathbf{F}_{112-36}} \\ \boldsymbol{J}_{\Delta\mathbf{F}_{238-36}} \\ \boldsymbol{J}_{\Delta\mathbf{F}_{364-36}} \\ \boldsymbol{J}_{\Delta\mathbf{F}_{490-36}} \\ \boldsymbol{J}_{\Delta\mathbf{F}_{616-36}} \\ \boldsymbol{J}_{\Delta\mathbf{F}_{742-36}} \end{bmatrix}^{+}_{6\times6\mathrm{m}} \begin{bmatrix} \Delta\boldsymbol{\rho}_{\mathbf{112-36}} \\ \Delta\boldsymbol{\rho}_{\mathbf{238-36}} \\ \Delta\boldsymbol{\rho}_{\mathbf{364-36}} \\ \Delta\boldsymbol{\rho}_{\mathbf{490-36}} \\ \Delta\boldsymbol{\rho}_{\mathbf{616-36}} \\ \Delta\boldsymbol{\rho}_{\mathbf{742-36}} \end{bmatrix}_{6\mathrm{m}\times1} \tag{4.28}$$

Table 4.6. Estimated global compliance value ( $^{mm}/_{N}$ ) of X and Y axes using all pressure data at once.

| $C_{X_{Estimated}}$ and $C_{Y_{Estimated}}$ | | | | | | | |
|---|---|---|---|---|---|---|---|
| | | Wrench | | | | | |
| | | $F_{XX}$ | $F_{YX}$ | $M_{CX}$ | $F_{XY}$ | $F_{YY}$ | $M_{CY}$ |
| Twist | $\delta_{XX}$ | 7.61E-05 | 2.27E-07 | 0 | 0 | 0 | 0 |
| | $\delta_{YX}$ | 0 | 0 | 0 | 0 | 0 | 0 |
| | $\delta_{CX}$ | 0 | 0 | 0 | 0 | 0 | 0 |
| | $\delta_{XY}$ | 0 | 0 | 0 | 0 | 0 | 0 |
| | $\delta_{YY}$ | 0 | 0 | 0 | 0 | 6.05E-05 | 0 |
| | $\delta_{CY}$ | 0 | 0 | 0 | 1.08E-09 | 5.35E-10 | -1.73E-11 |

Figure 4.9 presents the experimental and predicted loaded telescopic double ball-bar readings from 76 to 706 N force. All the predicted readings are generated using one set of compliance. At maximum force, the radial displacements in the *X*- and *Y*- positive sense for experimental and prediction are 0.0535 mm and 0.0422 mm, and 0.0523 mm and 0.0416 mm, respectively. As depicted in the Figure/diagram, by increasing the applied force, the loaded telescopic double ball-bar readings increase to deviate from the nominal trajectory up to its maximum level at 706 N force. When all data is used to estimate compliances the predicted behavior should be entirely linear with the applied force. However, as can be seen, from Figure 4.9 at 76 N force the results exhibit a non-linear behavior and there is a difference between experimental and predicted readings. However, at higher force levels the response appears linear and the prediction agrees more closely with the experimental readings.

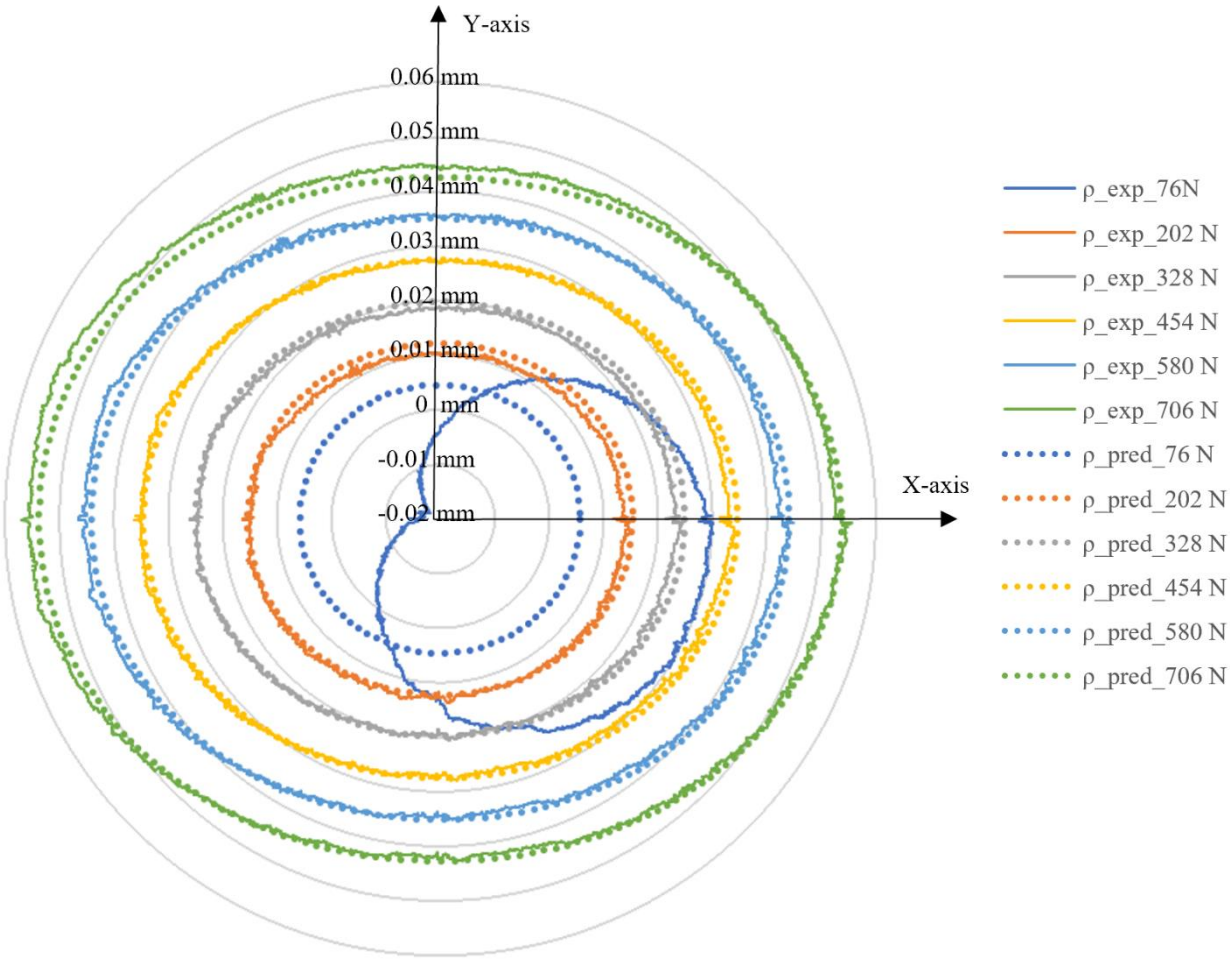


Figure 4.9.Experimental and Predicted global loaded telescopic double ball bar readings for X and Y-axis simultaneously with six different levels of applied force without geometric errors. ρ_exp and ρ_pred are the experimental and predicted readings of a loaded telescopic double ball bar.

In order to distinguish the dominant global compliance parameters simulated readings are generated for each estimated global compliance parameter individually. As shown in Figure 4.10 as well as Figure 4.11 the dominant compliance parameters are $C_{\mathrm{XXX}}$ and $C_{\mathrm{YYY}}$. A precise mechanical interpretation is not possible because those dominant compliances, which are related to the axis feed drive systems, are confounded with cross-compliances, which are associated with guiding systems. The global value of $C_{\mathrm{CCY}}$ compliance is always negative which means that adding a four-lobed shape at 45 degrees to the one produced by a positive compliance $C_{\mathrm{CCY}}$ is helping to reduce the model prediction residuals in a least-square sense. However, its value is very small and its impact on the loaded circular test readings is predicted to be around 0.00007 mm peak-to-peak which is less than one-third of the 0.00024 mm resolution of the LDBB position readout. Figure 4.11 shows predicted

reading of less than 0.00017 peak-to-peak for the largest non-dominant compliances which is also less than the LDBB resolution. We feel that these estimated non-dominant compliance values are not reliable. Although the estimated values repeat as will be shown in section 4.7.

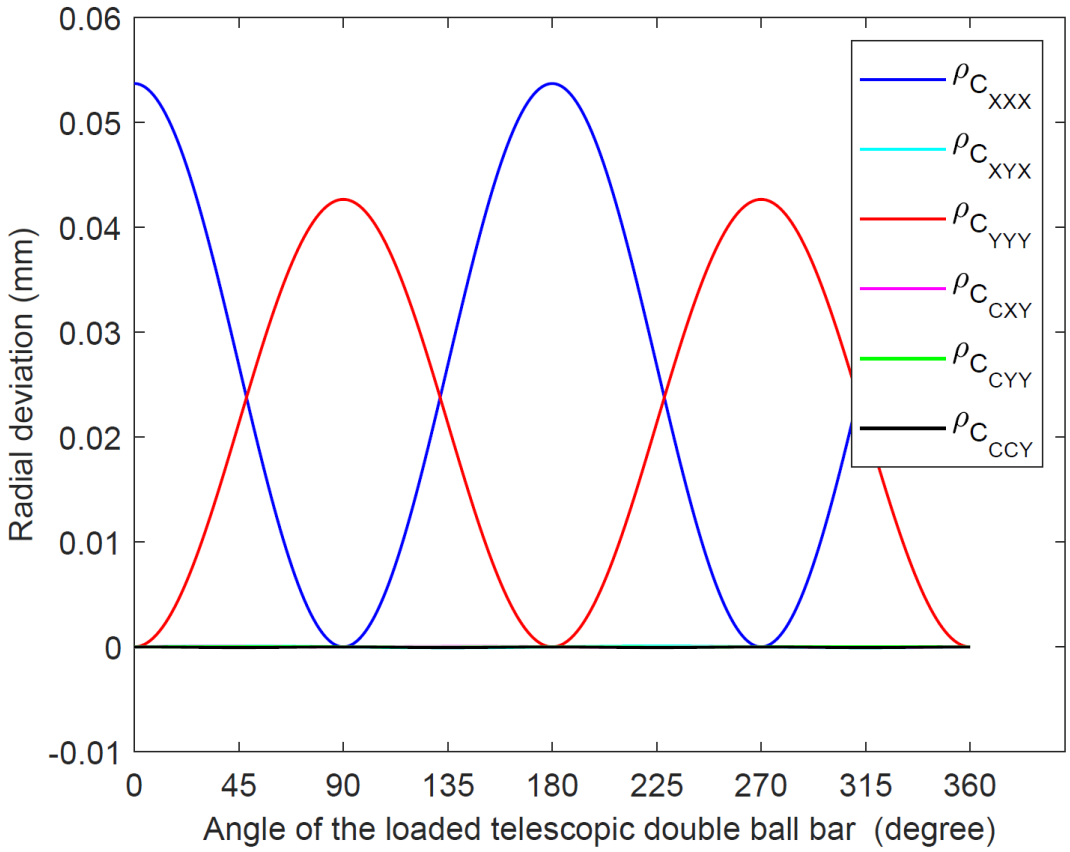


Figure 4.10.Predicted readings of the loaded double ball bar (radial deviation versus the angle of the ball bar with the X-axis during the circular test) from the estimated global compliance parameters ($C_{\mathrm{XXX}}$, $C_{\mathrm{XYX}}$, $C_{\mathrm{YYY}}$ , $C_{\mathrm{CXY}}$, $C_{\mathrm{CYY}}$ and $C_{\mathrm{CCY}}$) at a highest force (706 N).

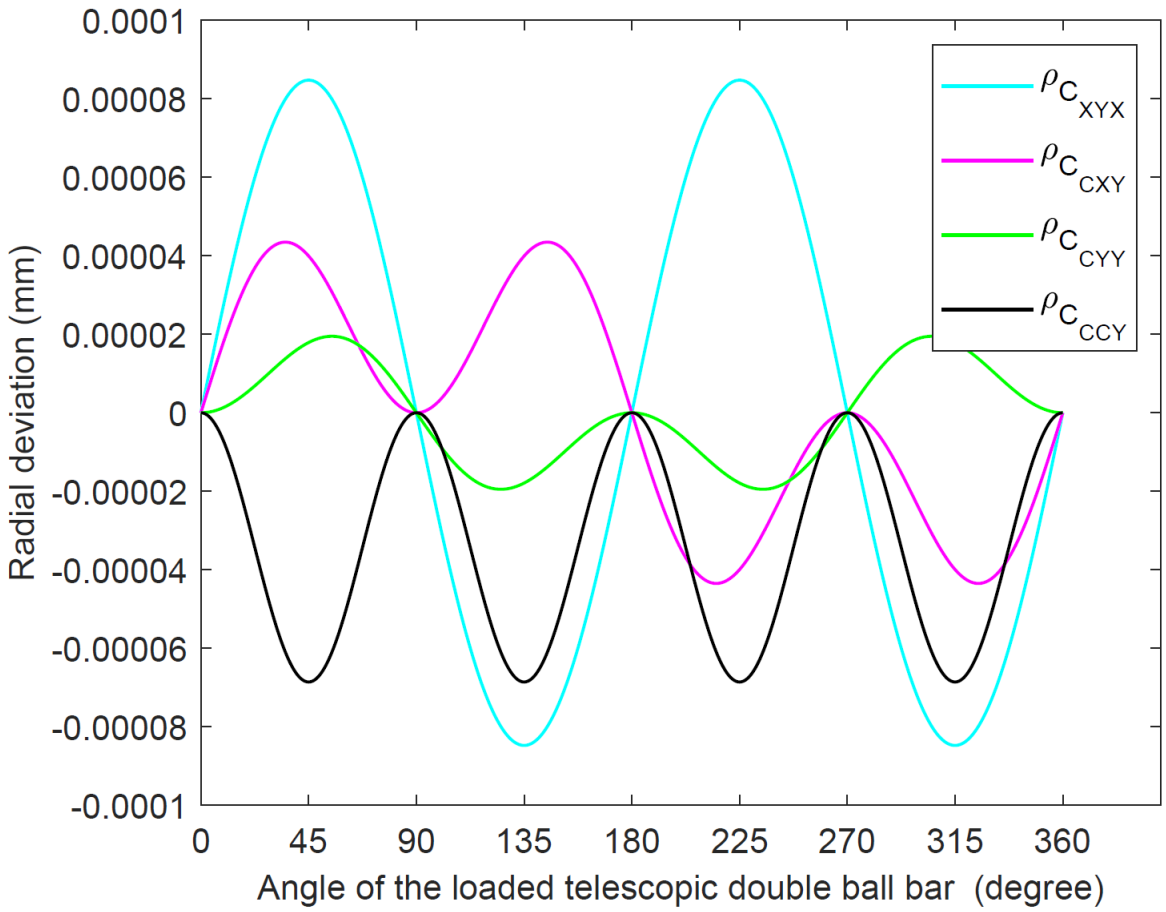


Figure 4.11. Predicted readings of the loaded double ball bar (radial deviation versus the angle of the ball bar with the X-axis during the circular test) from the estimated global compliance parameters ($C_{\mathrm{XYX}}$, $C_{\mathrm{CXY}}$, $C_{\mathrm{CYY}}$ and $C_{\mathrm{CCY}}$) at the highest force (706 N).

### 4.6.2. Local compliance

Local compliances are estimated using two force levels ([112-36, 238-36], [238-36, 364-36], etc.). For example, for the force level [238-36, 364-36], the local compliance terms are estimated using Eq.(4.29). The $\Delta\rho_{238-36}$ and $\Delta\rho_{364-36}$ are obtained through Eq.(4.26).

$$[C_{\mathrm{est}}]_{6\times1} = \begin{bmatrix} J_{\Delta \mathrm{F}_{238-36}} \\ J_{\Delta \mathrm{F}_{364-36}} \end{bmatrix}^{+}_{6\times2m} \begin{bmatrix} \Delta\rho_{238-36} \\ \Delta\rho_{364-36} \end{bmatrix}_{2m\times1} \tag{4.29}$$

Then the associated predicted readings are produced for each set of forces. Figure 4.12 shows corresponding experimental and predicted local readings for an individual set of differential forces. As the force increases, the predicted local readings better follow the experimental readings. The non-linear behavior can still be seen at 76 N force.

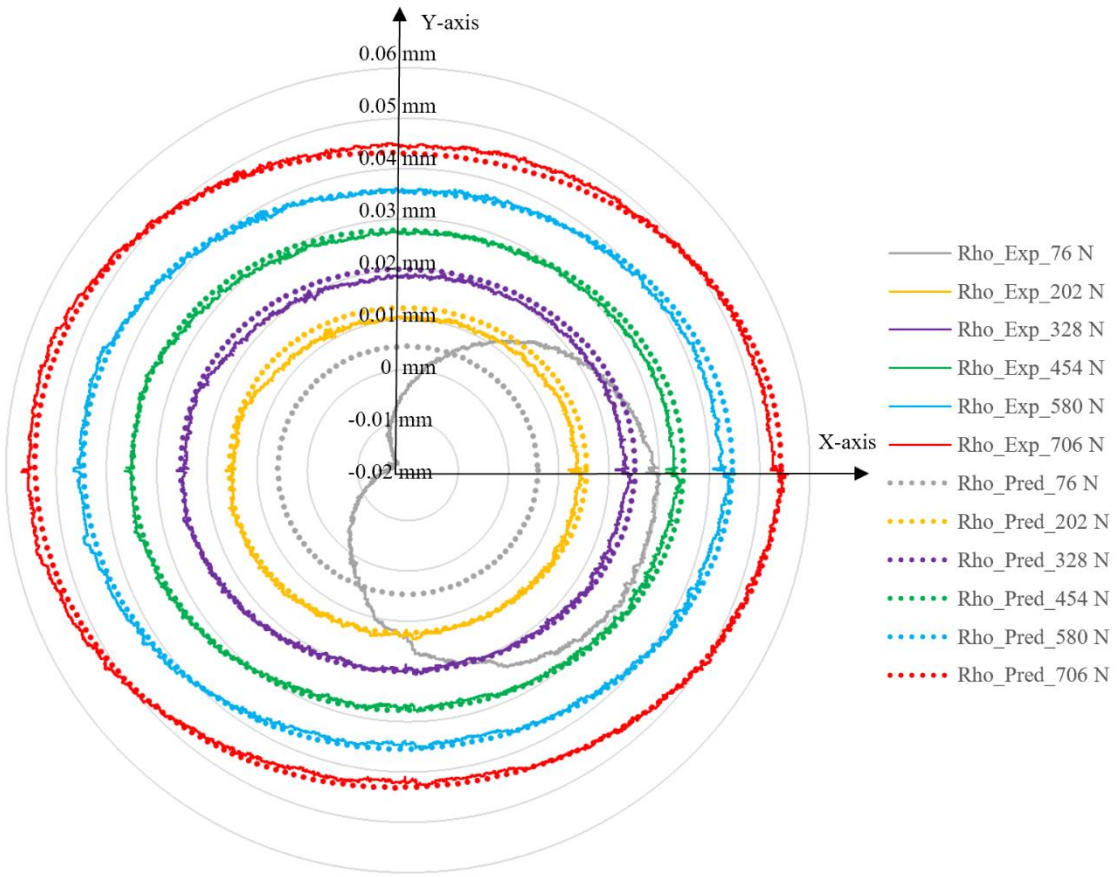


Figure 4.12. Experimental and predicted loaded telescopic double ball bar readings with six different force levels without geometric errors and predicted using locally estimated compliance values. ρ_exp and ρ_pred are the experimental and predicted readings of a loaded telescopic double ball bar.

Estimated local compliance values for each set of unique forces are shown in Table 4.7.

Table 4.7. Estimated local compliances values for a different set of pressures.

| Force (N) | $C_{\mathrm{XXX}}$ ( $^{\mathrm{mm}}/_{\mathrm{N}}$ ) | $C_{\mathrm{XYX}}$ ( $^{\mathrm{mm}}/_{\mathrm{N}}$ ) | $C_{\mathrm{YYY}}$ ( $^{\mathrm{mm}}/_{\mathrm{N}}$ ) | $C_{\mathrm{CXY}}$ ( $^{\mathrm{rad}}/_{\mathrm{N}}$ ) | $C_{\mathrm{CYY}}$ ( $^{\mathrm{rad}}/_{\mathrm{N}}$ ) | $C_{\mathrm{CCY}}$ ( $^{\mathrm{rad}}/_{\mathrm{N\ mm}}$ ) |
|---|---|---|---|---|---|---|
| $\Delta F_{1-2}$ (76 and 202) | 7.39E -05 | -1.26E-06 | 5.88E-05 | 2.52E-07 | 4.58E-07 | -1.18E-10 |
| $\Delta F_{2-3}$ (202 and 328) | 7.31E-05 | -9.09E-07 | 5.79E-05 | 3.87E-08 | -1.92E-08 | -3.21E-11 |
| $\Delta F_{3-4}$ (328 and 454) | 7.47E-05 | -4.09E-07 | 5.93E-05 | 7.72E-09 | -1.87E-08 | -2.29E-11 |
| $\Delta F_{4-5}$ (454 and 580) | 7.58E-05 | 8.50E-08 | 6.03E-05 | -5.12E-09 | -2.09E-08 | -2.52E-11 |
| $\Delta F_{5-6}$ (580 and 706) | 7.68E-05 | 5.49E-07 | 6.10E-05 | -1.54E-08 | -1.78E-08 | -9.59E-12 |

Figure 4.13 illustrates the estimated experimental compliance results. Most local compliances increase with the applied force such as $C_{\mathrm{XXX}}$, $C_{\mathrm{XYX}}$, $C_{\mathrm{YYY}}$ and $C_{\mathrm{CCY}}$. But some decrease such as $C_{\mathrm{CXY}}$ and $C_{\mathrm{CYY}}$. The on-axis (on the diagonal of the compliance matrix) compliances all increased but two of the three cross-compliances (off-diagonal terms) decreased. These results are counterintuitive as it was expected that the machine would stiffen (decreasing compliance) as the applied force increases. The dominant compliances, $C_{\mathrm{XXX}}$ and $C_{\mathrm{YYY}}$, which explains almost all of the readings (see Figure 4.10), increased in values but only did so by around 5 %. As depicted in Figure 4.13, for all retained compliance terms, at the highest force level such as 454, 580, and 706 N, both local and global compliance values (shown as a dashed line in the plots) closely follow each other. This is expected because the estimation criteria is to match the loaded telescopic double ball-bar length change readings and the readings corresponding to the higher forces are more sensitive to the compliance value. This confers them to a higher weight in the least square estimation.

The $C_{\mathrm{CCY}}$ compliance is always negative which is physically unexpected. Its global value was also negative. However, its contribution to the deflection readings is about one-thousandth that of the dominant compliance so quite negligible.

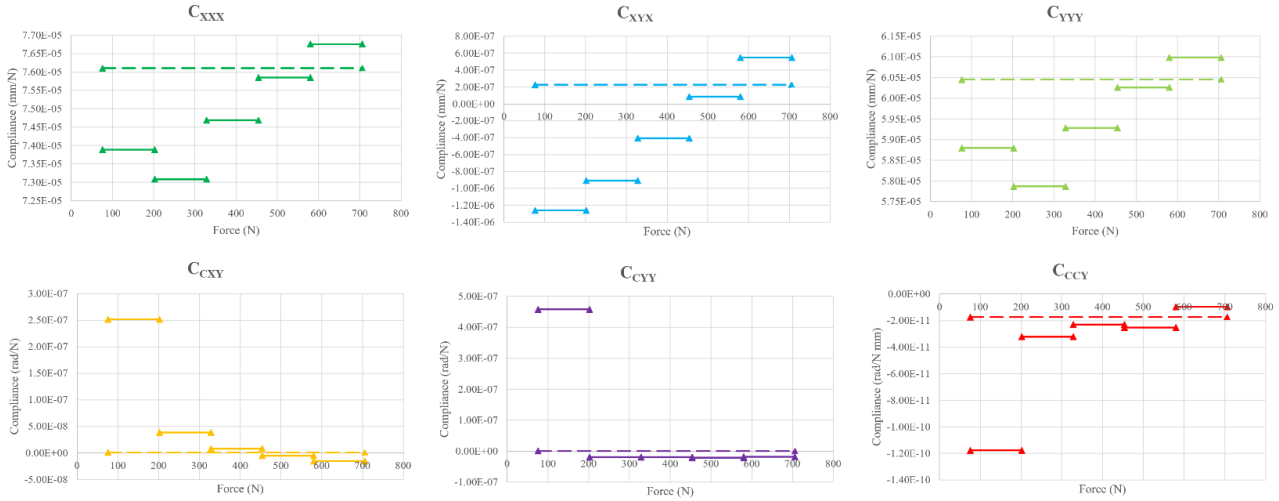


Figure 4.13. Estimated local compliances obtained using data from two consecutive force levels (a dashed horizontal line from 76 to 706 N represents the unique global compliance value for each compliance term).

The test and the model used for the estimation process do not allow to specifically consider the contribution of compliances coming from other parts of the machine. For instance, studying Figure 4.4 would suggest that compliance $C_{\mathrm{YYX}}$ will contribute to the cartesian compliance in the Y direction as would $C_{\mathrm{YYY}}$. However, the proposed test and model cannot distinguish between them and so this is the reason why the estimated compliances must be considered as equivalent compliances.

## 4.7. Uncertainty

Five repetitions of tests at 328 and 454 N were conducted on February 10th, 2021, for the purpose of evaluating the repeatability of the compliance measurement. The experimental loaded telescopic double ball-bar readings for the repeated tests are shown in Figure 4.14 They appear to have good repeatability. Based on GUM [9], a type A uncertainty is obtained by estimating the compliance values using all possible combinations of the two test repetitions. Since there are five repetitions for each test, 25 pairs of tests 1 and 2 results are available so that 25 compliance sets can be estimated each set consists of $C_{\mathrm{XXX}}$, $C_{\mathrm{XYX}}$, $C_{\mathrm{YYY}}$, $C_{\mathrm{CXY}}$, $C_{\mathrm{CYY}}$ and $C_{\mathrm{CCY}}$. The mean and standard deviation of these 25 compliance sets are calculated and shown in Table 4.8. Figure 4.15 shows the computed mean and standard deviation of those tests. These mean values differ from the compliance values previously presented which may be due to the latter having been gathered on May 2nd, 2019, about two years earlier.

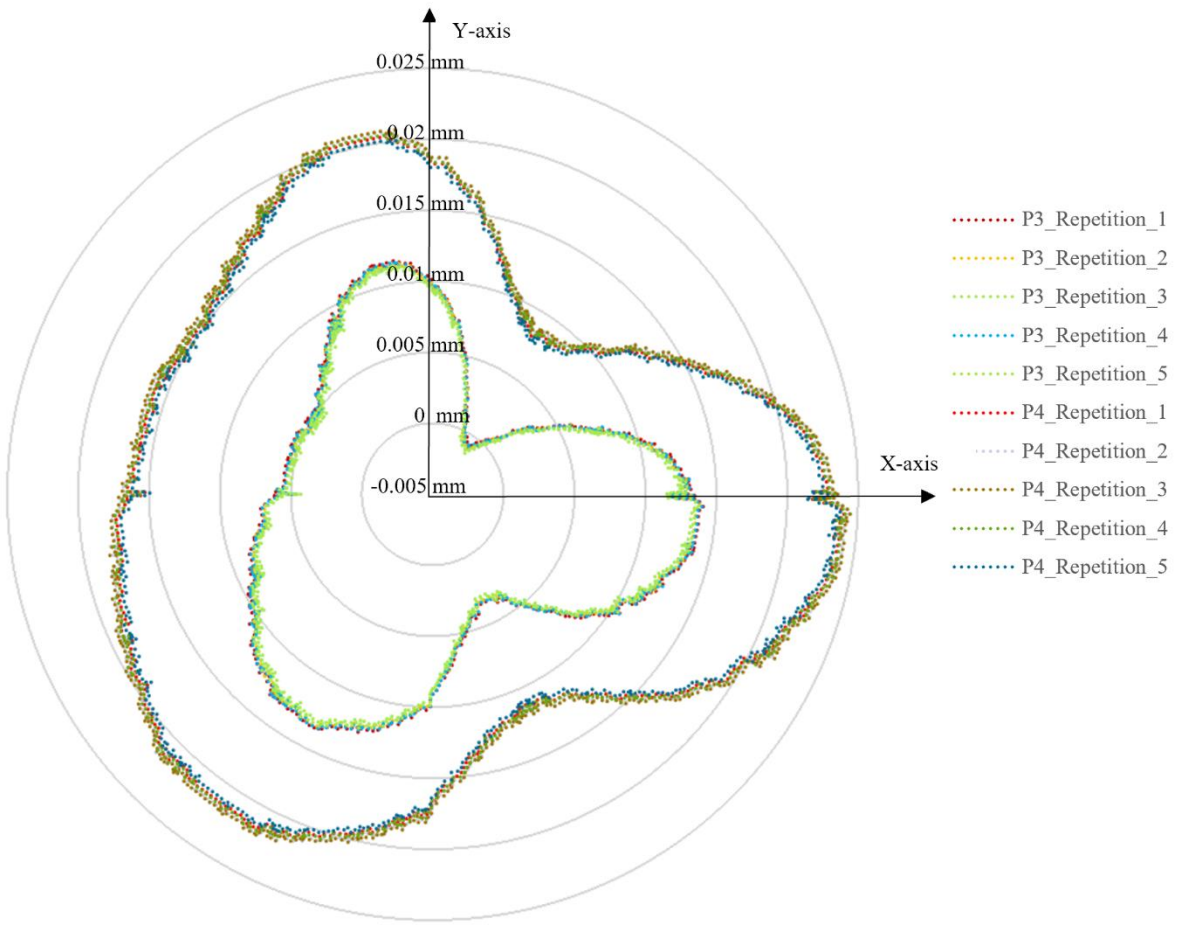


Figure 4.14. Experimental repeated LDBB readings for 328 and 454 N.

Table 4.8. Associated mean and standard deviation for each estimated compliance parameter.

| **Estimated compliance parameter** | **Mean ( $^{mm}/_{N}$ )** | **Standard deviation ( $^{mm}/_{N}$ )** |
|---|---|---|
| $C_{XXX_{est}}$ | 5.82E-05 | 2.16E-07 |
| $C_{XYX_{est}}$ | -1.69E-06 | 1.64E-08 |
| $C_{YYY_{est}}$ | 6.02E-05 | 1.88E-07 |
| $C_{CXY_{est}}$ | 4.02E-07 | 1.12E-09 |
| $C_{CYY_{est}}$ | -5.64E-08 | 7.30E-10 |
| $C_{CCY_{est}}$ | -7.66E-11 | 9.98E-13 |

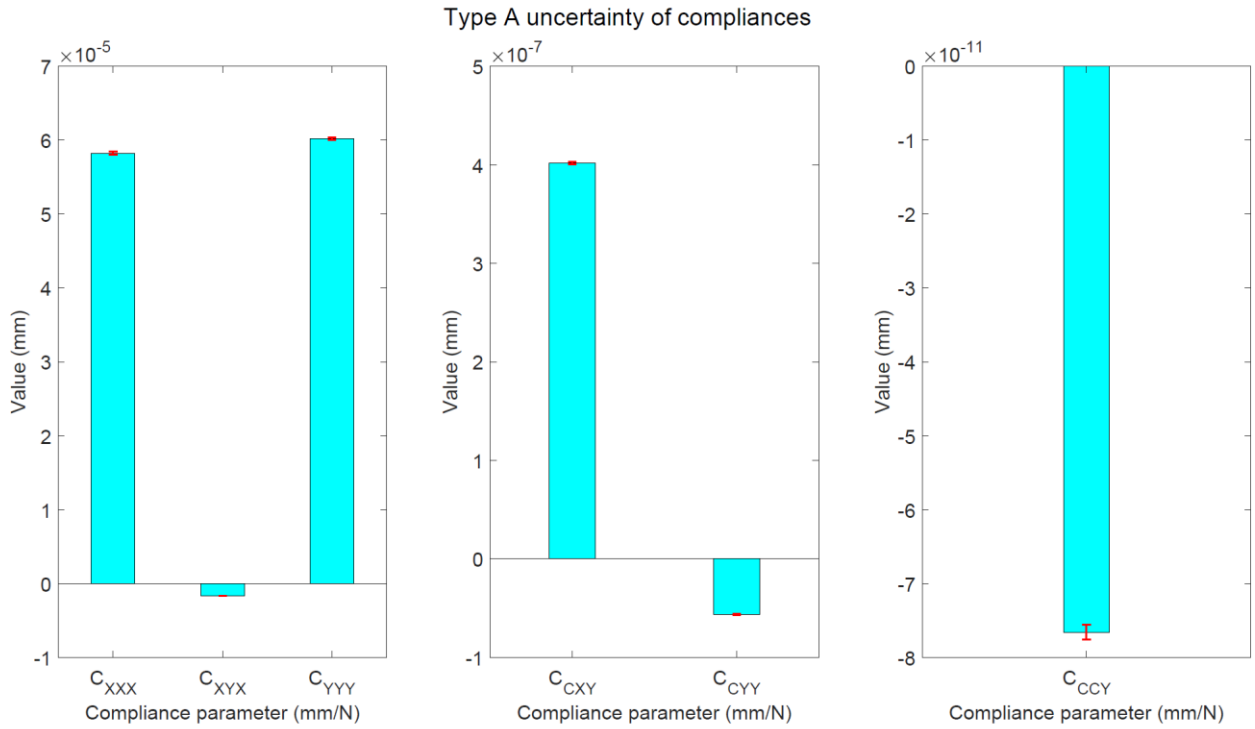


Figure 4.15. Type A uncertainty of global compliance parameters ($C_{\mathrm{XXX}}$, $C_{\mathrm{XYX}}$, $C_{\mathrm{YYY}}$, $C_{\mathrm{CXY}}$, $C_{\mathrm{CYY}}$ and $C_{\mathrm{CCY}}$).

## 4.8. Conclusion

A loaded telescopic double ball-bar is used to perform a circular 2D XY test on a machine tool from which machine equivalent joint compliances are estimated. A matrix formulation of the kinematic and compliance model of the serial mechanism is used to generate a numerical Jacobian of the change in the loaded double ball bar (LDBB) length as a function of the machine joint compliances and the applied forces. Simulations and close inspection of the numerical Jacobian matrix suggest the presence of significant confounding between compliances of the *X*- and *Y*-axis. This is partly due to the nature of the test which does not allow, for example, to differentiate between the effect of on-axis compliance at the X-axis, $C_{\mathrm{XXX}}$, and lateral compliance at the Y-axis, $C_{\mathrm{XXY}}$. A similar confounding occurs between the on-axis compliance of the Y-axis $C_{\mathrm{YYY}}$ and the lateral compliance of the X-axis $C_{\mathrm{YYX}}$. The loaded telescopic double ball-bar test was conducted at seven force levels of 36, 112, 238, 364, 490, 616, and 742 N. When using all available data, the dominant estimated global compliance

terms were $C_{\mathrm{XXX}}$ and $C_{\mathrm{YYY}}$ at 7.61E-05 and 6.05E-05 mm/N. These dominant compliances gradually increase with the load by approximately 5% over the tested load range which was unexpected. $C_{\mathrm{XYX}}$ also increased Others decreased such as $C_{\mathrm{CXY}}$ and $C_{\mathrm{CYY}}$. The compliance term $C_{\mathrm{CCY}}$ results in a four-lobed trace, as demonstrated by simulations, which has not been associated with unloaded ball bar circular tests. Its estimated value is always negative which is physically unexpected. However, its contribution to the deflection is estimated at one-thousandth that of the main compliance term and about one-third of the resolution of the LDBB position readout so its value is too small to be relied upon for the tested machine.

This indirect method of measuring the volumetric effect of many contributors are attractive by their simplicity and automation potential, especially for use as a regular checkup of a machine in an industrial setting. It also allows, given sufficiently rich tests to be determined, to separate the contribution compliance to guide repairs. The same model could then also be used to predict deflection under different conditions such as when machining. Nevertheless, the direct methods are often measuring individual compliance and the simplicity of the data does not allow to distinguish between compliance contributors within the machine.

## 4.9. Acknowledgements

This research was supported by the Natural Sciences and Engineering Research Council of Canada NSERC Canadian Network for Research and Innovation in Machining Technology–Phase 2: CANRIMT2 Grant number NSERC NETGP 479639 - 15 and by NSERC Discovery Grant number RGPIN-2016-06418. Researcher T. Laspas is acknowledged for experimental data. This Swedish part of the presented work was funded by the Centre for Design and Management of Manufacturing Systems DMMS at KTH and VINNOVA through the Eureka SMART COMACH project Grant Agreement ID: S0120).

## 4.10. Reference


1. Archenti, A. and M. Nicolescu, *Accuracy analysis of machine tools using Elastically Linked Systems.* CIRP Annals, 2013. 62(1): p. 503-506.

2. Archenti, A., *Prediction of machined part accuracy from machining system capability.* CIRP Annals, 2014. 63(1): p. 505-508.

3. Archenti, A. and M. Nicolescu, *A top-down equivalent stiffness approach for prediction of deviation sources in machine tool joints.* CIRP Annals, 2017. 66(1): p. 487-490.

4. Denkena, B. and H. Boujnah, *Feeling machines for online detection and compensation of tool deflection in milling.* CIRP Annals, 2018. 67(1): p. 423-426.

5. Matsubara, A., T. Yamazaki, and S. Ikenaga, *Non-contact measurement of spindle stiffness by using magnetic loading device.* International Journal of Machine Tools and Manufacture, 2013. 71: p. 20-25.

6. Atsushi Matsubara, T.F., Iwao Yamaji, and Soichi Ibaraki, *MEASUREMENT OF SPINDLE STIFFNESS FOR THE MONITORING SYSTEM OF CUTTING.* Proceedings of 2008 ISFA, 2008: p. 1-4.

7. Rahmani, M. and F. Bleicher, *Experimental and Analytical Investigations on Normal and Angular Stiffness of Linear Guides in Manufacturing Systems.* Procedia CIRP, 2016. 41: p. 795-800.

8. Chang, Y., et al., *Effect of joint interfacial contact stiffness on structural dynamics of ultra-precision machine tool.* International Journal of Machine Tools and Manufacture, 2020. 158.

9. *Joint Committee for Guides in Metrology. Evaluation of measurement data: Guide to the expression of uncertainty in measurement. International Bureau of Weightsand Measures; 2008.*

10. H Asada and JJE Slotine, *Robot analysis and control*. 1986, New York: Wiley.

# CHAPTER 5 ARTICLE 2 MATHEMATICAL SEPARATION OF ELASTO-GEOMETRIC ERROR PARAMETERS FROM LOADED CIRCULAR TESTS ON A MACHINE TOOL

Babak Beglarzadeh [a], J.R.R. Mayer [a], Andreas Archenti [b]

[a] Department of Mechanical Engineering, Polytechnique Montreal, Montreal, QC, H3T 1J4, Canada

[b] Department of Production Engineering, KTH Royal Institute of Technology, Brinellvägen 68, Stockholm SE-10044, Sweden

* Submitted to International Journal of Machine Tools and Manufacture on 19 February 2022

## 5.1. Abstract

A loaded double ball bar applies a radial force between the work table and the tool holder of a machine tool while measuring the radial deviations during a two-axis circular path on a machine tool. The machine compliance and geometric errors, as well as the test setup eccentricity, simultaneously contribute to the readings. An elasto-geometric model uses the principle of superposition to separate the effects of joint compliance and geometric errors. The model parameters are estimated from tests at different force levels, by distinguishing between errors that change with the applied force (compliance effect) from those that do not (geometric effects). At lower forces, the geometric errors are dominant whilst at higher forces compliance-induced errors dominate. When using all data to build a single geometry and compliance set of parameters the maximum effect of compliance reaches 0.046 mm, which is three times as much as the geometric effects. By feeding the elasto-geometric model with pairs of adjacent force data the evolution of estimated equivalent compliance parameters and geometric errors with changes in the applied force are observed. Although theoretically unexpected, the estimated geometry also changes across the force range. The change in estimated geometry predicts radial effect changes of at most 0.0085 mm, which is nearly 50% of the global geometric effect. As the force increases the majority of equivalent compliance terms increase such as the dominant equivalent compliances $C_{\mathrm{XXX}}$ and $C_{\mathrm{YYY}}$ as well as the less significant compliances $C_{\mathrm{XYX}}$ and $C_{\mathrm{CCY}}$. As for $C_{\mathrm{CXY}}$ and $C_{\mathrm{CYY}}$ no clear trend was observed. Given this observed dependence of the compliance on the force level, the compliance was further modeled as a linear function of the applied force. The root mean square error (RMSE) value for predicting the radial readings for all force levels for the constant and linearly variable compliance models are 0.0011 and 0.0009 mm, respectively, representing an 18% improvement for the linear compliance model. Both the constant and linearly

variable compliance models exhibit over 91 % fit to the experimental data with just over 1 % improvement for the linear compliance model.

**Keywords:** Elasto-geometric model, joint compliance, geometric error, machine tool, numerical simulation.

## 5.2. Introduction

Compliance in a machine tool results in changes in the location of its tool with respect to the workpiece in the presence of cutting forces and inertial and gravitational loads. A model for machine tool equivalent joint compliance is introduced in [1]. Indirect estimation of joint compliance is carried out via the loaded circular test. The relationship between joint and volumetric compliance is established. It is shown that on-axis compliances including $C_{\mathrm{XXX}}$ and $C_{\mathrm{YYY}}$ were dominant and their values slightly increased with the applied force. In this model, the effect of geometric errors was removed by subtracting the lowest force data assuming it only contained the effect of geometric errors.

The tooltip stiffness chain was examined experimentally and with both analytical and finite element models [2]. The cutting force and the tool deflection were measured with a dynamometer and inductive proximity sensors, respectively. The tool deflection was found to contribute as much as the rest of the system. Tests were conducted one direction at a time with a single axis being moved very slowly to gradually increase the deflection. Results were represented that the stiffness of shorter and thicker tools, as well as slender and flexible tools, were about 5-7 and 15 times less than that of the machine and tool holder system, respectively.

The equivalent stiffness method models the joint deviation contribution to the total volumetric deviation under load [3] from measurements of the force versus deviation functions at the interface between the tool and workpiece. The translational compliances at the joints are modeled by a number of suitably oriented linear springs.

Static stiffness modeling of the machining space is introduced in [4]. The parametric model includes the six-directional static stiffness obtained by the combination of both load and deformation transfer matrices. The loading and deformation of each part of the machine are analyzed separately. To identify the static stiffness, an experimental setup is used including a loading device (hydraulic cylinder) to apply force in the X-, Y- and Z-direction and a displacement sensor to measure the

deflection in the same direction. The error between the introduced model and measured stiffness was 7.6%.

The total stiffness of the machine is modeled using simple springs located at the bearing supports between the carriages and guideways [5]. Multi-body system theory is used to explain the topological structure of the machine. The deflection model represents the connection between the deformation of the components and the relative deformation of the tool and workpiece. To determine the stiffness value, each component was modeled as a spring with different degrees of freedom to deliver the resultant displacement in the direction of the force. The experimental data is gathered by applying a force to the machine spindle in either the X-, Y- or Z-direction and measuring the resulting deflection using an Eddy current proximity sensor. The difference between the estimated and given stiffness values at the tooltip was 8.8%, 9.6%, and 8.4% in the X-, Y- and Z-direction respectively.

To analyze the structural characteristics of an ultra-precision four-axis machine, the joint stiffness of both hydrostatic guideways of linear axes and hydrostatic bearings of the rotary C-axis were studied using a virtual prototype and experimental data [6]. The compliance of the individual axes and the stiffness of the overall machine loop were experimentally determined using a load cell and displacements measured by a laser interferometer. The virtual prototype was modeled in ANSYS software using solid elements as well as identifiable stiffness matrices for the four joints, which were identified to match the experimental joint compliances. The designed, predicted, and measured stiffness of the X- and Y-axis were 5.71, 4.68, and 4.98 (N/μm), and 9.86, 12.70, and 13.24 (N/μm), respectively. The predicted loop stiffness of the virtual prototype machine in the X-, Y- and Z-axis directions were 94%, 96%, and 93% of those experimentally measured.

In [7] the direction dependency of the tool to workpiece compliance of a machine tool was examined. A piezoelectric actuator excites the tool while the force and displacement are measured by a three-axis force sensor and three-axis accelerometer signals, respectively. The compliance in the X and Y (horizontal) directions was larger than that in the Z (vertical) direction. The highest compliance value in the X direction was two times larger than those in the Y and Z directions.

A device named Stiffness Workspace System (SWS) was introduced in [8]. It applies a force with a controlled value and direction and measures the resultant translational and rotational displacement using twelve inductive sensors. The machine is stationary. It was concluded that the stiffness varies both with the applied force direction and the location in the workspace.

An elastically Linked system (ELS) was introduced and the physical implementation was designed as a Loaded Double Ball Bar (LDBB) [9]. The LDBB measures the radial volumetric displacement during a circular test trajectory [10] while applying a constant radial force between the balls at the tool holder and workpiece table. The measurements provide the volumetric compliance i.e., the compliance in the working volume. It allows to test the machine in motion and combine the movement of two mechanical axes at various feed rates thus approaching more realistic conditions of use. A low force test is used as a reference and those readings are subtracted from data at higher force levels to remove contamination from no-load effects. Using data from an LDBB test, the accuracy of a machined part was predicted from the analysis of machining system capability [11]. In this approach, the volumetric deviations measured by an LDBB circular test are used to estimate a multi-body compliance model that can predict compliance for an arbitrary tool path. An FE model determines the tool and workpiece contributions to the total deviation. This method predicted the machined workpiece geometry with about 17% error.

The unloaded telescopic ball bar was invented to measure the two- or three-dimensional accuracy of machine tools, as a fast and accurate method [12]. In [13] the characteristic patterns of ball bar traces for 2D circular tests in the XY, YZ, and XZ planes of a three linear axis machine tool due to a variety of machine error sources such as out-of-squareness and out-of-straightness were presented.

An elasto-geometrical calibration method for geometric errors and compliance parameters of a six-DOF serial robot was introduced [14]. The load was applied using weights at the end effector and the effect on the positioning was measured using a laser tracker. The torsional compliances, self-gravity, and weight center of gravity were estimated. The geometric errors included such as joint-dependent and joint-independent errors including link, link offset and link twist errors.

When conducting a loaded test that involves a significant motion of one or more axes, geometric errors may also, together with compliance, produce instrument readings. This is the case when conducting a two-linear axis circular test using a loaded double ball bar. This paper proposes to simultaneously estimate joint compliances and geometric error using an elasto-geometric model and the associated mathematical parameter separation in order to attribute the observations to geometric errors and joint compliances, which should facilitate machine monitoring and fault diagnostics. It also provides a means to analyze the relative contribution of geometric errors and compliance at different load levels.

## 5.3.Machine geometric and volumetric model

A geometrically perfect, thermally insensitive, and rigid machine tool locates its tool and workpiece to the desired relative location. However, manufacturing and assembly errors, wear and tear, collisions, thermal expansion, and the presence of forces and compliance are a few factors that cause the tool to deviate in location relative to the workpiece. A machine tool kinematics can be modeled using a series of links and joints [15]. Machine deviations can be quantified as small errors in translations and rotations occurring at the attachment of each link between axis joints as axis alignment errors (or inter-axis errors) and each joint frame as error motion (intra-axis errors). These errors then propagate through the branches to the workpiece and tool. The difference between the actual and the nominal positions of the tool relative to the workpiece defines the volumetric error. A schematic of the kinematic model of the tested machine is illustrated in Figure 5.1. As shown in Figure 5.1 the LDBB circular test only involves the X- and Y-axis and since both are in the tool branch, the kinematic model of the deviated position of the tool with respect to the foundation frame can be written as

$$ {}^{\{F\},F}_{\quad t'}P = {}^{F}_{Y_0}T\ {}^{Y_0}_{Y_0'}T\ {}^{Y_0'}_{Y}T\ {}^{Y}_{Y'}T\ {}^{Y'}_{X_0}T\ {}^{X_0}_{X_0'}T\ {}^{X_0'}_{X}T\ {}^{X}_{X'}T\ {}^{X'}_{t}T\ {}^{t}_{t'}T\ [0 \quad 0 \quad 0 \quad 1]^T \tag{5.1} $$

in which ${}^{i}_{j}T$ is the homogeneous transformation matrix (HTM) from frame *i* to frame *j*. ${}^{F}_{Y_0}T$ is the nominal location of the Y-axis and it is identity as the foundation frame and the Y-axis carriage frame at y=0 cannot be distinguished from each other, since the Y-axis is the primary reference then ${}^{Y_0}_{Y_0'}T$ is also identity, ${}^{Y_0'}_{Y}T$ is the nominal motion of the Y-axis, ${}^{Y}_{Y'}T$ is error motion of the Y-axis, ${}^{Y'}_{X_0}T$ is identity as the X-axis is nominally aligned with the *i*-axis of frame Y' and the X-axis location error, here an out-of-squareness error, will be modeled as a linear straightness error, then ${}^{X_0}_{X_0'}T$ is identity, ${}^{X_0'}_{X}T$ is the nominal motion of the X-axis, ${}^{X}_{X'}T$ is the error motion of the X-axis and ${}^{X'}_{t}T$ is identity as the nominal tool ball is assumed to be nominally at the moving carriage frame origin. ${}^{t}_{t'}T$ is the setup error on the tool ball. The LDBB test is conducted within a single XY plane and since the LDBB test

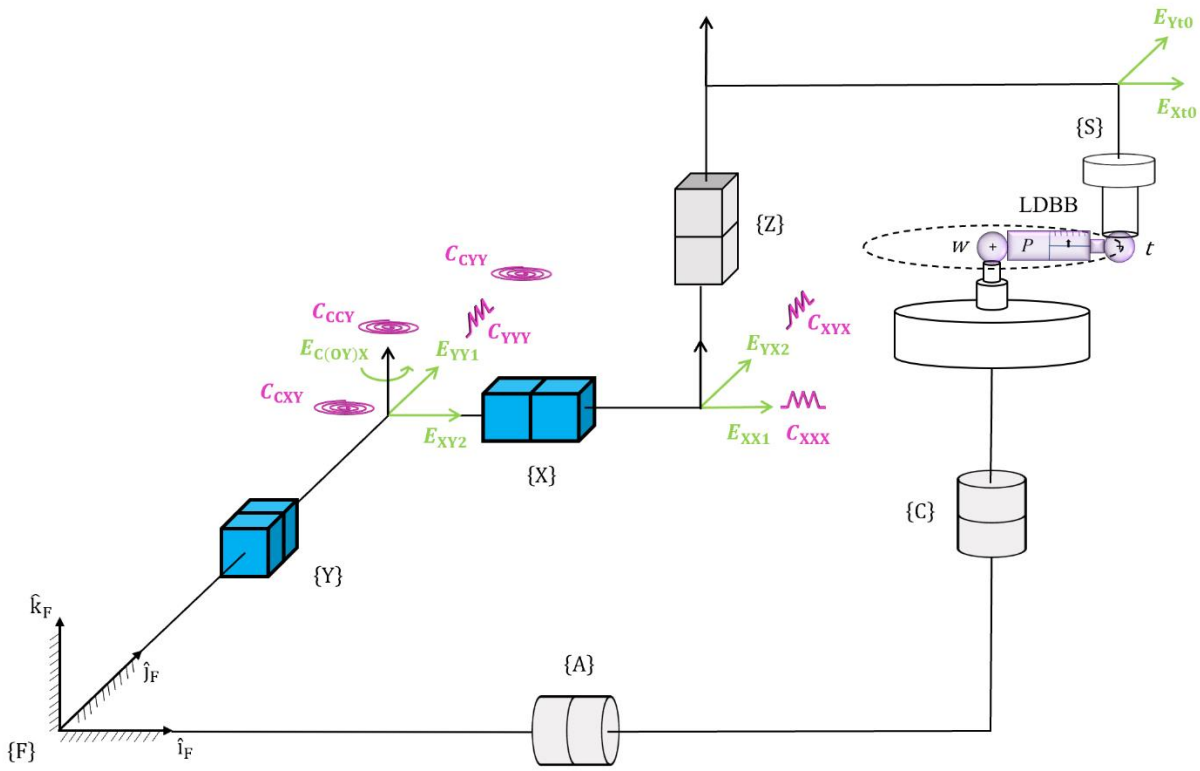


Figure 5.1. Schematic of the nominal model for the LDBB test and its circular path through the XY plane along with the machine with the topology of wCAFYXZSt where S stands for the spindle axis. Only the X- and Y-axis, shown in blue, are active during the LDBB circular test. Compliance and geometric parameters are shown in magenta and green color, respectively.

does not provide readings out of the XY plane, only the error terms that can affect the ball bar readings are retained. The matrices of the model are as follows:

$$ {}^{F}_{Y_0}T = \begin{pmatrix} 1 & 0 & 0 & 0 \\ 0 & 1 & 0 & 0 \\ 0 & 0 & 1 & 0 \\ 0 & 0 & 0 & 1 \end{pmatrix} \tag{5.2} $$

$$ {}^{Y_0}_{Y_0'}T = \begin{pmatrix} 1 & 0 & 0 & 0 \\ 0 & 1 & 0 & 0 \\ 0 & 0 & 1 & 0 \\ 0 & 0 & 0 & 1 \end{pmatrix} \tag{5.3} $$

$$ {}^{Y'_0}_{Y}T = \begin{pmatrix} 1 & 0 & 0 & 0 \\ 0 & 1 & 0 & y \\ 0 & 0 & 1 & 0 \\ 0 & 0 & 0 & 1 \end{pmatrix} \tag{5.4} $$

$$ {}^{Y}_{Y'}T = \begin{pmatrix} & & E_{XY} \\ & \left[R(\hat{k}_Y, E_{C(OY)X})\right]_{3\times3} & E_{YY} \\ & & 0 \\ & 0_{1\times3} & 1 \end{pmatrix} \tag{5.5} $$

$$ {}^{Y'}_{X_0}T = \begin{pmatrix} 1 & 0 & 0 & 0 \\ 0 & 1 & 0 & 0 \\ 0 & 0 & 1 & 0 \\ 0 & 0 & 0 & 1 \end{pmatrix} \tag{5.6} $$

$$ {}^{X_0}_{X'_0}T = \begin{pmatrix} 1 & 0 & 0 & 0 \\ 0 & 1 & 0 & 0 \\ 0 & 0 & 1 & 0 \\ 0 & 0 & 0 & 1 \end{pmatrix} \tag{5.7} $$

$$ {}^{X'_0}_{X}T = \begin{pmatrix} 1 & 0 & 0 & x \\ 0 & 1 & 0 & 0 \\ 0 & 0 & 1 & 0 \\ 0 & 0 & 0 & 1 \end{pmatrix} \tag{5.8} $$

$$ {}^{X}_{X'}T = \begin{pmatrix} 1 & 0 & 0 & E_{XX} \\ 0 & 1 & 0 & E_{YX} \\ 0 & 0 & 1 & 0 \\ 0 & 0 & 0 & 1 \end{pmatrix} \tag{5.9} $$

$$ {}^{X'}_{t}T = \begin{pmatrix} 1 & 0 & 0 & 0 \\ 0 & 1 & 0 & 0 \\ 0 & 0 & 1 & 0 \\ 0 & 0 & 0 & 1 \end{pmatrix} \tag{5.10} $$

$$ {}^{t}_{t'}T = \begin{pmatrix} 1 & 0 & 0 & E_{Xt} \\ 0 & 1 & 0 & E_{Yt} \\ 0 & 0 & 1 & 0 \\ 0 & 0 & 0 & 1 \end{pmatrix} \tag{5.11} $$

where for instance $R(\hat{k}_Y, E_{C(OY)X})$ depicts a rotation by an angle $E_{C(OY)X}$ around the Z-axis of the Y-axis reference frame and $E_{XY}$ and $E_{YY}$ are linear positioning error of the Y-axis and straightness error motion of the X-axis in the y-direction. Additionally, $E_{XX}$, $E_{YX}$, $E_{Xt}$ and $E_{Yt}$ are linear positioning error of the X-axis, straightness error motion of the X-axis in the y-direction, tool offset in the x-direction, and tool offset in the y-direction, respectively.

In the workpiece branch, the deviation of the actual position of the workpiece ball with respect to the foundation frame is:

$$ {}^{\{F\},F}_{w'}P = {}^{F}_{w}T\,{}^{w}_{w'}T\,[0 \quad 0 \quad 0 \quad 1]^{T} \tag{5.12} $$

However, since there is no physical means of distinguishing between the foundation frame and the actual workpiece ball position all HTMs in Eq.(5.12) are replaced by the identity matrix as only one setup is used and the workpiece ball is used as the foundation frame origin.

The LDBB readings, $\rho$, are computed by the subtraction of the nominal trajectory radius, R, from the actual cartesian distance between the actual positions of the tool and workpiece balls as follows:

$$ \rho = R' - R \tag{5.13} $$

where the actual cartesian distance is:

$$ R' = \left\| {}^{\{F\},F}_{t}P - {}^{\{F\},F}_{w}P \right\| \tag{5.14} $$

While the above model is theoretically exact for any size of deviations, a simplified linearized model can be produced assuming that deviations are small. This model can easily be solved to estimate the causal deviations indirectly from measurements of the volumetric errors. A geometric Jacobian matrix, $J$, propagates the causal geometric errors, $E_G$, which include the geometric errors occurring at the joints and the setup errors, to the volumetric cartesian errors, $E_V$, as follows [16]

$$ E_V = J\,E_G \tag{5.15} $$

where

$$ J = \begin{bmatrix} x & 0 & y^2 & 0 & 0 & 1 & 0 \\ 0 & x^2 & 0 & y & x & 0 & 1 \\ 0 & 0 & 0 & 0 & 1 & 0 & 0 \end{bmatrix} \tag{5.16} $$

where $x$ and y are the joint coordinates for axis X and Y respectively. Each column of the Jacobian matrix are related to the following geometric errors and setup errors composing $E_G = [\,E_{XX1}, E_{YX2}, E_{XY2}, E_{YY1}, E_{C(0Y)X}, E_{Xt0}, E_{Yt0}]^{T}$.

Eq.(5.15) can be contextualized to the telescopic loaded double ball bar reading by projecting the translational volumetric error vector along the sensitive direction of the ball bar at position $i$

$$ \rho_{G,i} = J_{G,i}\,E_G \tag{5.17} $$

where

$$J_{\mathrm{G},i} = [\cos\theta_i \;\; \sin\theta_i \;\; 0]\, J \tag{5.18}$$

with $\theta_i$ being the angle that the ball-bar sensitive direction makes with the X-axis.

Multiple measurements around the circular trajectory are concatenated vertically to yield a single linear system relating all ball bar readings to the causal geometric errors occurring at the joint and the setup errors of the balls of the ball-bar

$$\rho_{\mathrm{G}} = J_{\mathrm{G}}\, E_{\mathrm{G}} \tag{5.19}$$

## 5.4. Compliance model

The compliance model calculates the deflection occurring at the tool relative to the workpiece due to a wrench applied between the tool and the workpiece in the presence of compliance (inverse of stiffness) at the joints. It requires calculating the reaction wrench at the joints, the resulting deflection at the joint, and propagating these deflections down the kinematic chains to the tool in the tool branch and the workpiece in the workpiece branch using the geometric Jacobian. For each measurement $i$=1,m of the LDBB a wrench $W_i$ is applied resulting in a change in the LDBB length $\rho_{C,i}$ as follows:

$$\rho_{C,i} = \hat{B}^{\mathrm{T}}{}_i \; J_i \; C_{\mathrm{joint}} \; J^{\mathrm{T}}{}_i \; W_i \qquad i = 1, \mathrm{m} \tag{5.20}$$

where,

$$\hat{B}_i = \begin{bmatrix} \cos\theta_i \\ \sin\theta_i \\ 0 \end{bmatrix} \qquad i = 1, \mathrm{m} \tag{5.21}$$

is the unit vector of the sensitive direction of the LDBB and

$$J_i = \begin{bmatrix} 1 & 0 & -t_{\mathrm{y}} & 1 & 0 & -t_{\mathrm{y}} \\ 0 & 1 & t_{\mathrm{x}} & 0 & 1 & x_i + t_{\mathrm{x}} \\ 0 & 0 & 1 & 0 & 0 & 1 \end{bmatrix} \qquad i = 1, \mathrm{m} \tag{5.22}$$

where $t_{\mathrm{x}}$ and $t_{\mathrm{y}}$ are coordinates of the tool in the last tool branch frame, i.e. the X-axis frame and

$$W_i = \begin{bmatrix} F_{\mathrm{X}_i} \\ F_{\mathrm{Y}_i} \\ \tau_{\mathrm{Z}_i} \end{bmatrix} \qquad i = 1, \mathrm{m} \tag{5.23}$$

is the general wrench, for the 2D case, consisting of two forces in the X- and Y-direction and torque around the Z-axis. The complete two axes compliance matrix is

$$C_{\text{joint}_{6\times6}} = \begin{bmatrix} C_{\text{XXX}} & C_{\text{XYX}} & C_{\text{XCX}} & 0 & 0 & 0 \\ C_{\text{YXX}} & C_{\text{YYX}} & C_{\text{YCX}} & 0 & 0 & 0 \\ C_{\text{CXX}} & C_{\text{CYX}} & C_{\text{CCX}} & 0 & 0 & 0 \\ 0 & 0 & 0 & C_{\text{XXY}} & C_{\text{XYY}} & C_{\text{XCY}} \\ 0 & 0 & 0 & C_{\text{YXY}} & C_{\text{YYY}} & C_{\text{YCY}} \\ 0 & 0 & 0 & C_{\text{CXY}} & C_{\text{CYY}} & C_{\text{CCY}} \end{bmatrix}. \tag{5.24}$$

where for example $C_{\text{CXY}}$ represents compliance causing a rotation around z (represented by C) due to a force in x, both occurring at joint Y. Each compliance term has three subscripts. The first subscript is the translation or rotation direction, the second subscript is the applied force direction, and the third subscript is the relevant joint or axis, respectively.

Since the LDBB test is conducted within a single XY plane and it does not provide readings out of the XY plane, only the compliance error terms of the X- and Y-axis that can affect the ball bar readings are considered in the model. However, there could be a contribution of compliances originating from other components and non-modeled, but stationary, axes of the machine such as the Z-, A-, and C-axis. Hence, the estimated compliances will be considered as equivalent compliances.

### 5.4.1. Linearized wrench Jacobian

The authors did not find a closed-form solution for the compliance matrix from experimental measurements of the applied wrench and resulting LDBB length changes. Instead, Eq.(5.20) was used to generate a wrench Jacobian $J_{\text{W}}$ through numerical derivatives that multiplies the 18 compliances to produce the LDBB length change as follows:

$$\rho_{\text{C}\ \text{m}\times1} = J_{\text{W}_{\text{m}\times18}} C_{18\times1} \tag{5.25}$$

where the $J_{\text{W}}$ is

$$J_{\text{W}_{i,j}} = \frac{\partial \rho_i}{\partial \text{C}_j} \qquad i = 1, \text{m and } j = 1, 18 \tag{5.26}$$

## 5.5. Elasto-geometric model

The elasto-geometric model uses the principle of superposition to combine the effects of geometric errors and compliance deflection on the position of the tool relative to the workpiece. Intuitively, the geometric errors will cause a certain change in the length of the loaded ball bar even if no load is applied. Then, by applying the load the compliance within the system will result in an additional change in the ball bar length. The no-load geometric effects and the load-related compliance effects

are assumed to act independently. This is also a consequence of the load applied by the LDBB not being dependent on its length as it is applied using air pressure within a cylinder. As a result, the geometric effect does not cause a change in load and so the elasto-geometric model becomes

$$\rho_{\mathrm{H}} = \rho_{\mathrm{C}} + \rho_{\mathrm{G}} \tag{5.27}$$

where $\rho_{\mathrm{G}}$, $\rho_{\mathrm{C}}$ and $\rho_{\mathrm{H}}$ are the ball-bar length change due to the geometric errors, the compliance deflection, and both (the letter H was chosen for hybrid compliance and geometric error model), respectively. Using data at a single force level is not likely to allow us to distinguish between the geometric and compliance error sources. Let us consider two force levels for the system of equations to separate parameters with an effect that is constant across force levels, i.e. geometric errors, from parameters that have an effect proportional to the applied force, i.e the compliances. For example, using two force levels and Eq.(5.25) for each level yields Eq.(5.28) and Eq.(5.29)

$$\rho_{\mathrm{C},1,i} = J_{\mathrm{F},1,i}\, C \tag{5.28}$$

$$\rho_{\mathrm{C},2,j} = J_{\mathrm{F},2,j}\, C \tag{5.29}$$

which are then substituted in the combined equation

$$\rho_{\mathrm{H},1,i} = \rho_{\mathrm{C},1,i} + \rho_{\mathrm{G},i} \tag{5.30}$$

$$\rho_{\mathrm{H},2,j} = \rho_{\mathrm{C},2,j} + \rho_{\mathrm{G},j} \tag{5.31}$$

By substituting Eq.(5.17), Eq.(5.28), and Eq.(5.29) in Eq.(5.30) and Eq.(5.31),

$$\rho_{\mathrm{H},1,i} = J_{\mathrm{F},1,i} C + J_{\mathrm{G},i}\, E_{\mathrm{G}} \tag{5.32}$$

$$\rho_{\mathrm{H},2,j} = J_{\mathrm{F},2,j} C + J_{\mathrm{G},j}\, E_{\mathrm{G}} \tag{5.33}$$

which can be written in a matrix form,

$$\begin{bmatrix} \rho_{\mathrm{H},1,i} \\ \rho_{\mathrm{H},2,j} \end{bmatrix} = \begin{bmatrix} J_{\mathrm{F}1,i} & J_{\mathrm{G},i} \\ J_{\mathrm{F}2,j} & J_{\mathrm{G},j} \end{bmatrix} \begin{bmatrix} C \\ E_{\mathrm{G}} \end{bmatrix} \tag{5.34}$$

For $i$=1, $m_1$, and $j$=1 to $m_2$, there are $m=m_1+m_2$ measurements in total so Eq.(5.34) can be re-written

$$\begin{bmatrix} \rho_{\mathrm{H},1} \\ \vdots \\ \rho_{\mathrm{H,m}} \end{bmatrix}_{m\times 1} = \begin{bmatrix} J_{\mathrm{F},1} & J_{\mathrm{G},1} \\ \vdots & \vdots \\ J_{\mathrm{F,m}} & J_{\mathrm{G,m}} \end{bmatrix}_{m\times 13} \begin{bmatrix} C \\ E_{\mathrm{G}} \end{bmatrix}_{13\times 1} \tag{5.35}$$

Eq.(5.35) can be summarized as follow:

$$\rho_{\mathrm{H}_{m\times 1}} = J_{\mathrm{H}_{m\times 13}} P_{\mathrm{H}_{13\times 1}} \tag{5.36}$$

where, $\rho_{\mathrm{H}}$ is the summation of the compliance and geometric LDBB length change readings. $J_{\mathrm{H}}$ is the elasto-geometric Jacobian which is constituted by the combination of the wrench Jacobian and geometric Jacobian. Finally, $P_{\mathrm{H}}$ is the combined parameters set which are composed of compliance and geometric parameters. To estimate the elasto-geometric parameters, Eq.(5.36) is solved using the elasto-geometric Jacobian pseudoinverse as follows:

$$P_{\mathrm{H,est}_{13\times 1}} = J^{+}{}_{\mathrm{H}_{13\times m}}\, \rho_{\mathrm{H}_{m\times 1}} \tag{5.37}$$

Figure 5.2 shows a 3D rendering of the tested 5-axis CNC machine with the topology wCAFYXZSt.

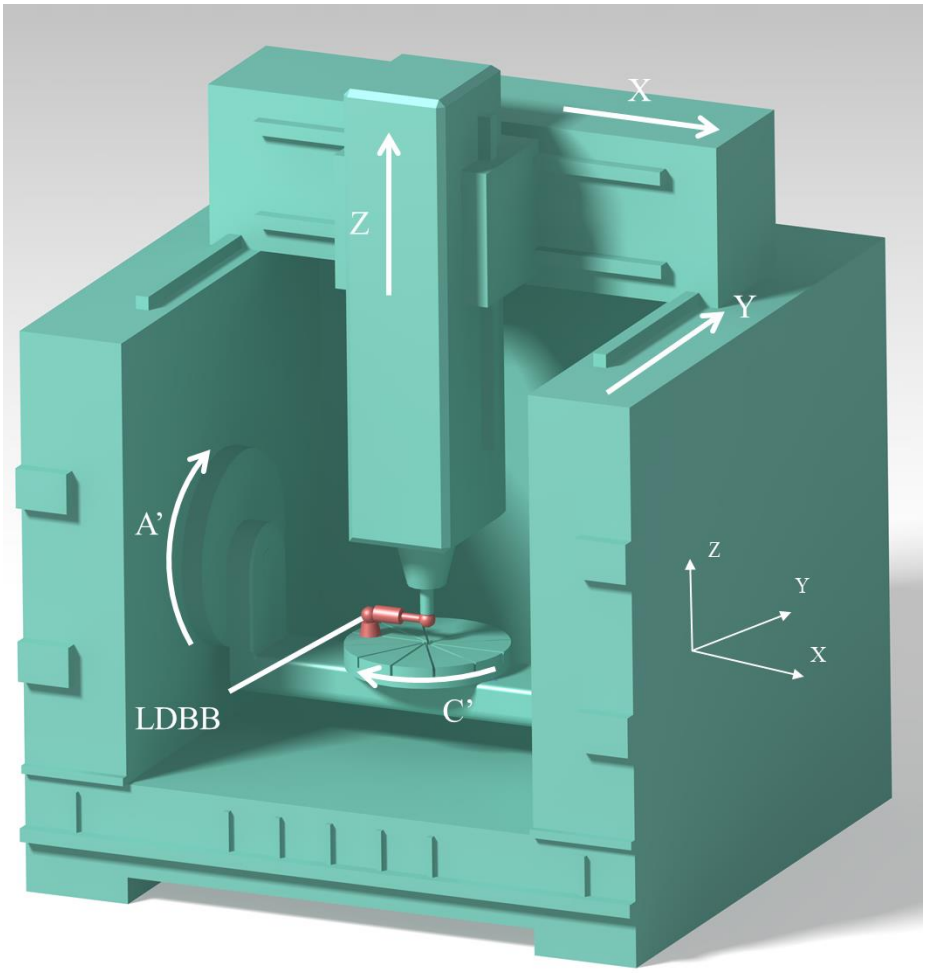


Figure 5.2. 3D rendering of the target 5-axis machine tool (wCAFYXZSt) with the LDBB mounted.

## 5.6. Simulation

Figure 5.3 shows the data flow for the simulation of the elasto-geometric model. The joint compliances are simulated at reasonable values from the literature review. The simulated LDBB

readings due to the compliance calculated with Eq.(5.20) and the simulated geometric contributions to the readings calculated with Eq.(5.13) geometric are summed up using Eq.(5.30) and Eq.(5.31) to generate the combined readings. In the estimation process, Eq.(5.37) yields the estimated combined parameters (compliance and geometric parameters) which are then compared with the simulated values. They are also used back in Eq.(5.20) and Eq.(5.13) to predict the LDBB combined readings which are compared with the initially simulated readings.

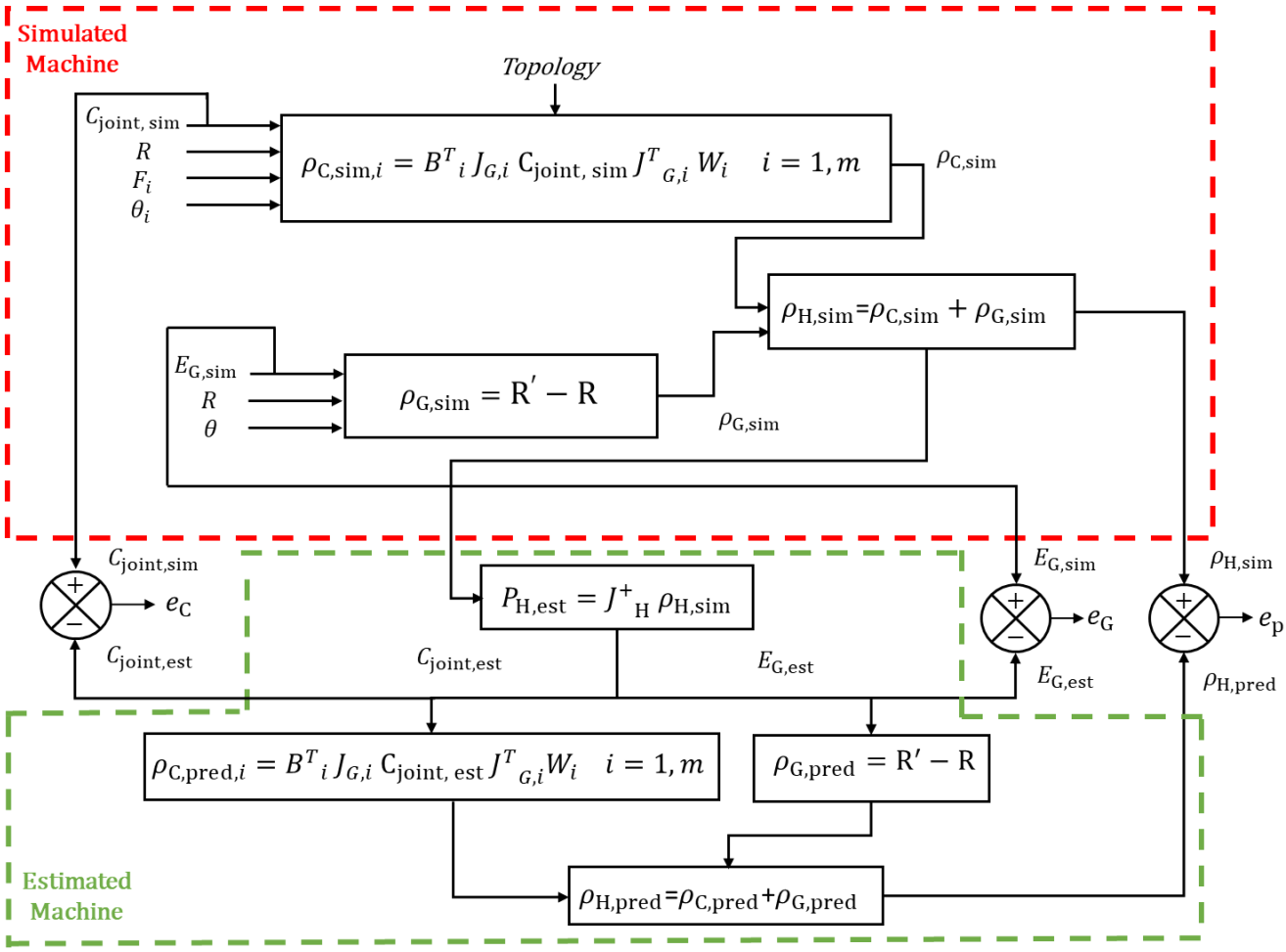


***W:*** simulated wrench at the tool
***F:*** loaded double ball bar force
***R:*** nominal trajectory radius
***R′:*** Cartesian distance
***θ:*** loaded double ball bar rotation angle
$\boldsymbol{C_{\text{joint,sim}}}$**:** simulated compliance for each axis
$\boldsymbol{C_{\text{joint,est}}}$**:** estimated compliance for each axis
$\boldsymbol{E_{\text{G,sim}}}$**:** simulated geometric parameters for each axis
$\boldsymbol{E_{\text{G,est}}}$**:** estimated geometric parameters for each axis
$\boldsymbol{\rho_{\text{G,sim}}}$**:** simulated geometric loaded double ball bar reading
$\boldsymbol{\rho_{\text{C,sim}}}$**:** simulated compliance loaded double ball bar reading

$\boldsymbol{\rho}_{\mathbf{H,sim}}$: elasto-geometric (combined) simulated loaded double ball bar reading
$\boldsymbol{\rho}_{\mathbf{H,\,pred}}$: elasto-geometric (combined) predicted loaded double ball bar reading
$\boldsymbol{J}_{\mathbf{H}}$: elasto-geometric (combined) Jacobian matrices
$\boldsymbol{\rho}_{\mathbf{C,pred}}$: predicted compliance loaded double ball bar reading
$\boldsymbol{\rho}_{\mathbf{G,pred}}$: predicted geometric loaded double ball bar reading
$\boldsymbol{e}_{\mathbf{G}}$: geometric parameters error
$\boldsymbol{e}_{\mathbf{C}}$: compliance error
$\boldsymbol{e}_{\mathbf{P}}$: loaded double ball bar reading error

Figure 5.3. Data flow for the simulation of the elasto-geometric Model.

### 5.6.1. Simulation results and discussion

Since only the X- and Y-axis of the wCAFYXZSt machine, illustrated in Figure 5.2, are engaged in the 2D circular test only compliance and geometric errors in the XY plane and rotations around the Z-axis are considered. As a result, the model may use those modeled axes to explain effects, which may in reality originate from non-modeled axes of the real machine. The following relevant geometric errors for the 2D test as shown in Figure 5.1, are simulated: $E_{\mathrm{XX1}}$, $E_{\mathrm{YX2}}$, $E_{\mathrm{XY2}}$, $E_{\mathrm{YY1}}$, $E_{\mathrm{C(0Y)X}}$, $E_{\mathrm{Xt0}}$ and $E_{\mathrm{Yt0}}$. They are described in Table 5.1.

The linearized wrench Jacobian matrix in Eq.(5.26) has 18 columns, which represent each compliance term. The condition number and rank of the wrench Jacobian matrix are 1.7e+34 and six, respectively. The rank of the matrix shows that there are only six independent columns out of 18. Twelve compliances must be removed from the estimation process. If the numerical Jacobian matrix has identical or linearly related columns, one of the compliances associated with this set is kept and the others are removed. Table 5.2 lists such compliance sets of confounded compliances. Compliances associated with null columns are also removed. The retained compliances as shown in Figure 5.1, are $C_{\mathrm{XXX}}$, $C_{\mathrm{XYX}}$, $C_{\mathrm{YYY}}$, $C_{\mathrm{CXY}}$, $C_{\mathrm{CYY}}$ and $C_{\mathrm{CCY}}$ which are in bold in Table 5.2. However, other compliances from each confounded set could have been selected. The reduced Jacobian condition number decreases to 9742 while the rank remains at six. The detailed descriptions of the kept compliance and geometric parameters are presented in Table 5.1.

Table 5.1. A detailed description of relevant compliance and geometric errors.

| **Error description** | **Symbol** |
|---|---|
| Compliance causing a translation in x for a force in x at joint X | $C_{\mathrm{XXX}}$ |
| Compliance causing a translation in x for a force in y at joint X | $C_{\mathrm{XYX}}$ |
| Compliance causing a translation in y for a force in y at joint Y | $C_{\mathrm{YYY}}$ |
| Compliance causing a rotation around z (C) for a force in x at joint Y | $C_{\mathrm{CXY}}$ |
| Compliance causing a rotation around z (C) for a force in y at joint Y | $C_{\mathrm{CYY}}$ |
| Compliance causing a rotation around z (C) for a moment of the force around z (C) at joint Y | $C_{\mathrm{CCY}}$ |
| Linear positioning error gain of the X-axis | $E_{\mathrm{XX1}}$ |
| Quadratic straightness error motion of the X-axis in the Y-direction | $E_{\mathrm{YX2}}$ |
| Quadratic straightness error motion of the Y-axis in the X-direction | $E_{\mathrm{XY2}}$ |
| Linear positioning error gain of the Y-axis | $E_{\mathrm{YY1}}$ |
| Out-of-squareness of the X-axis relative to the Y-axis | $E_{\mathrm{C(0Y)X}}$ |
| Tool offset in the X-direction | $E_{\mathrm{Xt0}}$ |
| Tool offset in the Y-direction | $E_{\mathrm{Yt0}}$ |

Compliances and geometric errors are individually simulated to detect similarities in the response of the LDBB. Parameters producing similar responses cannot be separated mathematically. Table 5.2 and Table 5.3 presents the LDBB response patterns generated by each simulated compliance and geometric term, respectively. These simulations were used to guide the variables' pruning selection.

Table 5.2. LDBB response patterns generated by each compliance term (one unit of the radial scale represents 15.0 µm).

| **List of compliances and their corresponding LDBB patterns (kept compliances are in bold)** | |
|---|---|
| $\boldsymbol{C_{XXX}}$ , $C_{XXY}$ | $C_{XCY}$ , $\boldsymbol{C_{CXY}}$ |
| 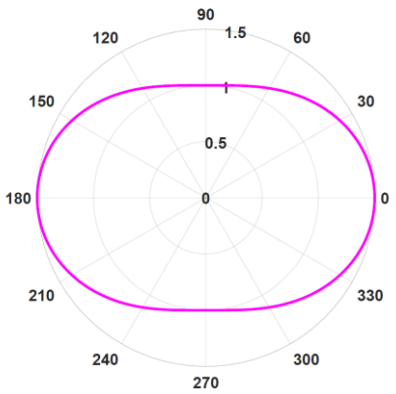 | 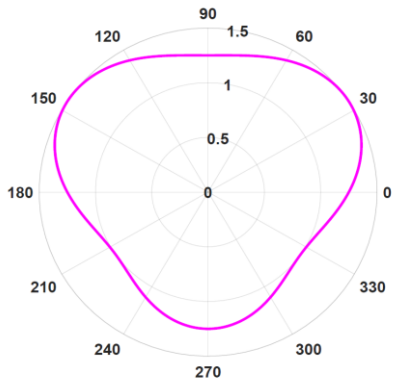 |
| $\boldsymbol{C_{XYX}}$, $C_{YXX}$, $C_{XYY}$ , $C_{YXY}$ | $C_{YCY}$, $\boldsymbol{C_{CYY}}$ |
| 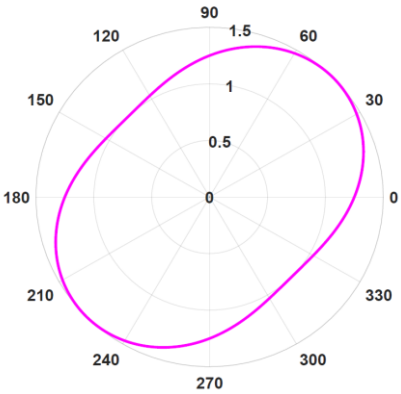 | 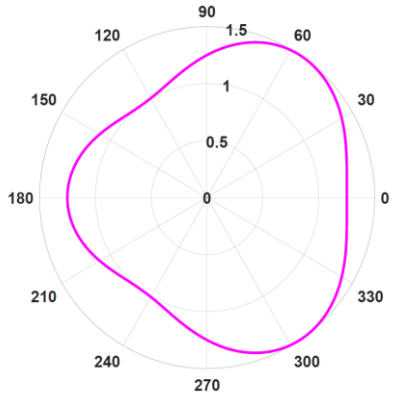 |
| $C_{YYX}$, $\boldsymbol{C_{YYY}}$ | $\boldsymbol{C_{CCY}}$ |
| 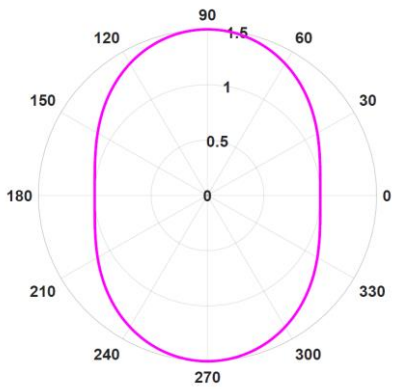 | 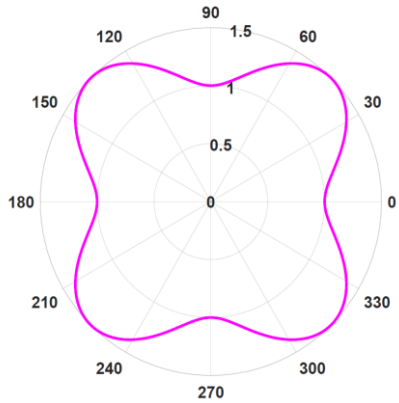 |

Table 5.3. LDBB response patterns generated by each geometric parameter (one unit of the radial scale represents 15.0 µm).

| List of geometric parameters each producing the pattern shown | | | |
|---|---|---|---|
| $E_{XX1}$ | $E_{YX2}$ | $E_{XY2}$ | $E_{YY1}$ |
| 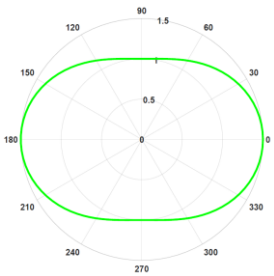 | 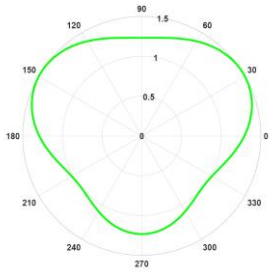 | 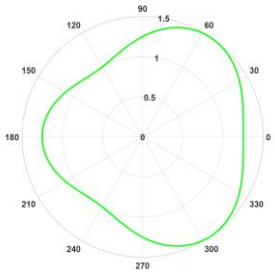 | 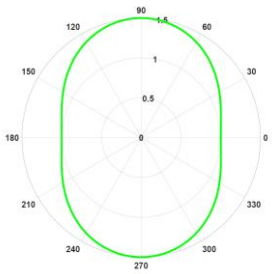 |
| $E_{C(0Y)X}$ | $E_{Xt0}$ | $E_{Yt0}$ | - |
| 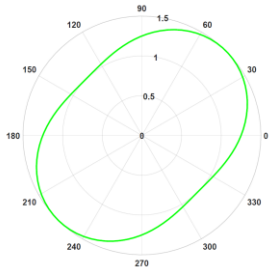 | 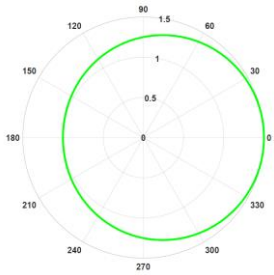 | 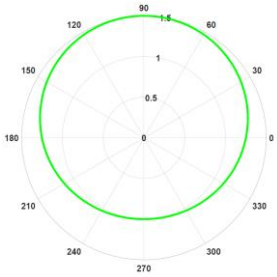 | |

Some simulations are also conducted to show that although some geometric and compliance parameters produce similar patterns the size of the compliance pattern varies with the applied force thus allowing its separation from the geometric effect. For this simulation $E_{\mathrm{XX1}}$ and $C_{\mathrm{XXX}}$ are set to 1.1200 E-04 and 1.1000 E-04, respectively, and seven force values are simulated i.e., 36,112, 238, 364, 490, 616, and 742 N. The LDBB readings are shown in Figure 5.4. At a force of 0 N, the compliance does not contribute to the LDBB readings and so only the geometric error produces the response. As shown in Figure 5.4, for non-zero forces from 36 to 742 N the readings gradually increase. Both $C_{\mathrm{XXX}}$ and $E_{\mathrm{XX1}}$ cause an ovalisation of the response along the X-axis but the size of the oval effect due to the compliance parameters changes with the applied force whereas the geometric effect, as modeled, does not.

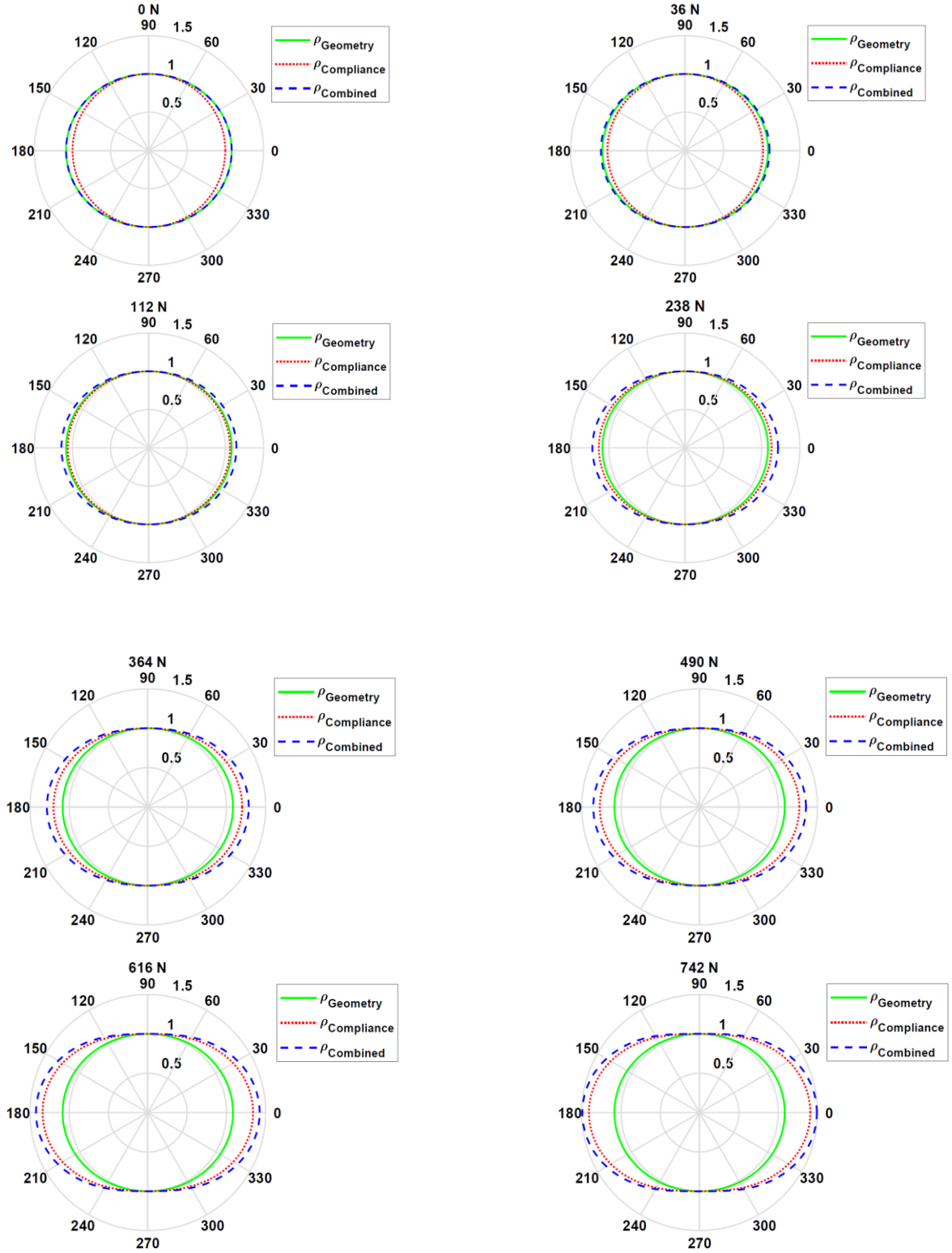


Figure 5.4. The LDBB's simulated as well as integrated compliance and geometric readings with a given value of $C_{XXX}$ and $E_{XX1}$ for seven different force levels (36,112, 238, 364, 490, 616 and 742 N).

Table 5.4. Simulated and estimated compliance values and geometric errors.

| Error | Simulated | Estimated | Difference | % Difference |
|---|---|---|---|---|
| $E_{XX1}$ | 1.1200E-04 | 1.1200E-04 | 0.0000 | 0.0000 |
| $E_{YX2}$ | 1.2300E-07 | 1.2295E-07 | 5E-11 | 0.0406 |
| $E_{XY2}$ | -2.1300E-06 | -2.1305E-06 | 5E-10 | -0.0234 |
| $E_{YY1}$ | -2.2000E-04 | -2.2195E-04 | -1.95E-06 | 0.8863 |
| $E_{C(0Y)X}$ | 2.6100E-05 | 2.6097E-05 | -3E-09 | -0.0114 |
| $E_{Xt0}$ | 6.1100E-04 | 6.1179E-04 | 7.9E-07 | 0.1292 |
| $E_{Yt0}$ | 6.2200E-04 | 6.2196E-04 | -4E-08 | -0.0064 |
| $C_{XXX}$ | 1.1000E-04 | 1.1000E-04 | 0.0000 | 0.0000 |
| $C_{XYX}$ | 1.2000E-04 | 1.2000E-04 | 0.0000 | 0.0000 |
| $C_{YYY}$ | 5.5000E-04 | 5.5000E-04 | 0.0000 | 0.0000 |
| $C_{CXY}$ | 6.4000E-06 | 6.4000E-06 | 0.0000 | 0.0000 |
| $C_{CYY}$ | 6.5000E-06 | 6.5000E-06 | 0.0000 | 0.0000 |
| $C_{CCY}$ | 6.6000E-08 | 6.5999E-08 | -1E-12 | -0.0015 |

Figure 5.5 shows the simulated and predicted LDBB readings for the simulated and estimated model parameter values in Table 5.4. Simulated and estimated values are close to each other. As shown in Figure 5.5, the simulated and predicted readings are similar.

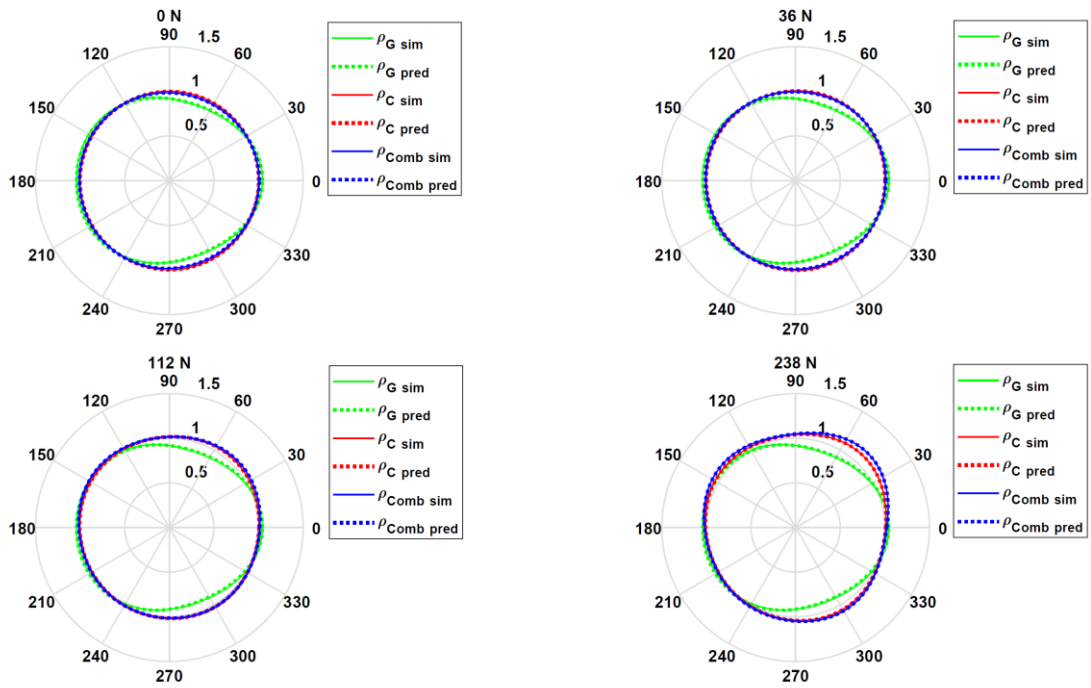

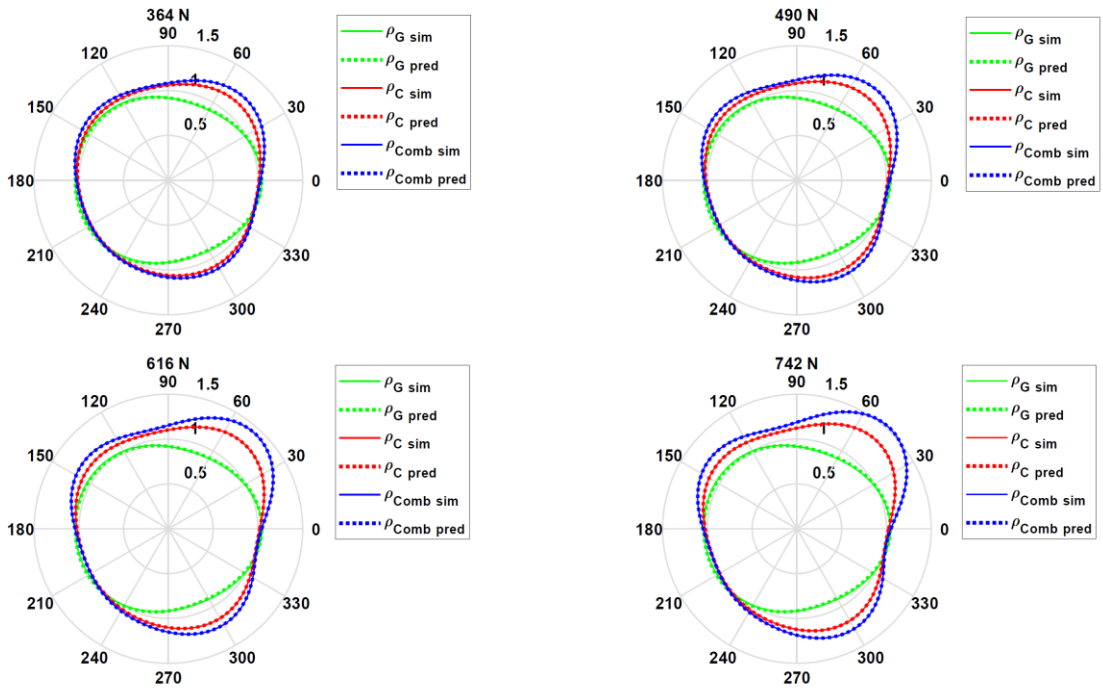


Figure 5.5. Simulated and predicted LDBB readings for values listed in Table 5.4 for eight different force levels (0, 36,112, 238, 364, 490, 616, and 742 N). $\rho_{\text{G sim}}$, $\rho_{\text{C sim}}$, $\rho_{\text{Comb sim}}$, $\rho_{\text{G pred}}$, $\rho_{\text{C pred}}$ and $\rho_{\text{Comb pred}}$ is the simulated geometric, compliance, combined and predicted geometric, compliance, and combined readings respectively.

## 5.7. Experimental Results and discussion

Figure 5.6 shows the loaded double ball bar test setup. The test is conducted on a machine tool with the configuration wCAFYXZt. The LDBB has a length of 150 mm, and the test feed rate is 2000 mm/min. The circular trajectory is in the XY plane with starting and ending angles of $0^{\circ}$and $360^{\circ}$, respectively. Radial displacement readings are measured for seven tests at forces of 36, 112, 238, 364, 490, 616, and 742N corresponding to pressure levels of 0.4, 1, 2, 3, 4, 5, and 6 bars internally applied to the LDBB, respectively. The radial displacement readout has a 0.00024 mm resolution. The raw data which was captured by the LDBB and readings were compensated for the setup deflection by using (5.38)

$$\delta = P \times 2.33 \times cos^2\theta \tag{5.38}$$

where $\delta$ (µm), $P$ (bar), and $\theta$ (degree) are the deflection at the workpiece ball, the air pressure, and the angle of the LDBB with the horizontal plane, respectively. The LDBB is perpendicular to the horizontal plane, therefore $\theta = 0$ degree.

Both the tool and the workpiece balls have a radii of 30 mm. According to ISO 3290-1:2014 [17], spheres of that radius can be reasonably well produced up to grade G20, i.e., with a tolerance in diameter of $\pm$ 11.5 µm; alternatively, the American Bearing Manufacturers Association standard defines tolerances of $\pm$12.5 µm for a corresponding grade G25 sphere. The LDBB measurement instrument features steel spheres for general industrial use. Thus, it must be assumed that each measurement contains an error component that is attributable to the imperfect shape of the sphere. It is possible to manufacture spheres according to much tighter roundness tolerance, e.g., the IBS Spindle Error Analyzer® features spheres with a roundness of less than $\pm$ 25nm [18]. The use of such spheres can reduce the complexity of understanding the measurement data as well as the time required to perform a measurement. Alternatively, one needs to employ error separation methods such as the Ball Reversal Method to quantify the contribution of the sphericity on the measurand [19]. For the work described in this manuscript, the form error of the spheres has not been compensated for. Based on the CMM measurement of these spheres, their form errors may contribute at most 30 µm. This means, that the model inaccurately re-attributes this error to the described kinematic machine tool errors. Nevertheless, this does not affect the modeling approach, as the measurement data, in general, should be compensated for this error before the model parameter estimation.

.

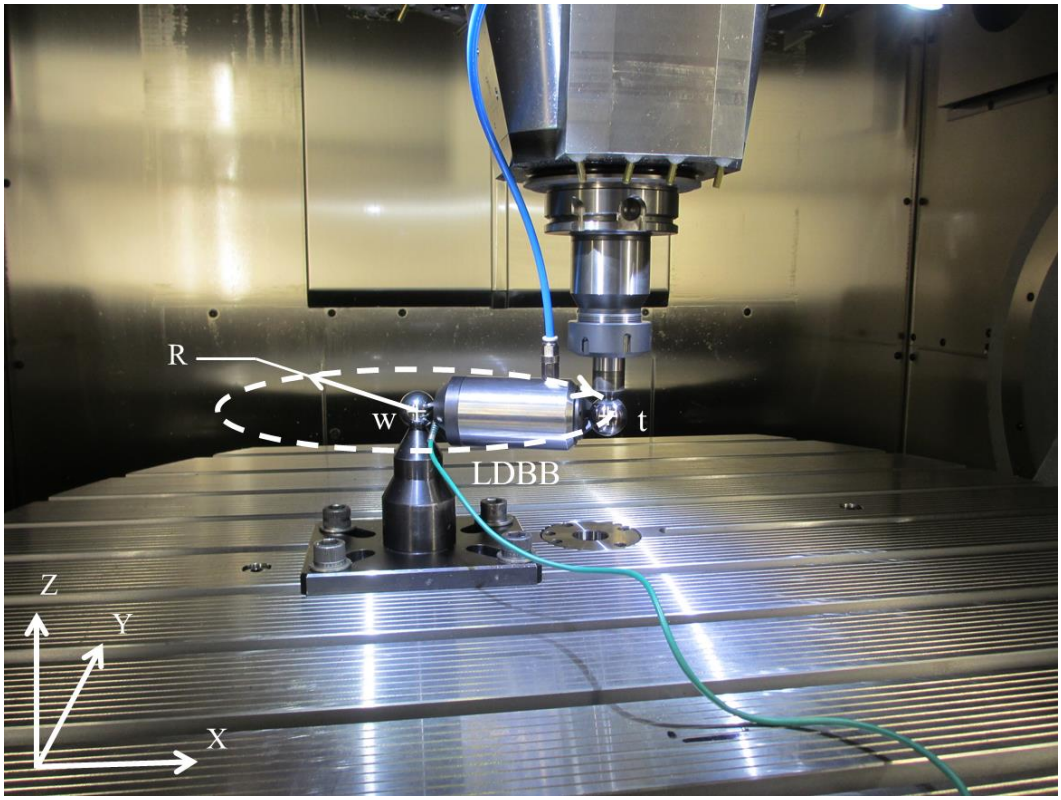


Figure 5.6. Loaded double ball bar test setup. The direction of the test is clockwise. The work ball is fixed, and the tool ball is moving. The test is conducted in the XY plane.

### 5.7.1. Global (overall) compliance and geometric parameters

Using the results from all force levels at once in Eq.(5.37) yields global estimates for the compliance and geometric parameters. The estimated compliance and geometric parameters values are listed in Table 5.5 and Table 5.6, respectively.

Table 5.5. Estimated global compliance value ( $^{mm}/_{N}$ ) of X- and Y-axis using all force data at once.

| $C_{X_{Estimated}}$ and $C_{Y_{Estimated}}$ | | | | | | | |
|---|---|---|---|---|---|---|---|
| | | Wrench | | | | | |
| | | $F_{XX}$ | $F_{YX}$ | $M_{CX}$ | $F_{XY}$ | $F_{YY}$ | $M_{CY}$ |
| Twist | $\delta_{XX}$ | 6.19E-05 | 7.98E-07 | 0 | 0 | 0 | 0 |
| | $\delta_{YX}$ | 0 | 0 | 0 | 0 | 0 | 0 |
| | $\delta_{CX}$ | 0 | 0 | 0 | 0 | 0 | 0 |
| | $\delta_{XY}$ | 0 | 0 | 0 | 0 | 0 | 0 |
| | $\delta_{YY}$ | 0 | 0 | 0 | 0 | 4.61E-05 | 0 |
| | $\delta_{CY}$ | 0 | 0 | 0 | -2.69E-08 | -1.66E-08 | -1.10E-09 |

Table 5.6. Estimated global geometry value (rad, mm, or mm/m) of X- and Y-axis using all pressure data at once.

| $E_{XX1}$ | $E_{YX2}$ | $E_{XY2}$ | $E_{YY1}$ | $E_{C(0Y)X}$ | $E_{Xt0}$ | $E_{Yt0}$ |
|---|---|---|---|---|---|---|
| -0.00013 | 4.34E-07 | -7.26E-07 | -9.86E-05 | 1.15E-06 | 0.003891 | -0.00062 |

Figure 5.7 shows the experimental and model prediction of the loaded telescopic double ball-bar from 36 to 742 N force levels. The estimation is conducted without the 112 N dataset, which will be studied in the next section as it exhibits a non-linear behavior. As expected, the loaded telescopic double ball-bar readings increase with the applied force. Also, although the shape of the trace predicted generally follows the contour of the measurements there is a cyclical difference between them.

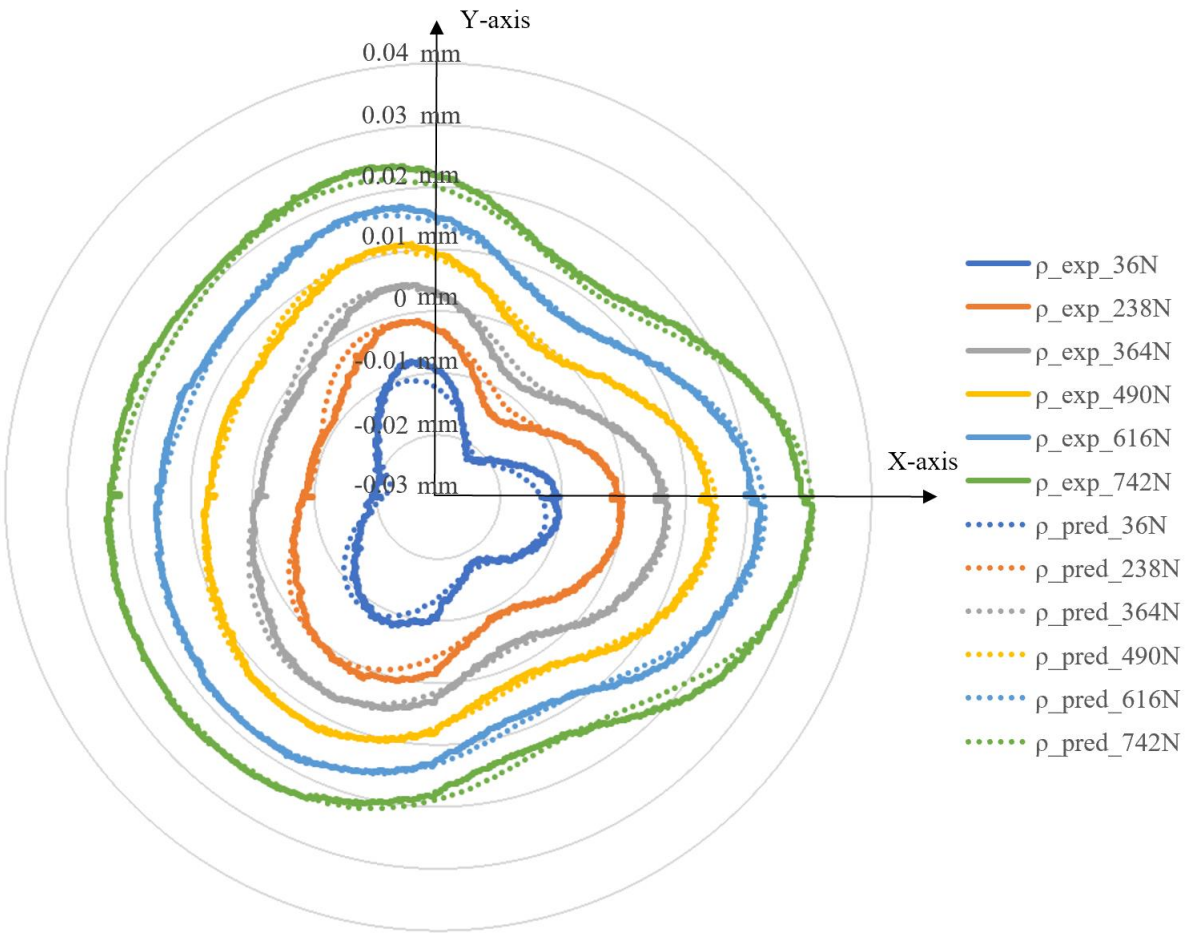


Figure 5.7. Experimental and predicted global loaded double ball bar readings for X and Y-axis simultaneously with seven different levels of applied force. ρ_exp and ρ_pred are the experimental and predicted readings of a loaded double ball bar.

The model allows studying the relative contribution of the geometric and compliance parameters to the response. Figure 5.8 shows the predicted readings in the absence of set-up errors ($E_{\mathrm{Xt0}}$ and $E_{\mathrm{Yt0}}$) for (a) all compliance and geometric parameters, (b) the compliance parameters only, and (c) the geometric parameters only. Since the geometry of the machine is modeled as invariant with a load, all the predicted loaded geometric readings are identical. In Figure 5.8 (b) the maximum and minimum predicted radial LDBB readings attributed to the compliance are 0.046 and 0 mm, respectively, which results in a 0.046 mm radial variation. In Figure 5.8 (c) the maximum and minimum predicted radial LDBB readings due to the estimated geometric errors are -0.007 mm and -0.026 mm, respectively, which results in a 0.019 mm departure from the nominal circular trajectory. The radial variation due to compliance effects is more than 3 times that of geometric errors.

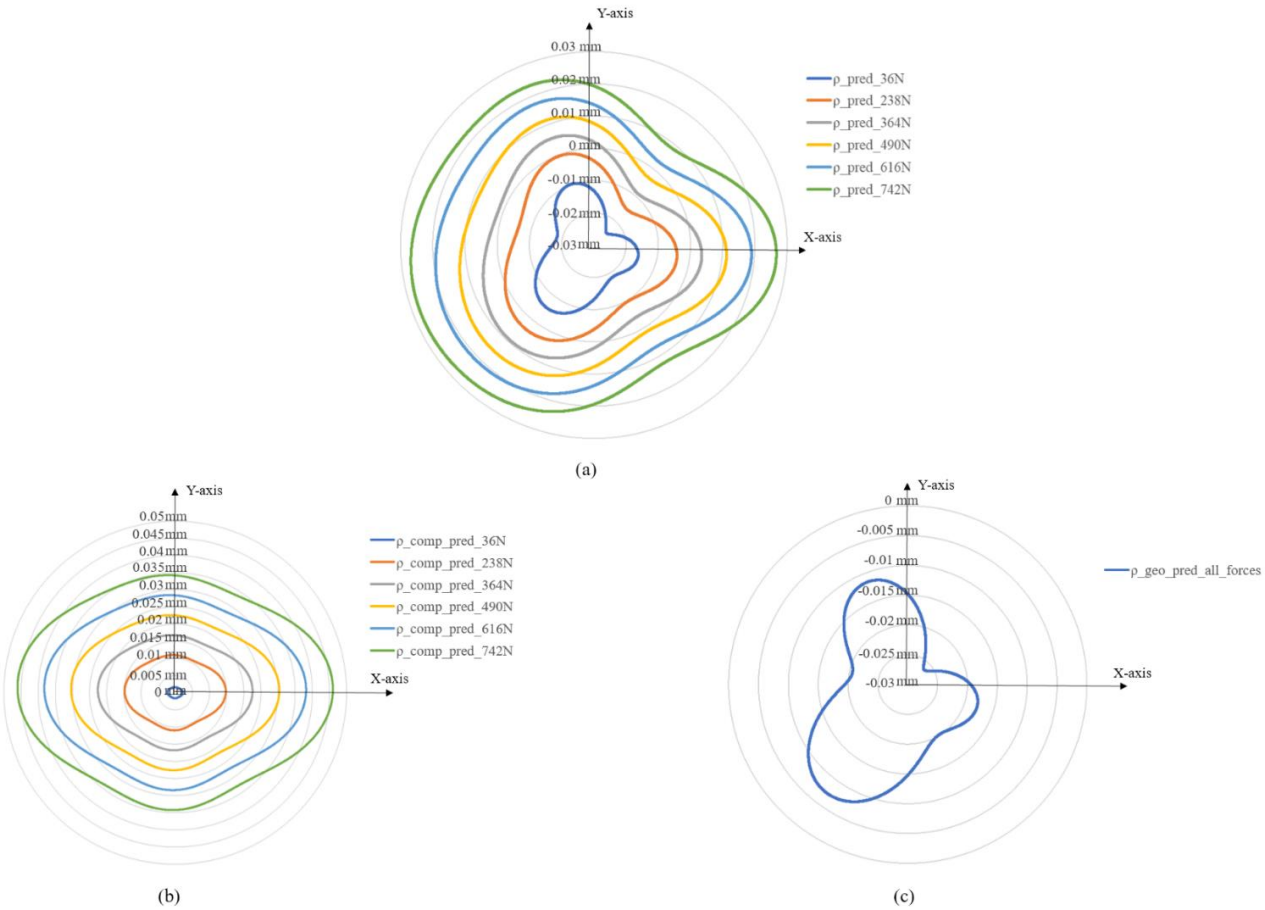


Figure 5.8. Predicted global loaded double ball bar readings for the X and Y-axis simultaneously with seven different levels of applied force. (a) Predicted combined readings (ρ_pred). (b) Predicted compliance readings (ρ_comp_pred). (c) Predicted geometric readings (ρ_geo_pred).

Figure 5.9 and Figure 5.10 presents predicted readings of the loaded double ball bar from the estimated global compliance and geometric parameters at the highest force (742 N), respectively. In Figure 5.9 (a) the dominant equivalent compliance's ($C_{\mathrm{XXX}}$, $C_{\mathrm{YYY}}$) impact on the loaded circular test readings are predicted to be around 0.045 and 0.034 mm peak-to-peak. In Figure 5.9 (b) the impact of non-dominant equivalent compliances ($C_{\mathrm{XYX}}$, $C_{\mathrm{CXY}}$, $C_{\mathrm{CYY}}$ and $C_{\mathrm{CCY}}$) are predicted to be around 0.00058, 0.0022, 0.0014 and 0.0045 mm peak-to-peak.

In Figure 5.10 (a) the loaded geometric parameters ($E_{\mathrm{XX1}}$, $E_{\mathrm{YY1}}$) impact on the loaded circular test readings is predicted to be around 0.019 and 0.014 mm peak-to-peak. In Figure 5.10 (b) the impact of loaded geometric parameters ($E_{\mathrm{YX2}}$, $E_{\mathrm{XY2}}$, $E_{\mathrm{C(0Y)X}}$, $E_{\mathrm{Xt0}}$ and $E_{\mathrm{Yt0}}$) are predicted to be around 0.0074, 0.012, 0.00017, 0.0076 and 0.0012 mm peak-to-peak.

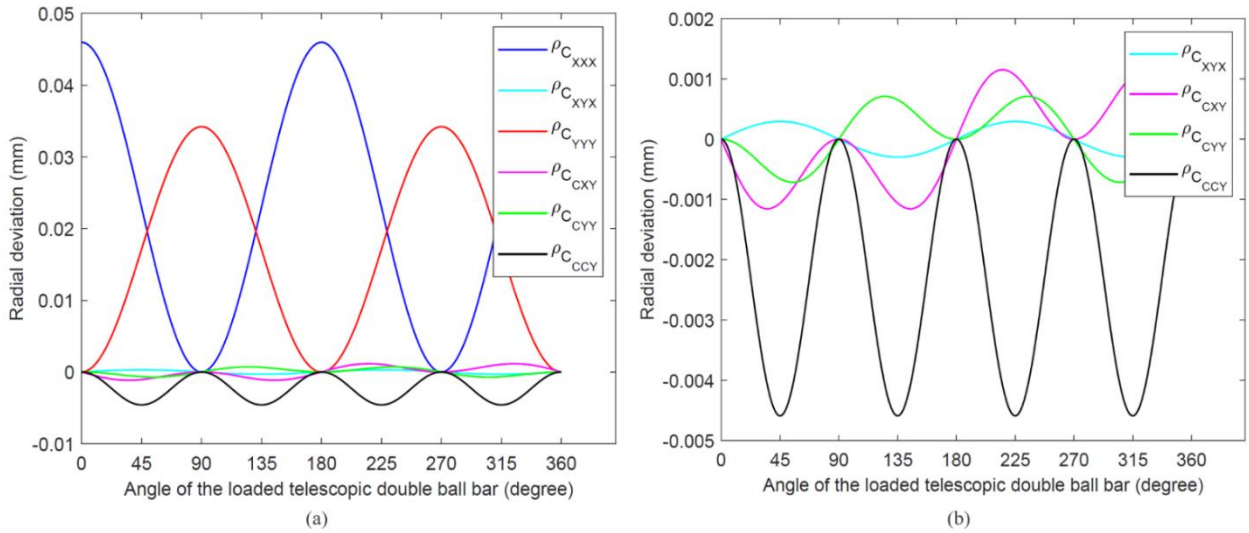


Figure 5.9. Predicted readings of the loaded double ball bar (radial deviation versus the angle of the ball bar with the X-axis during the circular test) from the estimated global compliance parameters at the highest force (742 N). (a) $C_{\mathrm{XXX}}$, $C_{\mathrm{XYX}}$, $C_{\mathrm{YYY}}$ , $C_{\mathrm{CXY}}$, $C_{\mathrm{CYY}}$ and $C_{\mathrm{CCY}}$. (b) $C_{\mathrm{XYX}}$, $C_{\mathrm{CXY}}$, $C_{\mathrm{CYY}}$ and $C_{\mathrm{CCY}}$.

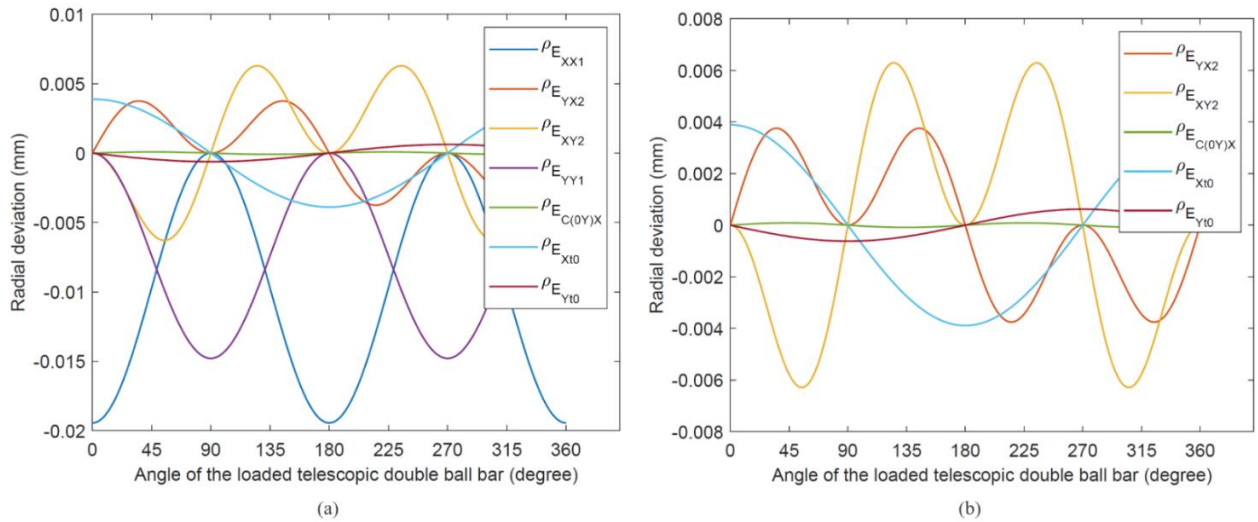


Figure 5.10. Predicted readings of the loaded double ball bar (radial deviation versus the angle of the ball bar with the X-axis during the circular test) from the estimated global constant geometric parameters at the highest force (742 N). (a) $E_{\mathrm{XX1}}$, $E_{\mathrm{YX2}}$, $E_{\mathrm{XY2}}$, $E_{\mathrm{YY1}}$, $E_{\mathrm{C(0Y)X}}$, $E_{\mathrm{Xt0}}$ and $E_{\mathrm{Yt0}}$. (b) $E_{\mathrm{YX2}}$, $E_{\mathrm{XY2}}$, $E_{\mathrm{C(0Y)X}}$, $E_{\mathrm{Xt0}}$ and $E_{\mathrm{Yt0}}$.

### 5.7.2. Local compliance and geometric parameters

By using only two adjacent force levels: [36 and 112; 112 and 238; 238 and 364; 364 and 490; 490 and 616; 616 and 742] N a set of local compliance and geometric parameters are estimated. The experimental and predicted readings for a particular set of forces are illustrated in Figure 5.11(a). From 238 N force, the predicted readings more closely follow the experimental readings. At 112 N force, results do not follow the general trend. This set of data significantly affects the estimated parameters.

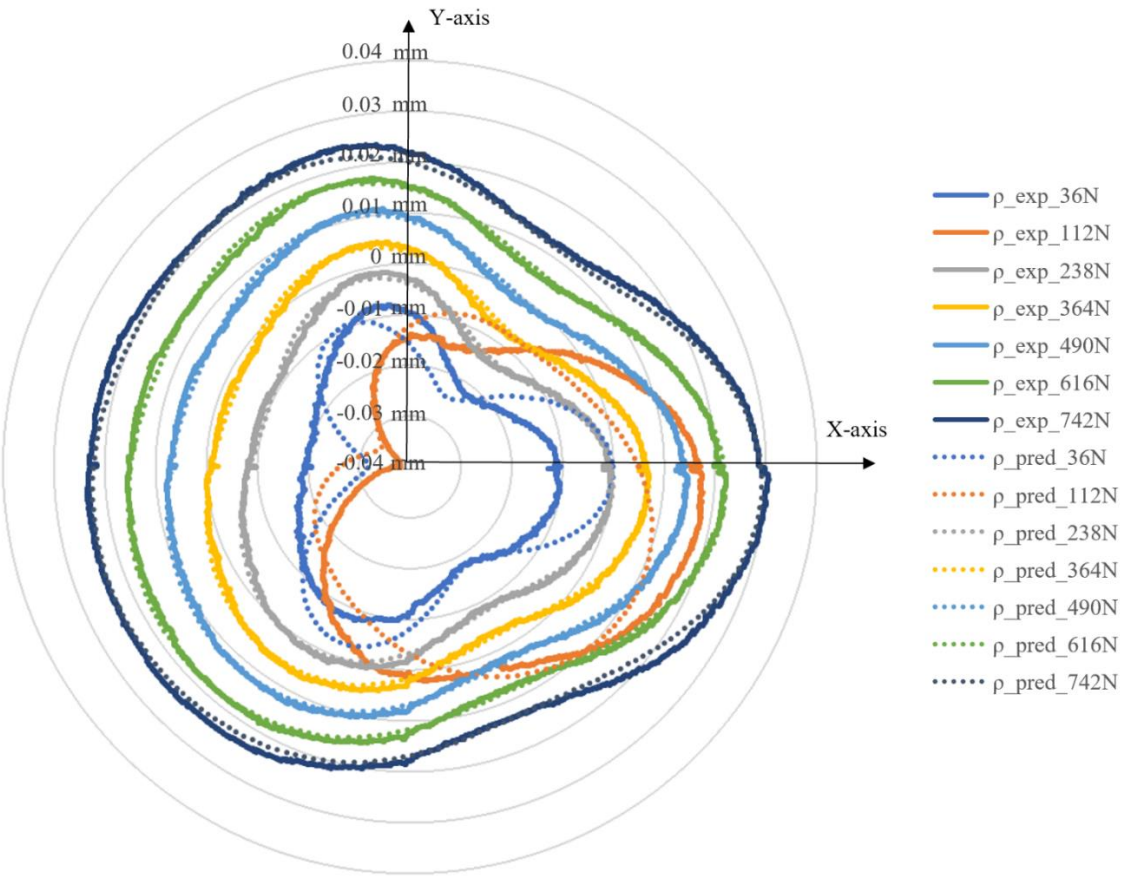


(a)

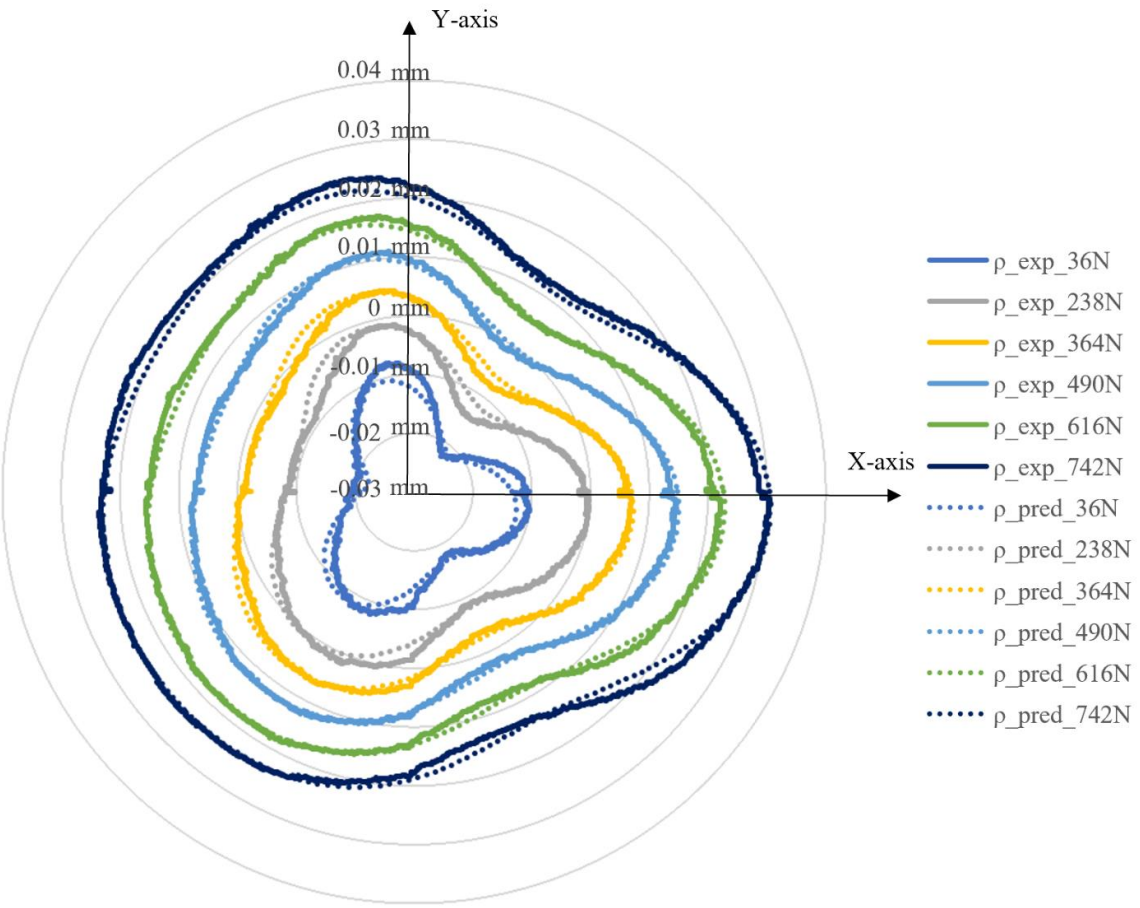


(b)

Figure 5.11. Experimental and predicted local loaded telescopic double ball bar readings for X and Y-axis simultaneously with seven different levels of applied force. ρ_exp and ρ_pred are the experimental and predicted readings of a loaded telescopic double ball bar. (a) Includes the 112 N force level results and the predicted traces are obtained using parameters estimated using the following two adjacent force levels ([36, 112], [112, 238], etc.). (b) Without 112 N force level and using the following two adjacent force levels ([36, 238], [238, 364], etc.).

Figure 5.12 shows the predicted local loaded telescopic double ball bar readings calculated using the estimated machine parameters, excluding the tool offsets. Three simulations are conducted: (a) compliance and geometric parameters; (b) compliance parameters only and (c) geometric parameters only. Although theoretically unexpected the estimated geometry changes with force levels. A possible explanation is that the compliance model cannot fully explain the change in response and so the geometric errors are used to explain those effects. The predicted LDBB reading variation due to geometry variation is at most 0.0085 mm over the force range. This compares with 0.019 mm

attributed to the global geometry obtained when using all force data at once. So the variation is early half the global value, which is not negligible. However, the overall shape of the geometric effect remains similar.

Figure 5.13 and Figure 5.14 present predicted readings of the loaded double ball bar from the estimated local compliance and geometric parameters at the highest force (742 N), respectively. In Figure 5.13 (a) the dominant equivalent compliance's ($C_{\mathrm{XXX}}$, $C_{\mathrm{YYY}}$) impact on the loaded circular test readings are predicted to be around 0.048 and 0.036 mm peak-to-peak. In Figure 5.13 (b) the impact of non-dominant equivalent compliances ($C_{\mathrm{XYX}}$, $C_{\mathrm{CXY}}$, $C_{\mathrm{CYY}}$ and $C_{\mathrm{CCY}}$) are predicted to be around 0.0018, 0.0064, 0.001 and 0.0036 mm peak-to-peak.

In Figure 5.14 (a) the loaded geometric parameters ($E_{\mathrm{XX1}}$, $E_{\mathrm{YY1}}$) impact on the loaded circular test readings is predicted to be around 0.022 and 0.017 mm peak-to-peak. In Figure 5.14 (b) the impact of loaded geometric parameters ($E_{\mathrm{YX2}}$, $E_{\mathrm{XY2}}$, $E_{\mathrm{C(0Y)X}}$, $E_{\mathrm{Xt0}}$ and $E_{\mathrm{Yt0}}$) are predicted to be around 0.012, 0.014, 0.00082, 0.0068 and 0.0031 mm peak-to-peak.

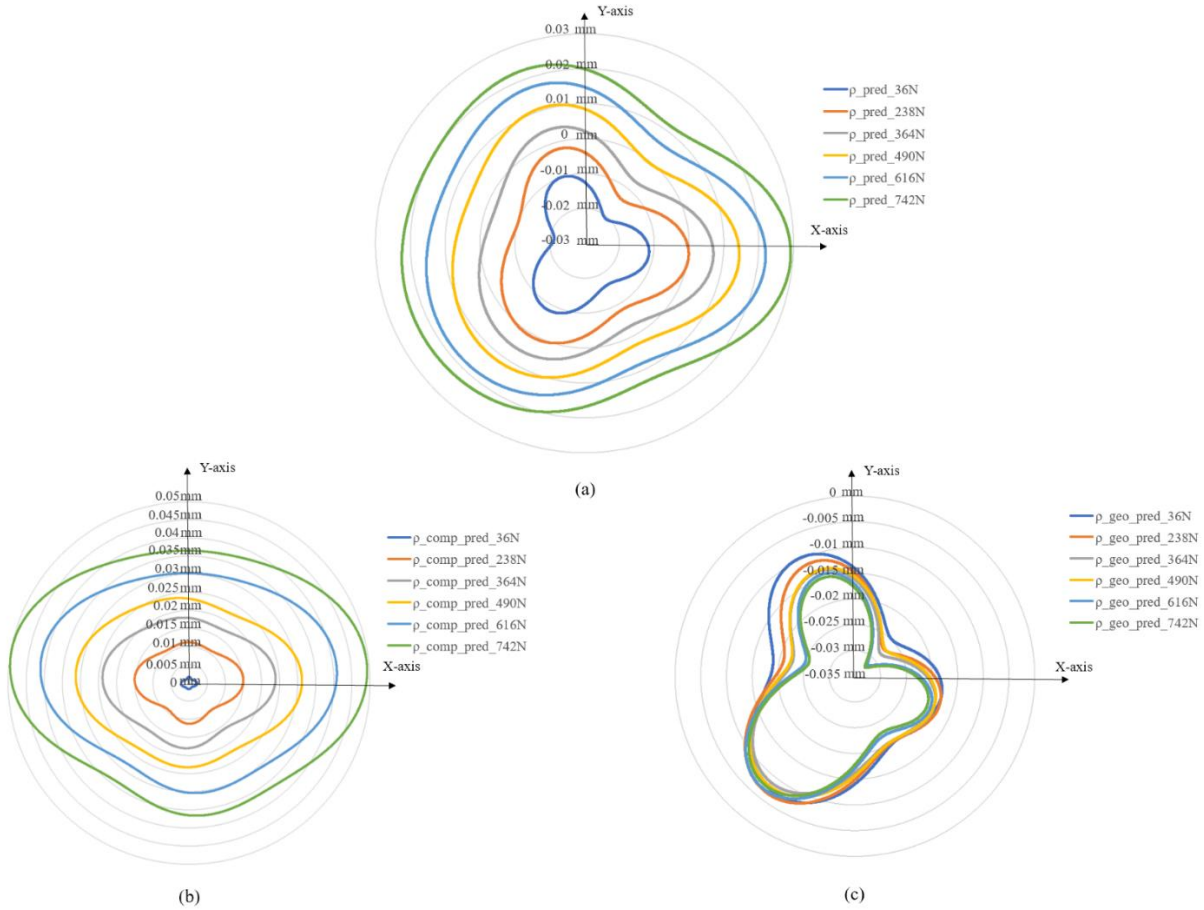


Figure 5.12. Predicted local loaded telescopic double ball bar readings for the X and Y-axis simultaneously with seven different levels of applied force. (a) Predicted local combined readings (ρ_pred). (b) Predicted local compliance readings (ρ_comp_pred). (c) Predicted local geometric readings (ρ_geo_pred).

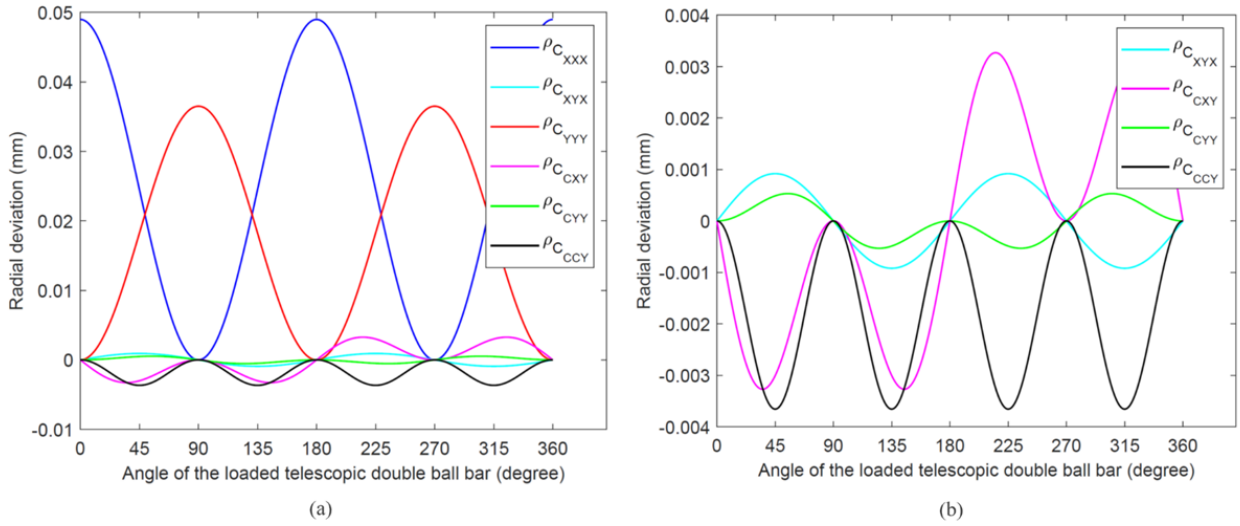


Figure 5.13. Predicted readings of the loaded double ball bar (radial deviation versus the angle of the ball bar with the X-axis during the circular test) from the estimated local compliance parameters at the highest force (742 N). (a) $C_{\mathrm{XXX}}$, $C_{\mathrm{XYX}}$, $C_{\mathrm{YYY}}$ , $C_{\mathrm{CXY}}$, $C_{\mathrm{CYY}}$ and $C_{\mathrm{CCY}}$. (b) $C_{\mathrm{XYX}}$, $C_{\mathrm{CXY}}$, $C_{\mathrm{CYY}}$ and $C_{\mathrm{CCY}}$

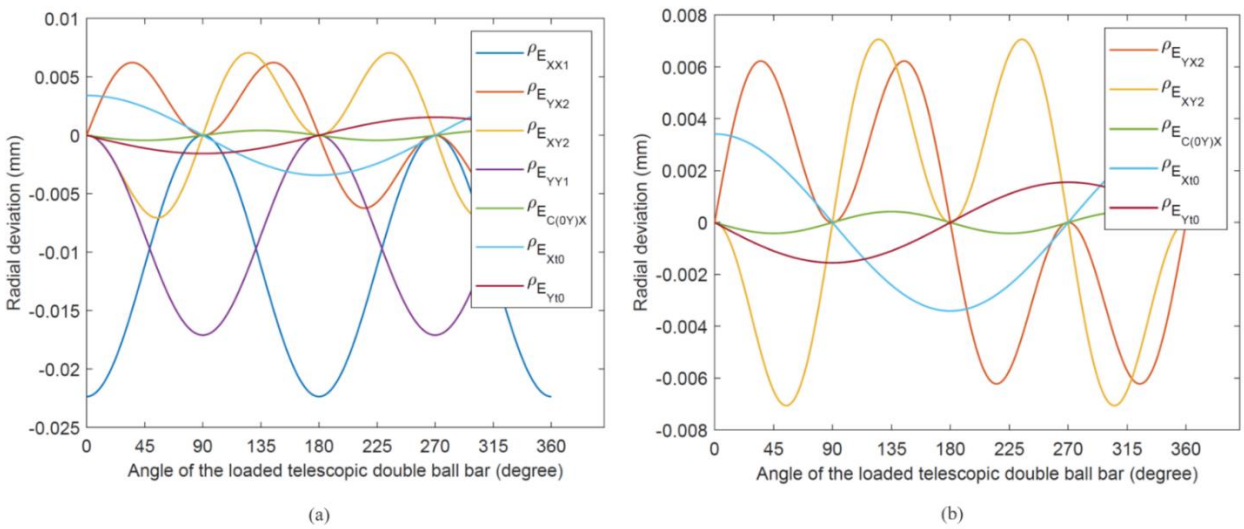


Figure 5.14. Predicted readings of the loaded double ball bar (radial deviation versus the angle of the ball bar with the X-axis during the circular test) from the estimated local geometric parameters at the highest force (742 N). (a) $E_{\mathrm{XX1}}$, $E_{\mathrm{YX2}}$, $E_{\mathrm{XY2}}$, $E_{\mathrm{YY1}}$, $E_{\mathrm{C(0Y)X}}$, $E_{\mathrm{Xt0}}$ and $E_{\mathrm{Yt0}}$. (b) $E_{\mathrm{YX2}}$, $E_{\mathrm{XY2}}$, $E_{\mathrm{C(0Y)X}}$, $E_{\mathrm{Xt0}}$ and $E_{\mathrm{Yt0}}$.

*Table 5.7* and

*Table* 5.8 list the estimated local compliance and geometric parameters values.

Table 5.7. Estimated local compliances values (mm/N, $^{\mathrm{rad}}/_{\mathrm{N}}$ or $^{\mathrm{rad}}/_{\mathrm{N\ mm}}$) for different sets of two force levels.

| Force (N) | $C_{\mathrm{XXX}}$ | $C_{\mathrm{XYX}}$ | $C_{\mathrm{YYY}}$ | $C_{\mathrm{CXY}}$ | $C_{\mathrm{CYY}}$ | $C_{\mathrm{CCY}}$ |
|---|---|---|---|---|---|---|
| $F_{1-2}$ (36 and 238) | 6.15E-05 | -1.65E-06 | 4.64E-05 | 8.04E-08 | -2.79E-08 | -2.88E-09 |
| $F_{2-3}$ (238 and 364) | 6.28E-05 | 1.07E-06 | 4.72E-05 | -6.94E-08 | 3.13E-09 | -1.92E-09 |
| $F_{3-4}$ (364 and 490) | 6.54E-05 | 5.54E-07 | 4.94E-05 | -6.03E-08 | -3.11E-08 | -1.38E-09 |
| $F_{4-5}$ (490 and 616) | 6.37E-05 | 2.56E-06 | 4.74E-05 | -3.67E-08 | -2.60E-08 | -1.08E-09 |
| $F_{5-6}$ (616 and 742) | 6.60E-05 | 2.48E-06 | 4.92E-05 | -7.63E-08 | 1.24E-08 | -8.76E-10 |

Table 5.8. Estimated local geometric values (rad, mm, or mm/m) for different sets of two force levels.

| Force (N) | $E_{\mathrm{XX1}}$ | $E_{\mathrm{YX2}}$ | $E_{\mathrm{XY2}}$ | $E_{\mathrm{YY1}}$ | $E_{\mathrm{C(0Y)X}}$ | $E_{\mathrm{Xt0}}$ | $E_{\mathrm{Yt0}}$ |
|---|---|---|---|---|---|---|---|
| $F_{1-2}$ (36 and 238) | -0.00012 | 2.75E-07 | -7.66E-07 | -9.36E-05 | 3.71E-06 | 0.004438 | 5.29E-05 |
| $F_{2-3}$ (238 and 364) | -0.00013 | 4.91E-07 | -7.79E-07 | -9.91E-05 | -6.08E-07 | 0.004025 | 0.0003 |
| $F_{3-4}$ (364 and 490) | -0.00014 | 5.27E-07 | -6.77E-07 | -0.00011 | 6.41E-07 | 0.003821 | -0.00036 |
| $F_{4-5}$ (490 and 616) | -0.00014 | 5.01E-07 | -6.68E-07 | -0.0001 | -5.91E-06 | 0.003525 | -0.00093 |
| $F_{5-6}$ (616 and 742) | -0.00015 | 7.19E-07 | -8.15E-07 | -0.00011 | -5.58E-06 | 0.003413 | -0.00155 |

*Figure 5.16* show the estimated experimental compliance and geometric error values. In Figure 5.15 by increasing the force the majority of compliance terms increase such as $C_{\mathrm{XXX}}$, $C_{\mathrm{XYX}}$, $C_{\mathrm{YYY}}$ and $C_{\mathrm{CCY}}$. The other two, $C_{\mathrm{CXY}}$ and $C_{\mathrm{CYY}}$ show no clear trends. In Figure 5.16 as the force increases, most of the loaded geometric terms decrease such as the scale gain errors $E_{\mathrm{XX1}}$ and $E_{\mathrm{YY1}}$, the out-of-squareness

$E_{C(0Y)X}$ and the tool offsets $E_{Xt0}$ and $E_{Yt0}$. Nevertheless, some increase such as the quadratic straightness $E_{YX2}$ and $E_{XY2}$.

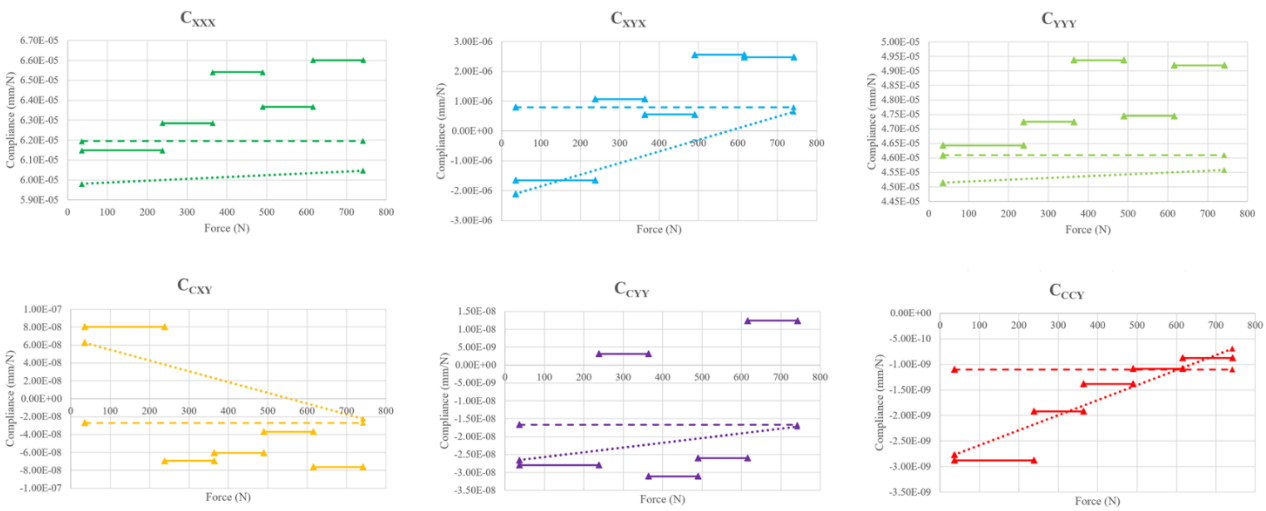


Figure 5.15. Estimated local compliances were acquired employing data from two adjacent force levels (dashed and dotted lines from 36 to 742 N depict the constant and variable global compliance value obtained by using all force results, respectively).

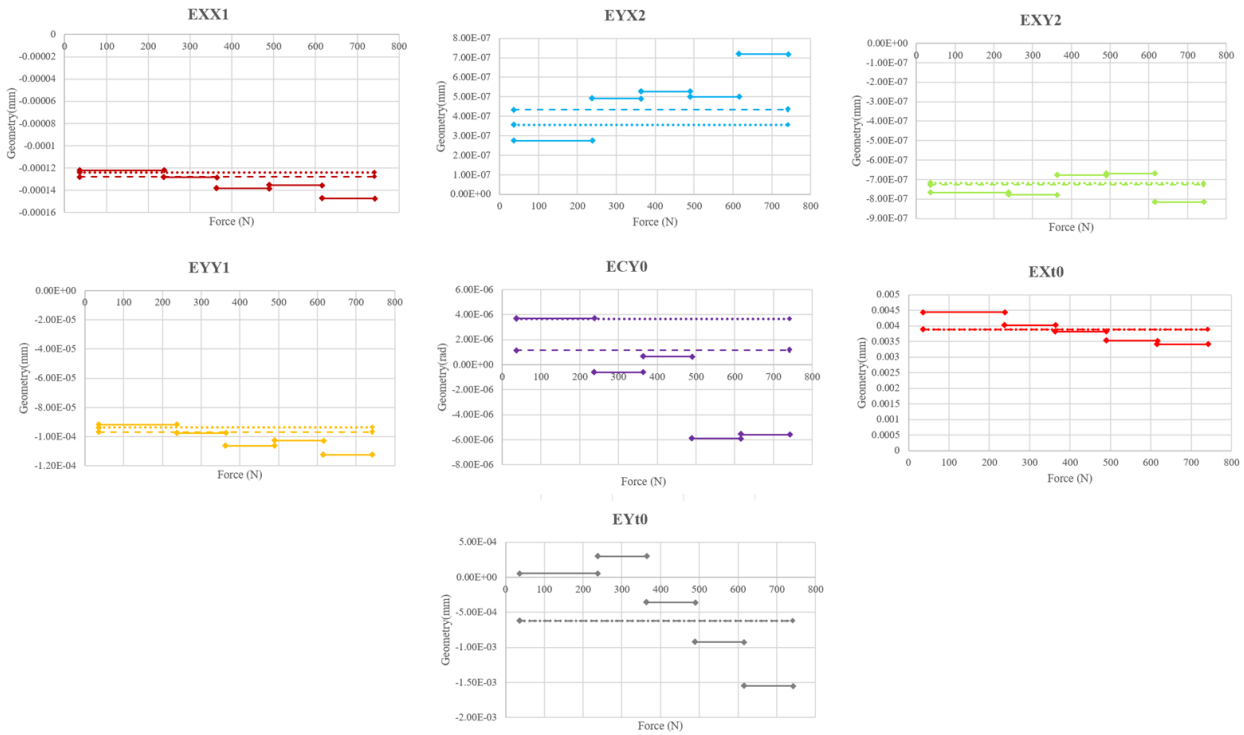


Figure 5.16. Estimated local geometric parameters were acquired employing data from two continuous force levels (dashed and dotted lines from 36 to 742 N depict the constant and variable unique global geometric parameter value for each compliance term, respectively).

### 5.7.3. Variable compliance

Results obtained for local compliances suggest that the values of compliances vary slightly with the applied load. This appears to cause changes in the estimated geometric error parameters which contravenes the definition of geometric errors which should be invariant with the applied load. To analyze the change of compliance parameters as a function of force ($F$) a solution is now proposed that consists of using a linear model for each compliance term such as

$$C_{\mathrm{XXX}} = C_{\mathrm{XXX0}} + C_{\mathrm{XXX1}}F \tag{5.39}$$

Then, the elasto-geometric Jacobian ($J_{\mathrm{H}}$) in Eq.(5.36) is expanded to include the new linear (degree one) compliance terms by adding an adjacent column for each existing column, corresponding to a constant compliance term (degree 0), which is the same value but multiplied by the relevant force level for each row. Each row corresponds to a force level that generated that relevant LDBB reading. These estimated parameters as a function of force are shown in Figure 5.15 as a dotted line from 36 to 742 N. To observe the modeling improvement of the variable compliance in comparison with constant compliance values, the root mean square error is used

$$RMSE = \sqrt{\frac{\sum_{i=1}^{n}(Predicted_i - Measured_i)^2}{n}} \tag{5.40}$$

where Predicted, Measured and n represents predicted LDBB readings, experimental LDBB readings, and the number of measurements, respectively. The RMSE value for produced LDBB reading for all force levels by constant and variable compliance are 0.0011 and 0.0009 mm, respectively which shows a further reduction of 18% using the variable compliance model. To determine how well the predicted data aligns with the measured one, the normalized root mean square error fitness is used

$$fitness\ (\%) = \left(1 - \frac{RMSE}{|Measured_{i,max} - Measured_{i,min}|}\right) \times 100 \tag{5.41}$$

Table 5.9 presents the fitting percentage for predicted readings from estimated global, variable global, and local compliance parameters. The fit improves slightly with the force level as the compliance effect becomes more significant. All fitting percentages exceed 91%. Compared to the constant variable model, the linearly variable compliance model improves the fit only slightly by just over 1% when using all force level data.

Table 5.9. The fitting values for global, variable global, and local compliance predicted readings with different force levels.

| LDBB readings for different force level | Fitting with global compliance | Fitting with variable global compliance | Fitting with local compliance |
|---|---|---|---|
| $\rho_{36}$ (%) | 92.4 | 93.7 | 91.7 |
| $\rho_{238}$ (%) | 93.0 | 94.2 | 95.3 |
| $\rho_{364}$ (%) | 92.5 | 93.8 | 95.4 |
| $\rho_{490}$ (%) | 93.0 | 94.2 | 95.8 |
| $\rho_{616}$ (%) | 93.4 | 94.6 | 96.0 |
| $\rho_{742}$ (%) | 93.9 | 95.0 | 96.2 |

## 5.8. Conclusion

The elasto-geometric model is contextualized to the data gathered during a loaded 2D circular test implemented using a loaded double ball bar (LDBB) to simultaneously estimate the machine tool X- and Y-axis equivalent compliances and geometric errors. The compliances are said to be “equivalent” because although only two axes are mobile during the test, the machine has five axes and all axes may contribute to the observed volumetric deflections. The tests are executed using seven levels of

forces of 36, 112, 238, 364, 490, 616, and 742 N. At lower forces the geometric errors are dominant whilst at higher forces compliance errors dominate. When using all data to build a single geometry and compliance set of parameters (global constant compliance model) the radial volumetric variations due to geometric errors and compliance are estimated at 0.019 mm and 0.046 mm, respectively, making compliance dominant by more than three times. The impact of dominant and non-dominant equivalent global compliance $C_{\mathrm{XXX}}$, $C_{\mathrm{YYY}}$, $C_{\mathrm{XYX}}$, $C_{\mathrm{CXY}}$, $C_{\mathrm{CYY}}$ and $C_{\mathrm{CCY}}$ on the loaded circular test readings at the highest force level of 742 N are predicted to be around 0.045, 0.034, 0.00058, 0.0022, 0.0014, and 0.0045 mm peak-to-peak, respectively. The impact of loaded geometric parameter $E_{\mathrm{XX1}}$, $E_{\mathrm{YY1}}$, $E_{\mathrm{YX2}}$, $E_{\mathrm{XY2}}$, $E_{\mathrm{C(0Y)X}}$, $E_{\mathrm{Xt0}}$ and $E_{\mathrm{Yt0}}$ on the loaded circular test readings are predicted to be around 0.019, 0.014, 0.0074, 0.012, 0.00017, 0.0076 and 0.0012 mm peak-to-peak, respectively. The dominant global compliances are $C_{\mathrm{XXX}}$ and $C_{\mathrm{YYY}}$ at 0.0619 and 0.0461 $\mu\mathrm{m/N}$, respectively.

By feeding the elasto-geometric model with pairs of adjacent force data the evolution of compliance with changes in the applied force is observed. Although theoretically unexpected, the estimated geometry changes with force levels. The radial volumetric largest change due to variation in the estimated geometry across the range of tested forces (local model) amounts to 0.0085 mm whereas the global model radial volumetric effects due to geometric errors are estimated at 0.019 mm. This means that the estimated change in geometry is significant. As the geometric errors would ideally not change for different force levels, this points to the need to enrich the compliance model so that it can better explain the change in the machine behavior across the tested force range. As the force increases the majority of compliance terms increase such as $C_{\mathrm{XXX}}$, $C_{\mathrm{XYX}}$, $C_{\mathrm{YYY}}$ and $C_{\mathrm{CCY}}$. Two of the less significant compliances, $C_{\mathrm{CXY}}$ and $C_{\mathrm{CYY}}$, show no clear trends. Most of the loaded geometric terms decrease such as $E_{\mathrm{XX1}}$, $E_{\mathrm{YY1}}$, $E_{\mathrm{C(0Y)X}}$, $E_{\mathrm{Xt0}}$ and $E_{\mathrm{Yt0}}$ as the force increases but $E_{\mathrm{YX2}}$ and $E_{\mathrm{XY2}}$ increase. The change in local compliance suggests that the compliance may vary with the applied force. As the compliance is assumed to be constant this may be causing the apparent change in the geometric error parameters at different force levels. Consequently, the compliance model was enriched as a linear function of the applied force to process all force level data at once so that the estimated geometry is kept the same at all force levels. The root mean square error (RMSE) value for predicting the radial LDBB readings using the constant and linearly variable compliance models are 0.0011 and 0.0009 mm, respectively, for an improvement of about 18% using the variable compliance model. As all models predict over 91% of the experimental radial deviations, the use of a linear compliance model results in just over 1% fitting improvement.

## 5.9. Acknowledgments

This research was supported by the Natural Sciences and Engineering Research Council of Canada NSERC Canadian Network for Research and Innovation in Machining Technology–Phase 2: CANRIMT2 Grant number NSERC NETGP 479639 - 15 and by NSERC Discovery Grant number RGPIN-2016-06418. Researcher T. Laspas is acknowledged for experimental data. This Swedish part of the presented work was funded by the Centre for Design and Management of Manufacturing Systems DMMS at KTH and VINNOVA through the Eureka SMART COMACH project Grant Agreement ID: S0120.

## 5.10. References

1. Beglarzadeh, B., J.R.R. Mayer, and A. Archenti, *Modelling and indirect measurement of machine tool equivalent joint compliances.* CIRP Journal of Manufacturing Science and Technology, 2021. 35: p. 882-895.

2. Salgado, M.A., et al., *Evaluation of the stiffness chain on the deflection of end-mills under cutting forces.* International Journal of Machine Tools & Manufacture, 2005. 45(6): p. 727-739.

3. Archenti, A. and M. Nicolescu, *A top-down equivalent stiffness approach for prediction of deviation sources in machine tool joints.* CIRP Annals, 2017. 66(1): p. 487-490.

4. Gao, X., et al., *Stiffness modeling of machine tools based on machining space analysis.* The International Journal of Advanced Manufacturing Technology, 2016. 86(5-8): p. 2093-2106.

5. Shi, Y., et al., *A new top-down design method for the stiffness of precision machine tools.* The International Journal of Advanced Manufacturing Technology, 2015. 83(9-12): p. 1887-1904.

6. W.J. Lee and S.l. Kim, *Joint Stiffness Identification of an Ultra-Precision Machine for Machining Large-Surface Micro-Features.* International Journal of Precision Engineering and Manufacturing, 2009. 10(5): p. 115-121.

7. Kono, D. and A. Matsubara, *Investigation on Direction Dependency of Tool-Workpiece Compliance of Machine Tool.* Procedia CIRP, 2016. 46: p. 529-532.

8. Pawełko, P., et al., *A new measurement system to determine stiffness distribution in machine tool workspace.* Archives of Civil and Mechanical Engineering, 2021. 21(2).

9. Archenti, A., *A Computational Framework for Control of Machining System Capability : From Formulation to Implementation*, in *Department of Production Engineering Machine and Process Technology*. 2011, KTH Royal Institute of Technology: Stockholm, Sweden.

10. International Organization for Standardization, *ISO 230_4, Test code for machine tools — part 4: Circular tests for numerically controlled machine tools.* 2005.

11. Archenti, A., *Prediction of machined part accuracy from machining system capability.* CIRP Annals, 2014. 63(1): p. 505-508.

12. Bryan, J.B., *A simple method for testing measuring machines and machine tools.* Precision Engineering, 1982. 4(2): p. 61-69.

13. Y. Kakino, et al., *The Measurement of Motion Errors of NC Machine Tools and Diagnosis of their Origins by Using Telescoping Magnetic Ball Bar Method.* CIRP Annals, 1987.

14. Jiang, Z., et al., *Elasto-geometrical calibration of six-DOF serial robots using multiple identification models.* Mechanism and Machine Theory, 2021. 157.

15. Craig, J.J., *Introduction to Robotics, Mechanics, and Control*. 2005, Pearson Prentice Hall.

16. G. Zhang, et al., *Error Compensation of Coordinate Measuring Machines.* CIRP Annals, 1985. Volume 34(1): p. 445-448.

17. International Organization for Standardization, *ISO 3290-1, Rolling bearings- Balls- Part 1: Steel balls.* 2014.

18. International Organization for Standardization, *ISO 1101, Geometrical product specifications (GPS)-Geometrical tolerancing-Tolerances of form, orientation, location, and run-out.* 2017.

19. Evans, C.J., R.J. Hocken, and W.T. Estler, *Self-Calibration: Reversal, Redundancy, Error Separation, and 'Absolute Testing'.* CIRP Annals, 1996. 45(2): p. 617-634.

# CHAPTER 6 SENSORLESS LOADED TEST FOR MACHINE TOOL STIFFNESS CHARACTERIZATION

## 6.1. Abstract

Machine tools stiffness may affect a machined part's accuracy. Volumetric stiffness is measured by a novel test apparatus, named Ball-Roller Bearing Device (BRBD). The volumetric stiffness measurement procedure is conducted by a loaded circular test consisting of a commanded radial engagement between a ball attached to the table and a roller bearing mounted at the tool holder causing a radial force to develop. The engagement and force are calculated from the encoder readings and the servo motor current, respectively. Disturbance from non-compliant effects is removed by analyzing the data from at least two engagement levels. Predicted force and obtained volumetric compliance values are validated with the dynamometer table force and compliant rig artefact, respectively.

**Keywords:** Ball-roller bearing device (BRBD), sensorless, volumetric stiffness, machine tool

## 6.2. Introduction

Machine stiffness is a major criterion of performance for high-speed and accurate machining since the machine will deflect due to cutting forces and workpiece weight.

Machine tools static compliance and hysteresis measurement procedure are mentioned in ISO 230-1:2012 [1]. The static load is applied between the tool and workpiece and the resulting displacement is measured in the direction of the force.

A two-axis joint compliance model was used to indirectly estimate equivalent joint compliances in [2]. The data is gathered with a loaded double ball bar (LDBB) that applies a radial force and measures the radial displacement during a two-axis circular test at different force levels on a five-axis machine tool. Global and local compliances were calculated. The on-axis compliances were dominant in comparison with lateral and rotary ones. The disturbance from geometric errors in the radial displacement readings is removed by subtracting the readings from a low force test.

A new method for measuring the translational and rotational stiffness coefficients of a machine tool was introduced [3]. This method is based on rigid body motion and it allows any positioning of the displacements sensor and excitation force. It was able to recognize the reason for the appearance of differences in stiffness coefficient values on orthogonal directions of machine tool axes. The

measured stiffness between the tool and machine table including $k_x$, $k_y$, $k_z$ , $k_{\varphi x}$ and $k_{\varphi y}$ were approximately 2.02, 2.15, 16.7 $^{N}/_{\mu m}$, 0.212 and 0.211 $^{Nm}/_{\mu rad}$.

A novel measurement procedure was proposed to measure and determine the full Cartesian translational (volumetric) stiffness matrix for a 5-axis machine tool. Whilst the machine rotates its C-axis the X- and Y-axes nominally keep the tool ball at a constant position relative to the worktable which results in a circular path. The Loaded Double Ball Bar (LDBB) is used to apply various quasi-static loads between a workpiece ball attached to the table and a tool ball at the tool holder. The displacement of the tool ball relative to the table is measured by three Linearly Variable Differential Transformers (LVDT) [4].

A novel system that determines stationary machine tool quasi-static stiffness named Stiffness Workspace System (SWS) was introduced in [5]. This method can employ force with controlled value and direction and in the meanwhile measure the displacement using twelve inductive sensors. It was shown that the stiffness relies on both direction of employed force and position in the workspace.

The proposed approach in this paper to compliance measurement is to rely solely on force and position data obtained from the machine tool's encoder and drive current data.

## 6.3. Ball-Roller Bearing Device

The ball-roller bearing device (BRBD) consists of a spherical ball and a roller bearing, one attached to the work table and the other mounted in a tool holder a the spindle. The diameter of the ball is 50.8 mm, and its material is chrome steel. The type of roller bearing is NTN® (UC 206-103 D1) which is installed to an HSK A 63 MAXIN1-1/4X4.448 tool holder. The machine is programmed to follow a circular trajectory that moves the roller bearing around the ball. The trajectory radius is nominally smaller than the sum of the ball and roller bearing radii resulting in a reaction force due to the system's stiffness. Because the machine also has geometric errors, the actual trajectory that the machine aims to achieve will depart from a perfect circle thus causing a disturbance in the radial engagement. Radial volumetric stiffness estimation requires knowledge of the system deflection and the applied force. As conceptually shown in Figure 6.1, assuming the ball and roller bearing are rigid, the change in tooltip deflection is taken as the change in commanded engagement based on the encoder readings whereas the radial force is estimated from the drive currents also provided by the CNC.

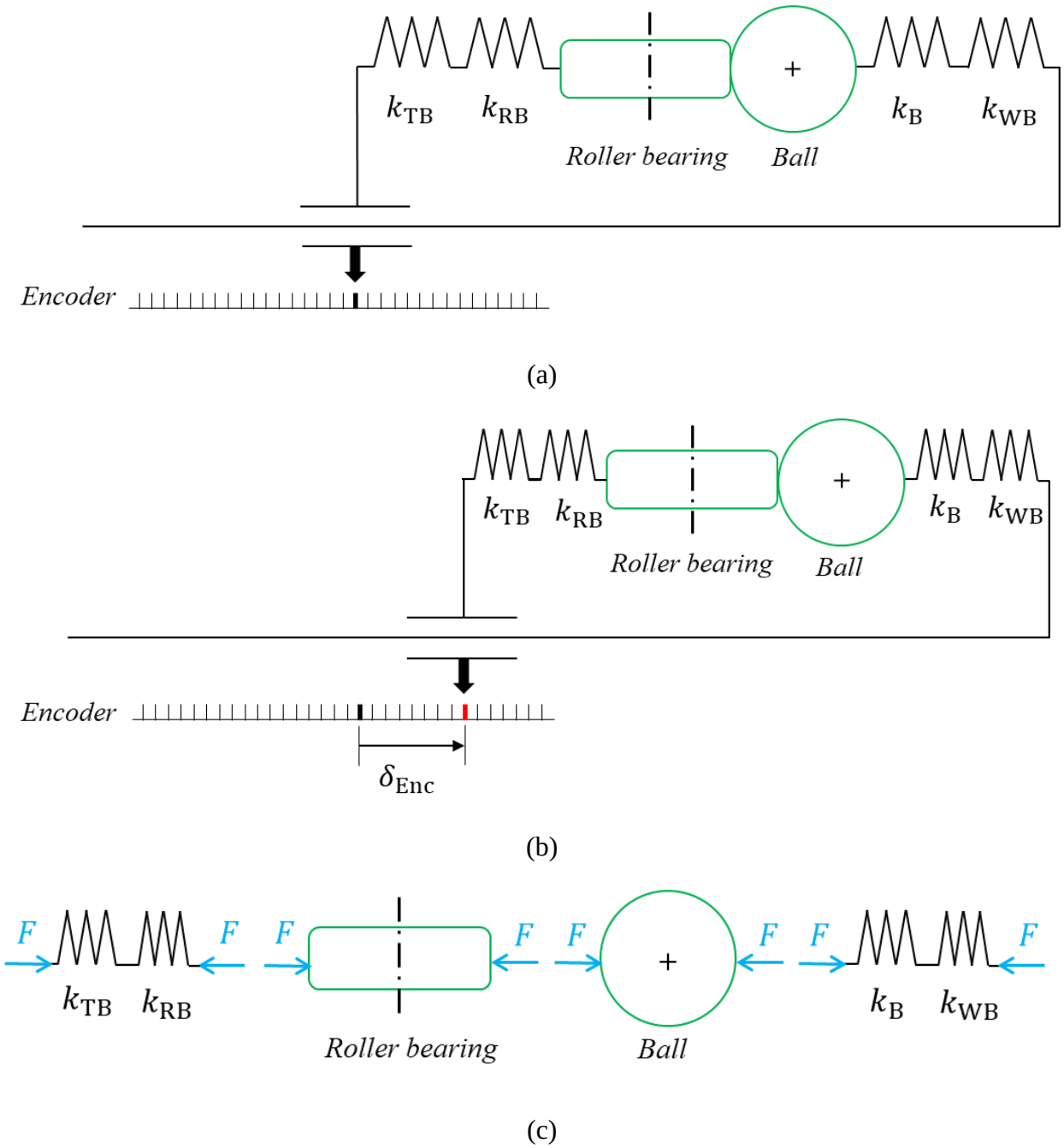


Figure 6.1. A schematic of BRBD and machine equivalent deflection. (a) Before commanding displacement. (b) After commanding displacement. (c) Free body diagram of BRBD. $k_{TB}$, $k_{WB}$, $k_{RB}$, $k_B$ and $\delta_{Enc}$ represents tool branch workpiece branch stiffness, roller bearing stiffness, ball stiffness, and encoder displacement, respectively.

Figure 6.2 shows the device unmounted and mounted on a five-axis machine tool.

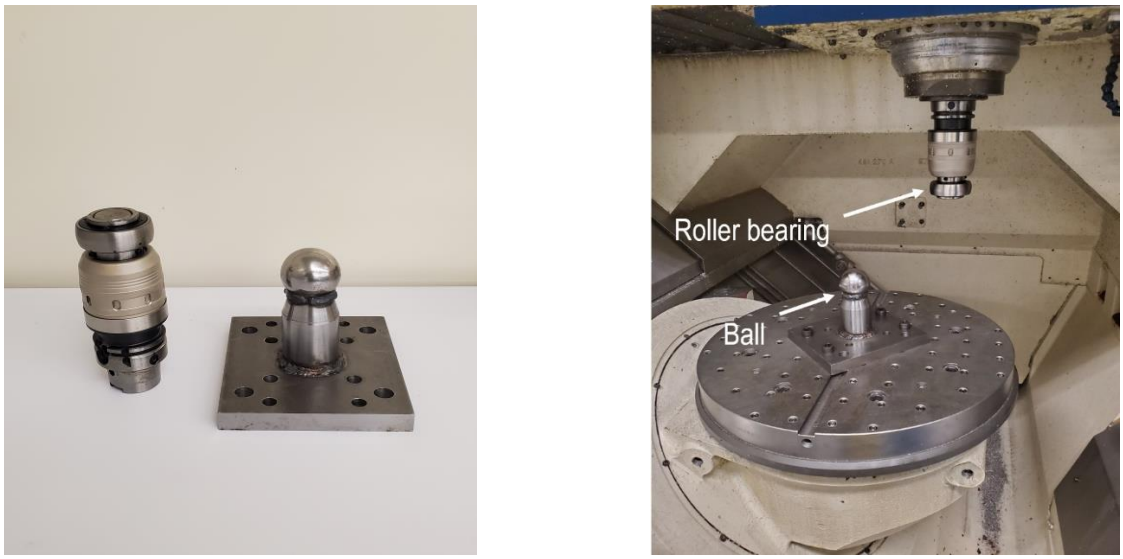


Figure 6.2. Photos of BRBD (left) mounted on a machine tool ready to test (right).

Figure 6.3 shows a 3D rendering of the tested 5-axis CNC machine with the topology wCAYfXZt and the BRBD system.

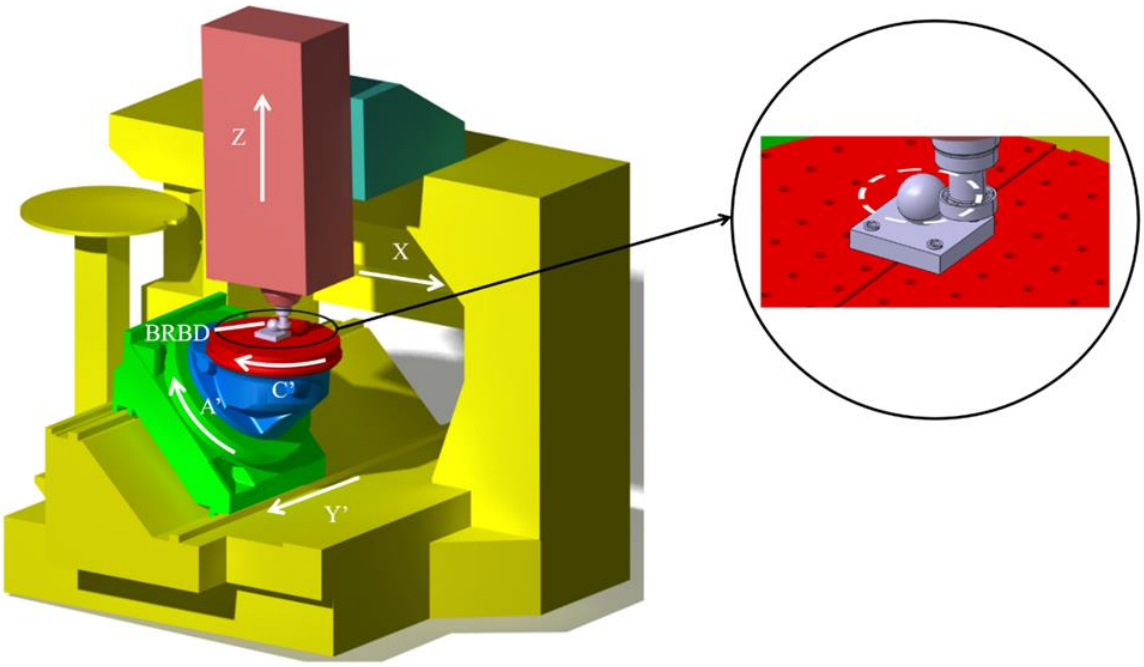


Figure 6.3. Huron KX8 five-axis vertical machine tool with BRBD mounted on it.

## 6.4. Volumetric stiffness model

As shown in Figure 6.1 The system is modeled as a series of springs. The commanded motion attempts to move the outer bearing surface into the ball. Neglecting Hertzian effects, no such penetration occurs and it is the entire system that must deflect to accommodate the axis motion as measured at the encoder level. As a result, the sum of the deflections within the system is assumed to equal the encoder indicated displacement

$$\delta_{\mathrm{Enc}} = \delta_{\mathrm{TB}} + \delta_{\mathrm{RB}} + \delta_{\mathrm{B}} + \delta_{\mathrm{WB}} \tag{6.1}$$

where $\delta_{\mathrm{Enc}}$, $\delta_{\mathrm{TB}}$, $\delta_{\mathrm{RB}}$, $\delta_{\mathrm{B}}$ and $\delta_{\mathrm{WB}}$ are the deflections of the tool branch, roller bearing, ball, and workpiece branch, respectively.

Using a Hooke's law model to the individual displacement yields

$$\delta_{\mathrm{Enc}} = \frac{F}{k_{\mathrm{TB}}} + \frac{F}{k_{\mathrm{RB}}} + \frac{F}{k_{\mathrm{B}}} + \frac{F}{k_{\mathrm{WB}}} \tag{6.2}$$

where $k_{\mathrm{TB}}$, $k_{\mathrm{RB}}$, $k_{\mathrm{B}}$ and $k_{\mathrm{WB}}$ are the tool branch, roller bearing, ball, and workpiece branch stiffness, respectively. Eq.(6.2) can be reformatted as follows to separate the machine stiffness and the setup stiffness from the BRBD device,

$$\begin{aligned} \frac{\delta_{\mathrm{Enc}}}{F} &= \left(\frac{1}{k_{\mathrm{TB}}} + \frac{1}{k_{\mathrm{WB}}}\right) + \left(\frac{1}{k_{\mathrm{RB}}} + \frac{1}{k_{\mathrm{B}}}\right) \\ &= \left(\frac{1}{k_{\mathrm{TB}}} + \frac{1}{k_{\mathrm{WB}}}\right) + \left(\frac{1}{k_{\mathrm{RB}}} + \frac{1}{k_{\mathrm{B}}}\right) \\ &= (C_{\mathrm{TB}} + C_{\mathrm{WB}}) + (C_{\mathrm{RB}} + C_{\mathrm{B}}) \end{aligned} \tag{6.3}$$

where the tool branch and workpiece branch stiffnesses and compliances are grouped together and similarly for the BRBD. Finally, the stiffness and compliance equations are presented with the machine and BRBD amalgamated terms as follows:

$$\frac{\delta_{\mathrm{Enc}}}{F} = \left(\frac{1}{k_{\mathrm{VM}}} + \frac{1}{k_{\mathrm{S}}}\right) = C_{\mathrm{VM}} + C_{\mathrm{S}} \tag{6.4}$$

where $k_{\mathrm{VM}}$, and $k_{\mathrm{S}}$ are the machine volumetric and BRBD (or setup) stiffnesses and $C_{\mathrm{VM}}$ and $C_{\mathrm{S}}$ are the corresponding compliances, respectively.

This model will be applied to all radial directions during a circular test. Also, because the machine and setup stiffness cannot be distinguished from the encoder and force data alone, a separate test will be conducted to estimate the setup stiffness.

### 6.4.1. Stiffness compensation

Machine volumetric stiffness is compensating for setup stiffness which affects machine stiffness. Eq.(6.5) is employed to compensate for the machine's volumetric stiffness. Hence, the compensation equation would be as follow

$$\frac{1}{k_{\mathrm{VM}}} = \frac{\delta_{\mathrm{Enc}}}{F} - \frac{1}{k_{\mathrm{S}}} \tag{6.5}$$

and

$$C_{\mathrm{VM}} = \frac{\delta_{\mathrm{Enc}}}{F} - C_{\mathrm{S}}$$

## 6.5. Machine feed drive torque model

The torque produced by the feed drive servomotor aims at rotating the ball screw but in doing so must overcome other torques such as the inertial acceleration torque, viscous friction torque, Coulomb friction torque, and disturbance torque from the useful load such as those due to cutting forces or in our case the interference between the roller bearing and the ball. Figure 6.4, demonstrates torque balance in the machine feed drive system during the BRBD test. A mathematical model which denotes this phenomenon in machine tool feed drive is as follows [6]:

$$k_{\mathrm{t}} i = \tau_{\mathrm{m}} = J_{\mathrm{T}} \frac{d\omega}{dt} + B_{\mathrm{T}}\omega + \tau_{\mathrm{c}}\,\mathrm{sgn}(\omega) + \tau_{\mathrm{d}} \tag{6.6}$$

where $k_{\mathrm{t}}$ , $i$ , $J_{\mathrm{T}}$ , $d\omega/dt$ , $B_{\mathrm{T}}$ , $\omega$ , $\tau_{\mathrm{c}}$ and $\tau_{\mathrm{d}}$ are the servomotor constant ($N\,m/A$), current ($A$), total inertia seen by the servomotor including bearings, ball screw, and slide ($kg\,m^2$), angular acceleration ($rad/s^2$), viscous coefficient ($N\,m\,s/rad$), angular velocity ($rad/s$), coulomb friction torque ($N\,m$) and disturbance torque caused by cutting force or BRBD interference ($N\,m$), respectively.

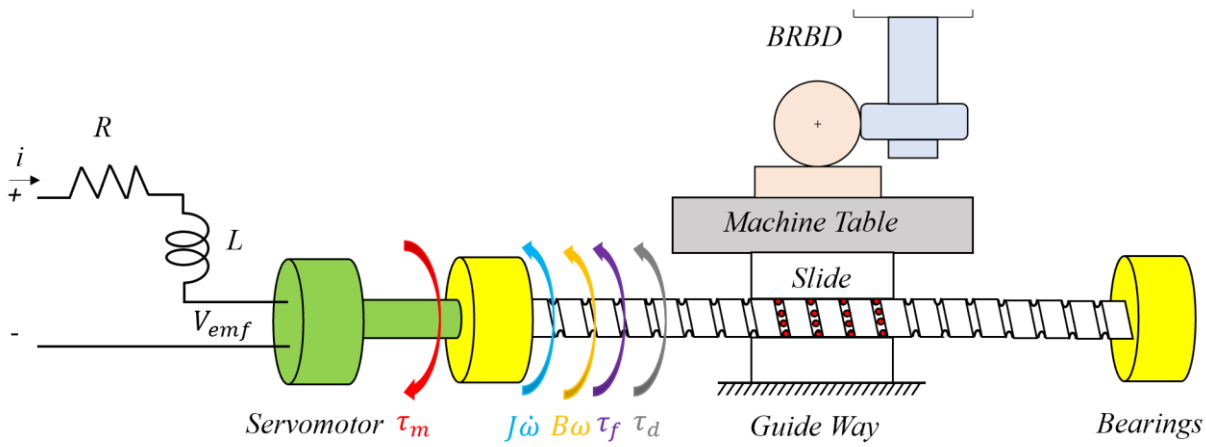


Figure 6.4. Schematics of applied torques through the machine tool feed drive during the BRBD test.

A mathematical model is applied to determine the unknown parameters including $J_T$ , $B_T$ , $\tau_f$ and $\tau_d$. The known parameters are $\dot{\omega}$ , $\omega$ and $i$ which are recorded through the machine controller for a different number of measurements. For machine X-axis feed drive:

$$\begin{bmatrix} \dot{\omega}_{1_X} & \omega_{1_X} & sgn(\omega_{1_X}) & \cos\theta_1 \\ \dot{\omega}_{2_X} & \omega_{2_X} & sgn(\omega_{2_X}) & \cos\theta_2 \\ \vdots & \vdots & \vdots & \vdots \\ \dot{\omega}_{n_X} & \omega_{n_X} & sgn(\omega_{n_X}) & \cos\theta_n \end{bmatrix} \begin{bmatrix} J_{T_X} \\ B_{T_X} \\ \tau_{f_X} \\ \tau_{d_X} \end{bmatrix} = \begin{bmatrix} \tau_{m_{1_X}} \\ \tau_{m_{2_X}} \\ \vdots \\ \tau_{m_{n_X}} \end{bmatrix} = \begin{bmatrix} k_{t_X} i_{1_X} \\ k_{t_X} i_{2_X} \\ \vdots \\ k_{t_X} i_{n_X} \end{bmatrix} \tag{6.7}$$

By employing the same model to the machine Y-axis feed drive:

$$\begin{bmatrix} \dot{\omega}_{1_Y} & \omega_{1_Y} & sgn(\omega_{1_Y}) & \sin\theta_1 \\ \dot{\omega}_{2_Y} & \omega_{2_Y} & sgn(\omega_{2_Y}) & \sin\theta_2 \\ \vdots & \vdots & \vdots & \vdots \\ \dot{\omega}_{n_Y} & \omega_{n_Y} & sgn(\omega_{n_Y}) & \sin\theta_n \end{bmatrix} \begin{bmatrix} J_{T_Y} \\ B_{T_Y} \\ \tau_{f_Y} \\ \tau_{d_Y} \end{bmatrix} = \begin{bmatrix} \tau_{m_{1_Y}} \\ \tau_{m_{2_Y}} \\ \vdots \\ \tau_{m_{n_Y}} \end{bmatrix} = \begin{bmatrix} k_{t_Y} i_{1_Y} \\ k_{t_Y} i_{2_Y} \\ \vdots \\ k_{t_Y} i_{n_Y} \end{bmatrix} \tag{6.8}$$

By naming matrices in *(6.7* from left to right as *S*, *v*, and *r*:

$$Sv = r \tag{6.9}$$

$$S^T S v = S^T r$$

$$v = (S^T S)^{-1} S^T r$$

By considering (6.9) the unknown parameters ($v$) can be estimated by using the known parameters ($S$) where the machine controller provides them.

The motor constant $k_t$ for machine X and Y-axis are listed in Table 6.1.

Table 6.1. Table 6.2. Motor constant value for X and Y feed drive axis [7].

| Axis | $k_t[^{N\,m}/_{A}]$ |
|---|---|
| X | 1.65 |
| Y | 1.52 |

To convert disturbance torque is converted to the disturbance force using feed drive system characteristics [6]:

$$F_d = \frac{\eta}{r_g}\,\tau_d \tag{6.10}$$

where $\eta$ and $r_g$ are the efficiency and transmission ratio of the ball screw, respectively. The relationship between the pitch and transmission ratio of the ball screw is as follows [6]:

$$r_g = \frac{h}{2\pi} \tag{6.11}$$

where h is the pitch of the screw. Table 6.3 lists the pitch, transmission ratio and efficiency values of the machine axes feed drive.

Table 6.3. Pitch, transmission ratio and efficiency values of machine axes feed drive [7].

| Axis | Pitch, h ($^{mm}/_{rev}$) | Transmission ratio, $r_g$ ($^{mm}/_{rad}$) | Efficiency, $\eta$ (%) |
|---|---|---|---|
| X | 10 | 1.59 | 90 |
| Y | 10 | 1.59 | 90 |

Table 6.4 represents the estimated parameters for the machine X and Y feed drive axis.

Table 6.4. Estimated parameters value ($v$) for machine X and Y feed drive axis

| Axis | $J_T[kgm^2]$ | $B_T\ [^{N\ m\ s}/_{rad}]$ | $\tau_c[Nm]$ | $\tau_d\ [Nm]$ |
|---|---|---|---|---|
| X | 0.006 | 0.09 | 1.55 | 2.64 |
| Y | 0.004 | 0.07 | 1.60 | 2.59 |

Figure 6.5 represents the estimated inertial, viscous, coulomb, and disturbance force for the maximum displacement of 200 µm.

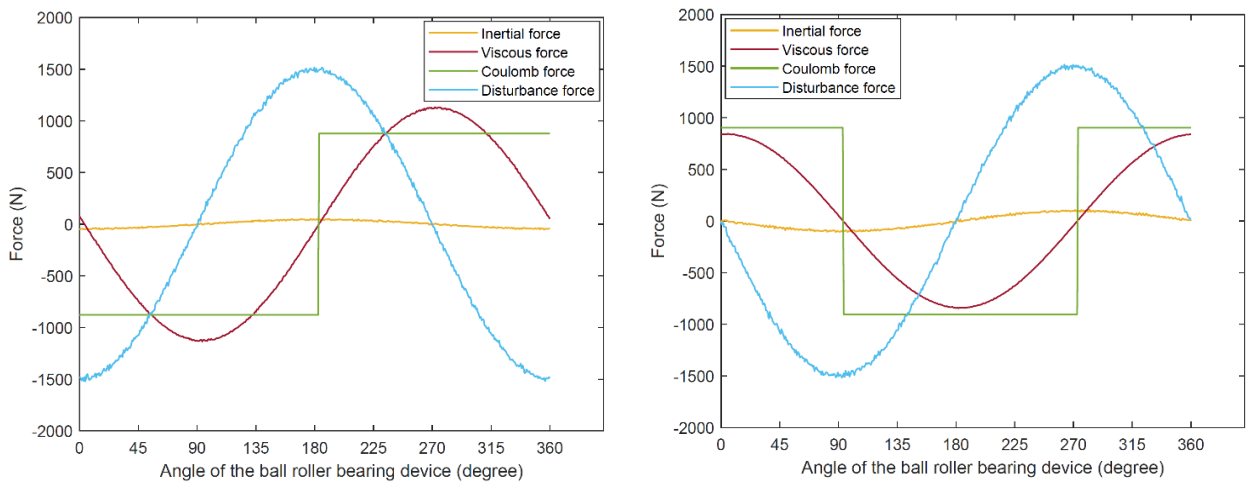


(a) (b)

Figure 6.5. Estimated inertial, viscous, coulomb, and disturbance force for the maximum displacement of 200 µm. (a) X-axis. (b) Y-axis.

### 6.5.1. Propagation of force from feed drive (joint) space to the tooltip (cartesian) space

Based on the virtual work theory, the works that have been done in the joint space and tooltip space should be equal. From another perspective, the displacement at the tooltip due to the applied force would cause displacement at the joint. By the knowledge of joint and tooltip relationship in terms of displacement and virtual work [8]:

$$d\boldsymbol{W} = \boldsymbol{\tau}^{\mathrm{T}} d\boldsymbol{j} - \boldsymbol{F}^{\mathrm{T}} d\boldsymbol{t} \tag{6.12}$$

where $dW$, $\tau^{\mathrm{T}}$, $dj$ , $F^{\mathrm{T}}$, $dt$ is the virtual work, transpose of torque at the joint, joint displacement, transpose of force at the tool, and displacement at the tool, respectively.

The association of the joint and tooltip displacement is [8]:

$$d\boldsymbol{t} = \boldsymbol{J} d\boldsymbol{j} \tag{6.13}$$

By substituting Eq.(6.13) in Eq.(6.12) [8]:

$$d\boldsymbol{W} = (\boldsymbol{\tau} - \boldsymbol{J}^{\mathrm{T}} \boldsymbol{F})^{\mathrm{T}} d\boldsymbol{j} \tag{6.14}$$

Considering the static equilibrium, which states that the total virtual work should be zero [8], in Eq.(6.14):

$$\boldsymbol{\tau} = \boldsymbol{J}^{\mathrm{T}} \boldsymbol{F} \tag{6.15}$$

## 6.6. Experimental validation

### 6.6.1. Current based force validation with dynamometer table

The force prediction from the servomotor current is validated using a dynamometer table as shown in Figure 6.6. Five nominal test radii (40, 80, 120, 160, and 200 µm) are commanded for the relative circular trajectory of the roller bearing around the ball and the results are shown in Figure 6.7.

Figure 6.6. Installed dynamometer table and BRBD device on the machine tool.

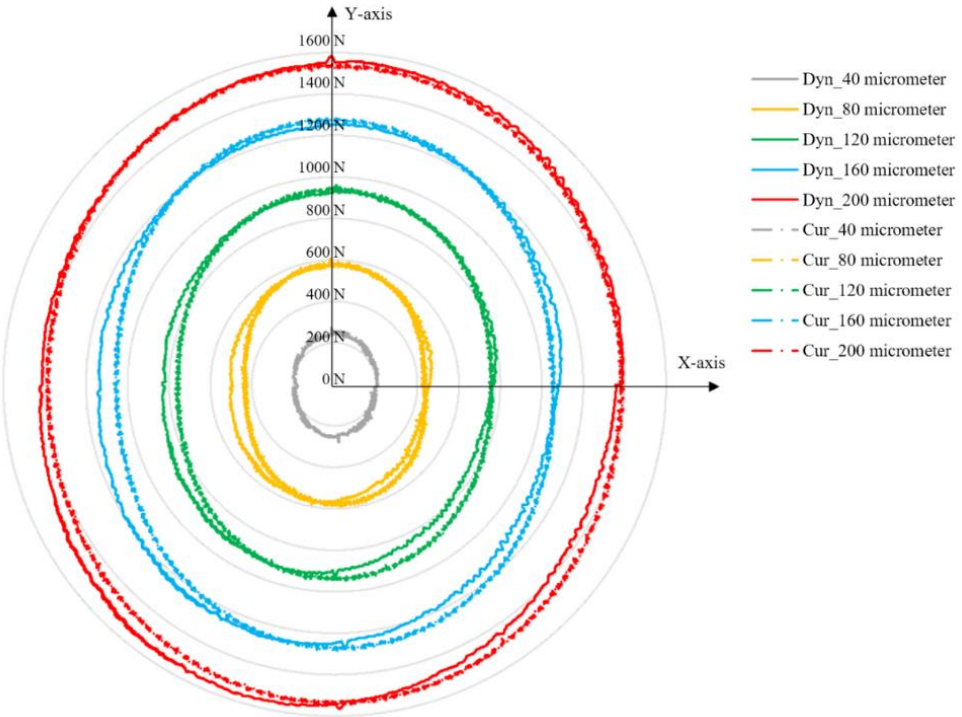


Figure 6.7. Comparison of dynamometer measured force (Dyn) and current-based force (Cur) for different commanded displacements with 1000 mm/min feed rate.

### 6.6.2. Setup stiffness measurement

The volumetric stiffness includes the setup deflection and since it has an important effect on the machine volumetric stiffness, it needs to be determined and subtract from the nominal commanded displacement. As shown in Figure 6.8 the setup stiffness is determined by a single X-axis test in which the roller bearing moves with a feed rate of 1000 mm/min at the X- direction towards the ball. The encoder is commanded by the nominal displacements including 40, 80, 120, 160, and 200 µm, and the ball, as well as roller bearing resultant deflections, are measured by dial indicators which are installed on the spindle and work table, respectively. Figure 6.8 represents dial indicator readings including ball, roller bearing, and machine deflection as a function of encoder commanded displacement.

Figure 6.8. Set up stiffness measurement with the dial indicator at X-direction and 1000 mm/min feed rate.

Table 6.4 represents setup deflection including ball and roller bearing deflection. According to Table 6.4, it can be seen that at the highest commanded displacement (200 µm), approximately 55% and 45% of volumetric stiffness comes from machine and setup, respectively. Eq.(6.8) is used for the stiffness compensation in which setup stiffness is subtracted from the encoder stiffness and the retained one is the stiffness which comes from the machine.

Table 6.5. Measured setup (ball and roller-bearing) deflection in a single X_axis test.

| **Commanded displacement (µm)** | **Ball deflection (µm)** | **Roller-bearing deflection (µm)** | **Total setup deflection (µm)** | **Machine deflection (µm)** |
|---|---|---|---|---|
| **40** | 0 | 10 | 10 | 30 |
| **80** | 0 | 26 | 26 | 54 |
| **120** | 2 | 44 | 46 | 74 |
| **160** | 2 | 64 | 66 | 94 |
| **200** | 3 | 86 | 89 | 111 |

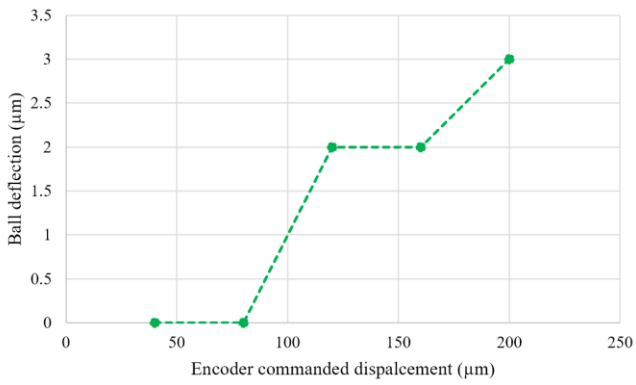


(a)

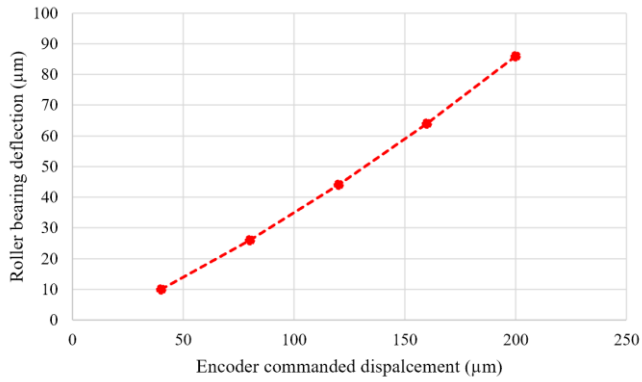


(b)

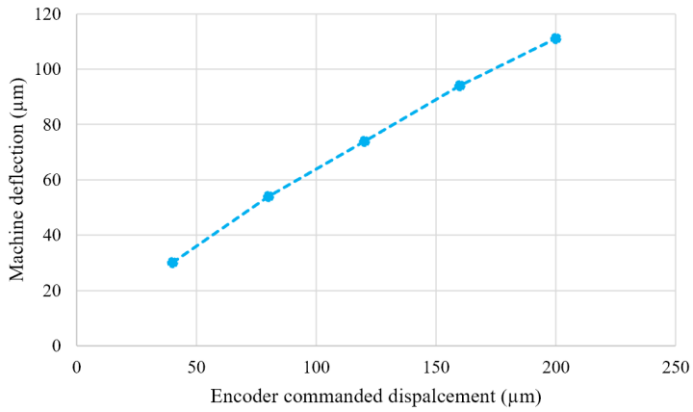


(c)

Figure 6.9. Dial indicator readings as a function of encoder commanded displacement. (a) Ball deflection. (b) Roller bearing deflection. (c) Machine deflection.

Table 6.6 illustrates the measured ball, roller-bearing, and machine stiffness in a single X_axis test.

Table 6.6. Measured ball, roller-bearing, and machine stiffness in a single X_axis test.

| **Commanded displacement (μm)** | **Ball stiffness ($k_B$) ($N/\mu m$)** | **Roller-bearing stiffness ($k_{RB}$) ($N/\mu m$)** | **Total setup stiffness ($k_S$) ($N/\mu m$)** | **Machine stiffness ($k_{VM}$) ($N/\mu m$)** |
|---|---|---|---|---|
| **40** | inf | 18.9 | 18.9 | 6.3 |
| **80** | inf | 17.3 | 17.3 | 8.3 |
| **120** | 375 | 17 | 16.3 | 10.1 |
| **160** | 523.5 | 16.3 | 15.8 | 11.1 |
| **200** | 430.3 | 15 | 14.5 | 11.6 |

Eq.(6.5) is used to calculate machine volumetric stiffness. The volumetric stiffness of the machine ($k_{VM}$) is illustrated in Figure 6.10. As shown in Figure 6.10, by increasing the commanded displacement, the stiffness value is increasing.

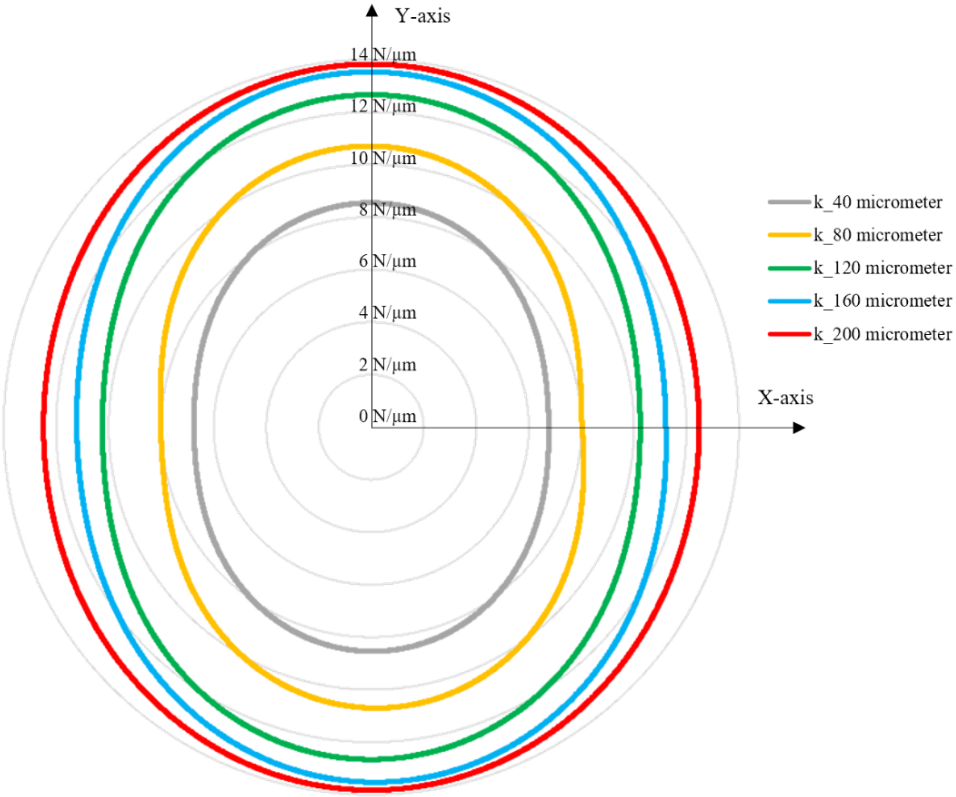


Figure 6.10. Compensated volumetric stiffness ($k_{\mathrm{VM}}$) for various commanded displacements (40, 80, 120, 160 and 200 µm).

### 6.6.3. Stiffness validation with compliant part (rig)

Figure 6.8(a) shows a compliant rig mounted on the machine table to induce an apparent change in the machine volumetric compliance. This device uses a parallelogram flexure mechanism. It has a rigid upper part connected through two thin and flexible plates to a rigid lower part. As shown in Figure 6.11, the stiffness of the rig is 2.65 $N/\mu m$ which was measured by adding certain weight (11.89, 24.97, 31.90, 56.85, 68.75, 79.77, 91.66, 104.74, and 111.68 N) and measuring the displacement.

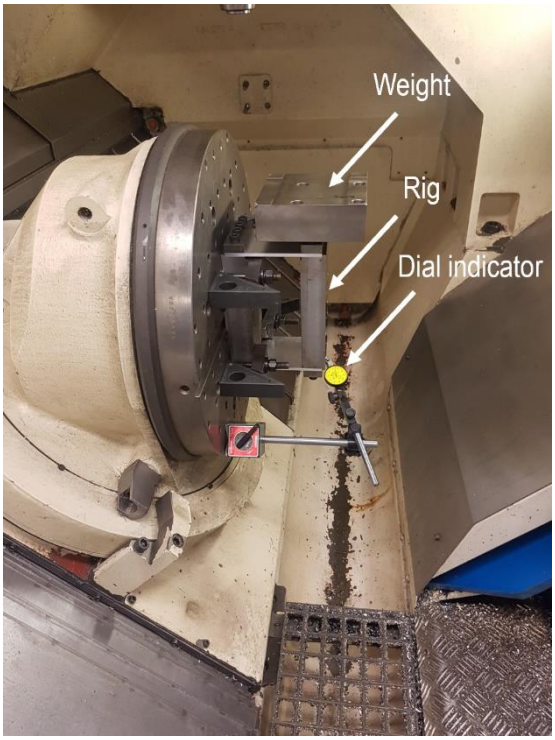


Figure 6.11. Measuring the stiffness of the rig by adding certain weights (11.89, 24.97, 31.90, 56.85, 68.75, 79.77, 91.66, 104.74, and 111.68 N) and measuring the displacement by a dial indicator.

The added rig is like another spring added in series to the existing setup the following equation applies:

$$\frac{1}{k_{\mathrm{VMwr}}} = C_{\mathrm{VMwr}} = \frac{1}{k_{\mathrm{VM}}} + \frac{1}{k_{\mathrm{r}}} = C_{\mathrm{VM}} + C_{\mathrm{r}} \tag{6.16}$$

where $k_{\mathrm{VMwr}}$, $k_{\mathrm{VM}}$ and $k_{\mathrm{r}}$ are machine volumetric with the rig, without the rig, and rig stiffness. $C_{\mathrm{VM}}$ and $C_{\mathrm{S}}$ are the corresponding compliances, respectively. Based on Eq.(6.16), the summation of the inverse of stiffness without the rig and the rig itself are equal to the inverse of stiffness with the rig. Figure 6.12 represents stiffness validation setup with BRBD, rig, and dynamometer table. Figure 6.12 (a) and Figure 6.12 (b) show setup without and with the rig, respectively.

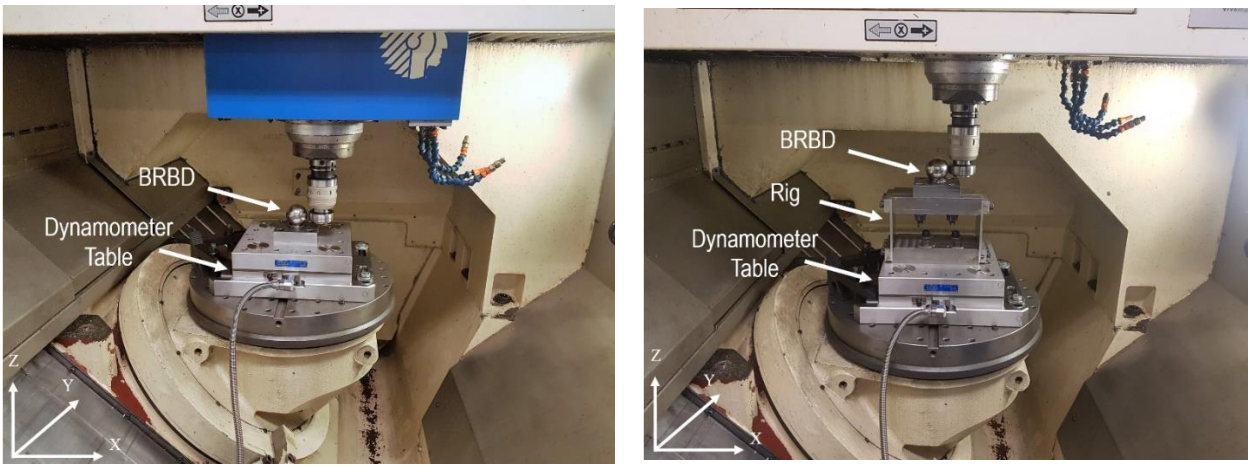


(a) (b)

Figure 6.12. Stiffness validation setup with BRBD, rig, and dynamometer table. (a) setup without the rig. (b) setup with the rig.

As shown in Figure 6.13 (a) and Figure 6.13 (b) by adding a rig to the setup, stiffness values are changed. As shown in Figure 6.13 (a), for the highest commanded displacement, the stiffness value is decreased from 12.5 and 14 $^{N}/_{\mu m}$ to 3.34 and 9.65 $^{N}/_{\mu m}$ in X- and Y-direction, respectively.

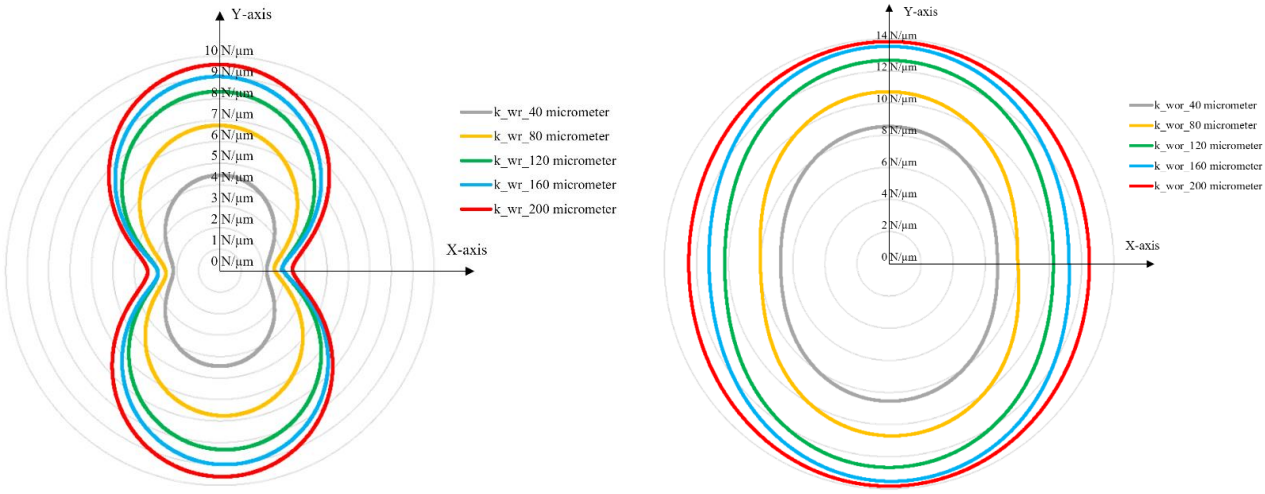


(a) (b)

Figure 6.13. Stiffness variation for different commanded displacements. (a) setup with the rig. (b) setup without the rig.

Figure 6.14 depicts the change in machine volumetric compliance without a rig, with the rig, and predicted with the rig, respectively. For a system in series spring, the compliance values simply add to each other, therefore the rig compliance value (0.37 µm/N) is added to the machine volumetric compliance value without a rig. For example, machine volumetric compliance for 40 µm displacement in X-direction is 0.07 µm/N and by using Eq.(6.16), the machine volumetric compliance with the rig is predicted to be 0.5325 µm/N whereas the obtained machine volumetric compliance is 0.5194 µm/N.

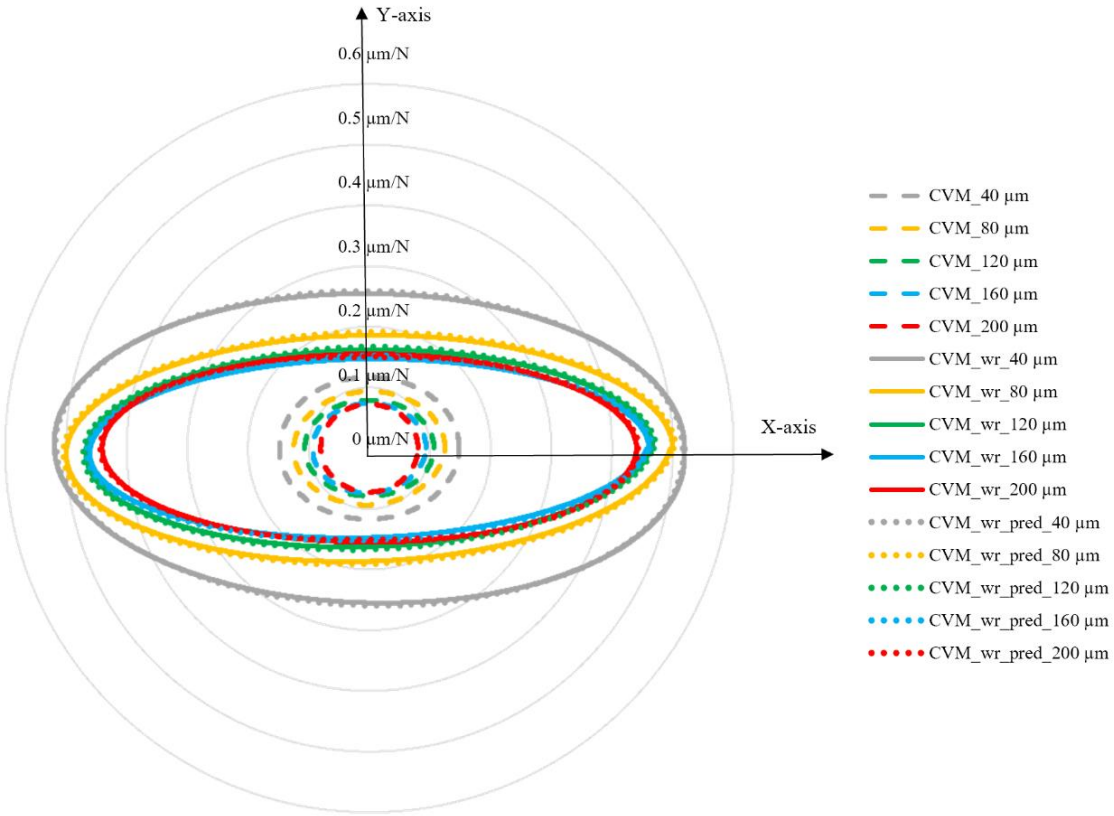


Figure 6.14. Machine volumetric compliance without a rig, with the rig, and predicted with rig for different commanded displacements. CVM, CVM_wr, and CVM_wr_pred represent machine volumetric compliance without a rig, with the rig, and predicted with the rig.

## 6.7. Conclusion

To estimate the machine tool volumetric stiffness, a new Ball-Roller Bearing Device is used. The joint force and displacement are obtained through the servo motor current and the encoder reading without any external loading device, load cell, or displacement sensor. It is observed that, by increasing the commanded displacement, the stiffness value is increased. It is shown that at the highest displacement, approximately 55% and 45% of volumetric stiffness comes from machine and setup, respectively.

## 6.8. References


1. International Organization for Standardization, *ISO 230-1, Test code for machine tools — part 1: Geometric accuracy of machines operating under no-load or quasi-static conditions*. 2012.

2. Beglarzadeh, B., J.R.R. Mayer, and A. Archenti, *Modelling and indirect measurement of machine tool equivalent joint compliances.* CIRP Journal of Manufacturing Science and Technology, 2021. 35: p. 882-895.

3. Majda, P. and J. Jastrzębska, *Measurement uncertainty of generalized stiffness of machine tools.* Measurement, 2021. 170.

4. Laspas, T., N. Theissen, and A. Archenti, *Novel methodology for the measurement and identification for quasi-static stiffness of five-axis machine tools.* Precision Engineering, 2020. 65: p. 164-170.

5. Pawełko, P., et al., *A new measurement system to determine stiffness distribution in machine tool workspace.* Archives of Civil and Mechanical Engineering, 2021. 21(2).

6. Aslan, D. and Y. Altintas, *Prediction of Cutting Forces in Five-Axis Milling Using Feed Drive Current Measurements.* IEEE/ASME Transactions on Mechatronics, 2018. 23(2): p. 833-844.

7. *Simodrive 611 / Masterdrives mc / 1FT6 synchronous motors*. 2005, Siemens.

8. H Asada and JJE Slotine, *Robot analysis, and control*. 1986, New York: Wiley.

# CHAPTER 7 GENERAL DISCUSSION

A general discussion of the thesis is presented in this chapter. The principal methods, as well as procedures that have been used, are presented within the context of the machine tool compliance characterization.

Machine tool stiffness plays an important role in the machining process outcome. The significant elements in designing high precision machines are recognizing error sources, their cause, and their contribution to the machined part deviation. Stiffness participates in the alteration of precision in the machining process. The stiffness of machine tools changes with position and direction since the machine may distort under cutting forces and workpiece weight. Machine stiffness also affects the dynamic stability of the machine. Machine maintenance is greatly facilitated if problems can be detected early on and diagnosed to avoid making bad parts and production loss due to unexpected machine breakdown. Information regarding the machine tool stiffness can be obtained from simulation (finite element analysis), and analytical methods but these are based on a nominal machine, not the actual one on the shop floor.

In this thesis, a novel joint compliance model was developed which was indirectly estimated using different levels of volumetric radial load and displacement data obtained via the Loaded Double Ball Bar (LDBB) test. Simulations and close inspection of the numerical Jacobian matrix suggested the presence of significant confounding between compliances of the X- and Y-axis. This was partly due to the nature of the test which did not allow, for example, to differentiate between the effect of on-axis compliance at the X-axis, $C_{\mathrm{XXX}}$, and lateral compliance at the Y-axis, $C_{\mathrm{XXY}}$. A similar confounding occurred between the on-axis compliance of the Y-axis $C_{\mathrm{YYY}}$ and the lateral compliance of the X-axis $C_{\mathrm{YYX}}$. The loaded telescopic double ball-bar test was conducted at seven force levels of 36, 112, 238, 364, 490, 616, and 742 N. When using all available data, the dominant estimated global compliance terms were $C_{\mathrm{XXX}}$ and $C_{\mathrm{YYY}}$ at 7.61E-05 and 6.05E-05 mm/N. These dominant compliances gradually increase with the load by approximately 5% over the tested load range, which was unexpected. $C_{\mathrm{XYX}}$ also increased, others decreased such as $C_{\mathrm{CXY}}$ and $C_{\mathrm{CYY}}$. The compliance term $C_{\mathrm{CCY}}$ results in a four-lobed trace, as demonstrated by simulations, which had not been associated with unloaded ball bar circular tests. However, its estimated value was always negative which is physically unexpected. Its contribution to the deflection was estimated at one-thousandth that of the main compliance term and about one-third of the resolution of the LDBB position readout so its value was too small to be relied upon for the tested machine. This indirect method, which estimates model

parameters from the volumetric effect of many contributors, is attractive by its simplicity and automation potential, especially for use as a regular checkup of a machine in an industrial setting. It also allows, given sufficiently rich tests to be determined, to separate the contribution compliance to guide repairs. The same model could then also be used to predict deflection under different conditions such as when machining.

The LDBB test involves significant motion of the machine axes and so is partly contaminated with the volumetric effect of the machine tool geometric errors. In order to make a better use of the data, an elasto-geometric model was developed that was contextualized to the data gathered during a loaded 2D circular test implemented using a loaded double ball bar (LDBB) to simultaneously estimate the machine tool X- and Y-axis equivalent compliances and their geometric errors. The compliances were said to be "equivalent" because although only two axes are mobile during the test, the machine has five axes, and all axes may contribute to the observed volumetric deflections. The tests were executed using seven levels of forces of 36, 112, 238, 364, 490, 616, and 742 N. At lower forces the geometric errors were dominant whilst at higher forces compliance errors dominated. When using all data to build a single geometry and compliance set of parameters (global constant compliance model) the radial volumetric variations due to geometric errors and compliance were estimated at 0.019 mm and 0.046 mm, respectively, making compliance dominant by more than three times. The impact of dominant and non-dominant equivalent global compliance $C_{\mathrm{XXX}}$, $C_{\mathrm{YYY}}$, $C_{\mathrm{XYX}}$, $C_{\mathrm{CXY}}$, $C_{\mathrm{CYY}}$ and $C_{\mathrm{CCY}}$ on the loaded circular test readings at the highest force level of 742 N were predicted to be around 0.045, 0.034, 0.00058, 0.0022, 0.0014, and 0.0045 mm peak-to-peak, respectively. The impact of loaded geometric parameter $E_{\mathrm{XX1}}$, $E_{\mathrm{YY1}}$, $E_{\mathrm{YX2}}$, $E_{\mathrm{XY2}}$, $E_{\mathrm{C(0Y)X}}$, $E_{\mathrm{Xt0}}$ and $E_{\mathrm{Yt0}}$ on the loaded circular test readings were predicted to be around 0.019, 0.014, 0.0074, 0.012, 0.00017, 0.0076 and 0.0012 mm peak-to-peak, respectively. The dominant global compliances were $C_{\mathrm{XXX}}$ and $C_{\mathrm{YYY}}$ at 0.0619 and 0.0461 $\mu\mathrm{m/N}$, respectively.

By feeding the elasto-geometric model with pairs of adjacent force data the evolution of compliance with changes in the applied force was observed. Although theoretically unexpected, the estimated geometry changed with force levels. The radial volumetric largest change due to variation in the estimated geometry across the range of tested forces (local model) amounted to 0.0085 mm whereas the global model radial volumetric effects due to geometric errors were estimated at 0.019 mm. This means that the estimated change in geometry was significant. As the geometric errors would not change for different force levels, it pointed to the need to enrich the compliance model so that it could better explain the change in the machine behavior across the tested force range. As the force increased

the majority of compliance terms increased such as $C_{\mathrm{XXX}}$, $C_{\mathrm{XYX}}$, $C_{\mathrm{YYY}}$ and $C_{\mathrm{CCY}}$. Two of the less significant compliances, $C_{\mathrm{CXY}}$ and $C_{\mathrm{CYY}}$, showed no clear trends. Most of the loaded geometric terms decreased such as $E_{\mathrm{XX1}}$, $E_{\mathrm{YY1}}$, $E_{\mathrm{C(0Y)X}}$, $E_{\mathrm{Xt0}}$ and $E_{\mathrm{Yt0}}$ as the force increased but $E_{\mathrm{YX2}}$ and $E_{\mathrm{XY2}}$ increased. The change in local compliance suggested that the compliance may vary with the applied force. As the compliance was assumed to be constant this may be causing the apparent change in the geometric error parameters at different force levels. Consequently, the compliance model was enriched as a linear function of the applied force to process all force level data at once so that the estimated geometry is kept the same at all force levels. The root mean square error (RMSE) value for predicting the radial LDBB readings using the constant and linearly variable compliance models were 0.0011 and 0.0009 mm, respectively, for an improvement of about 18% using the variable compliance model. As all models predicted over 91% of the experimental radial deviations, the use of a linear compliance model resulted in just over 1% fitting improvement.

Finally, the novel loading test apparatus, the so-called Ball-Roller Bearing Device (BRBD) was introduced. The machine volumetric stiffness was examined by this device. The force and engagement were calculated from the servo motor current and the encoder readings, respectively. It was observed that while the force level is increased, the stiffness value also increased. It was shown that at the highest displacement, approximately 55% and 45% of volumetric stiffness came from the machine and BRBD device, respectively. A known compliance part namely the compliant rig was used to validate the measured volumetric compliance. It was shown that the combined rig and machine compliance could be closely estimated by a BRBD test.

# CHAPTER 8 CONCLUSION AND RECOMMENDATION

This chapter summarises the findings of the research reported in chapters 4 to 6, as well as the recommendations for further work.

## 8.1. Conclusion and contributions of the work

The thesis covers the indirect estimation of machine tool compliance only, followed by the concurrent estimation of compliance and geometric error parameters, from volumetric data. A matrix formulation of the forward force to deflection compliance model of the serial mechanism is used to generate the numerical Jacobian of the change in the loaded double ball bar (LDBB) length as a function of the machine joint compliances and the applied forces. The characteristic patterns of loaded telescopic double ball bar readings associated with each compliance term are also generated. The compliance model contained numerous superfluous and confounded terms that were pruned from the model. The model was then used to estimate the compliances from test data gathered at various force levels. By using all force data at once global compliance values were estimated whereas using only adjacent force level data allows observing the change in compliance with force. The dominant compliances were the X-axis on-axis compliance $C_{\mathrm{XXX}}$ (confounded with the lateral compliance of the Y-axis $C_{\mathrm{XXY}}$) and $C_{\mathrm{YYY}}$ (confounded with $C_{\mathrm{YYX}}$). It was observed that as the load increased the dominant compliances also increased.

In the initial model, the geometric error effects on the LDBB reading were removed by subtracting the low force level reading from all the data. As an alternative approach, a so-called elasto-geometric model was introduced. An elasto-geometric model used the principle of superposition to separate the effects of joint compliance and geometric errors. The model parameters were estimated from tests at different force levels, by distinguishing between errors that change with the applied force (compliance effect) from those that do not (geometric effects). At lower forces, the geometric errors were dominant whilst at higher forces compliance-induced errors dominated. When using all data to build a single geometry and compliance set of parameters the maximum effect of compliance was three times as much as for the geometric effects. By feeding the elasto-geometric model with pairs of adjacent force data the evolution of estimated equivalent compliance parameters and geometric errors with changes in the applied force were observed. Although theoretically unexpected, the estimated geometry significantly changed across the force range. The change in estimated geometry predicted radial effect changes that was nearly half of the global geometric effect. As the force increased the majority of

equivalent compliance terms increased such as the dominant equivalent compliances $C_{\mathrm{XXX}}$ and $C_{\mathrm{YYY}}$ as well as the less significant compliances $C_{\mathrm{XYX}}$ and $C_{\mathrm{CCY}}$. As for $C_{\mathrm{CXY}}$ and $C_{\mathrm{CYY}}$ no clear trend was observed. Given this observed dependence of the compliance on the force level, the compliance was further modeled as a linear function of the applied force thus further improving the model prediction while keeping geometric errors constant independently of the load level.

Lastly, a loading test instrument so-called Ball-Roller Bearing Device (BRBD) was used to determine the machine's volumetric stiffness without added force device or sensors. The machine was loaded with the BRBD by commanding a displacement, while servo motor current and encoder readings were recorded. The force was calculated from the current. It was seen that while the force level was increased, the stiffness value also was increased. Because the added BRBD device compliance is significant it was separately estimated, and the results were compensated. For validation purposes, a known compliance part (rig) was added to the machine table. The BRBD result exposed that the summation of the rig compliance and machine volumetric compliance was very close to the machine volumetric compliance value when it was tested with the rig.

Executed compliance and elasto-geometric models together with novel loading apparatus were given an overall picture of machine compliance in which both joint and volumetric compliance were examined in detail. The machine tool can be loaded with BRBD, and machine volumetric compliance can be calculated. Furthermore, the recorded data during the BRBD test can be fed to the elasto-geometric estimator to estimate the relevant joint compliance and geometric parameters.

## 8.2. Recommendations for future works

The aforementioned models and loading instruments can be further improved. The compliances are said to be “equivalent” because although only two axes are mobile during the test, the machine has five axes, and all axes may contribute to the observed volumetric deflections. Richer LDBB tests involving more axes of the machine are needed to quantify more compliances.

Machine maintenance is greatly facilitated if problems can be detected early on and diagnosed to avoid production loss due to unexpected machine breakdown. Hence, an online stiffness monitoring software can be introduced which can be quite beneficial to predict upcoming failures.

Based on the local compliance analysis in both compliance and elasto-geometric models, the machine tool compliance presented non-linear behavior. Both compliance and elasto-geometric models can be enriched with non-linear functions. In this case, the models can better explain the non-linearity of compliance and its behavior can be examined from lower to higher levels of forces.

Machine stiffness can be affected by high-speed machining. Therefore, a new approach will be needed to investigate the correlation between machine stiffness and speed. While the machine is changing its speed from lower to a higher value, the machine stiffness can change from steady-state to transit status from which another factor can emerge.

The machine tool may distort under workpiece weight which is important for accurate machining. Consequently, in the analysis of machine overall stiffness, an innovative testing method will be required to stimulate the workpiece weight while the machine is moving. In such circumstances, both cutting forces as a loaded criterion and workpiece weight contributions in machine total stiffness can be examined.

# REFERENCES


Aachen, W. R. (2018). Static and dynamic flexibility behaviour of machine tools. Retrieved from https://www.wzl.rwthaachen.de/cms/www_content/en/9ca627d9a8ad2da3c1256fb2004537f7.htm

Agapiou, J. S. (2008). Estimating the Static Stiffness for a Spindle-Toolholder-Tooling System. *Machining Science and Technology, 12*(1), 77-99. doi:10.1080/10910340801890938

Agaplou, J. S. (2005). A Methodology to Measure Joint Stiffness Parameters for Toolholder-Spindle Interfaces. *Journal of Manufacturing Systems, 24*(1), 13-20.

Andreas Archenti, M. N., Guillame Casterman, Sven Hjelm. (2012). A New Method for Circular Testing of Machine Tools Under Loaded Condition. *5th CIRP Conference on High Performance Cutting 2012, 1*, 575-580. doi:10.1016/j.procir.2012.04.102

Archenti, A. (2011). *A Computational Framework for Control of Machining System Capability : From Formulation to Implementation.* (PhD). KTH Royal Institute of Technology, Stockholm, Sweden.

Archenti, A. (2014). Prediction of machined part accuracy from machining system capability. *CIRP Annals, 63*(1), 505-508. doi:10.1016/j.cirp.2014.03.040

Archenti, A., & Laspas, T. (2019). Accuracy and Performance Analysis of Machine Tools. In W. Gao (Ed.), *Metrology* (pp. 215-244). Singapore: Springer Singapore.

Archenti, A., & Nicolescu, M. (2013). Accuracy analysis of machine tools using Elastically Linked Systems. *Cirp Annals-Manufacturing Technology, 62*(1), 503-506. doi:10.1016/j.cirp.2013.03.100

Archenti, A., & Nicolescu, M. (2013). Accuracy analysis of machine tools using Elastically Linked Systems. *CIRP Annals, 62*(1), 503-506. doi:10.1016/j.cirp.2013.03.100

Archenti, A., & Nicolescu, M. (2017). A top-down equivalent stiffness approach for prediction of deviation sources in machine tool joints. *CIRP Annals, 66*(1), 487-490. doi:10.1016/j.cirp.2017.04.066

Archenti, A., Nicolescu, M., Casterman, G., & Hjelm, S. (2012). A new method for circular testing of machine tools under loaded condition. *Fifth Cirp Conference on High Performance Cutting 2012, 1*, 575-580. doi:10.1016/j.procir.2012.05.002

Aslan, D., & Altintas, Y. (2018). Prediction of Cutting Forces in Five-Axis Milling Using Feed Drive Current Measurements. *IEEE/ASME Transactions on Mechatronics, 23*(2), 833-844. doi:10.1109/tmech.2018.2804859

Atsushi Matsubara, T. F., Iwao Yamaji, and Soichi Ibaraki. (2008). MEASUREMENT OF SPINDLE STIFFNESS FOR THE MONITORING SYSTEM OF CUTTING. *Proceedings of 2008 ISFA*, 1-4.

Atsushi Matsubara, T. F., Iwao Yamaji, and Soichi Ibaraki (2008). MEASUREMENT OF SPINDLE STIFFNESS FOR THE MONITORING SYSTEM OF CUTTING FORCES. *ASME*, 4.

Beglarzadeh, B., Mayer, J. R. R., & Archenti, A. (2021). Modelling and indirect measurement of machine tool equivalent joint compliances. *CIRP Journal of Manufacturing Science and Technology, 35*, 882-895. doi:10.1016/j.cirpj.2021.10.001

Bryan, J. B. (1982). A simple method for testing measuring machines and machine tools. *Precision Engineering, 4*(2), 61-69.

Chang, Y., Ding, J., He, Z., Shehzad, A., Ding, Y., Lu, H., . . . Chen, Y. (2020). Effect of joint interfacial contact stiffness on structural dynamics of ultra-precision machine tool. *International Journal of Machine Tools and Manufacture, 158*. doi:10.1016/j.ijmachtools.2020.103609

Craig, J. J. (2005). *Introduction to Robotics, Mechanics, and Control*. Pearson Prentice Hall.

David Te-Yen Huang, J.-J. L. (2001). On obtaining machine tool stiffness by CAE techniques. *International Journal of Machine Tools and Manufacture, 41*, 1149-1163.

Denkena, B., Bergmann, B., & Witt, M. (2021). Feeling Machine for Process Monitoring of Components with Stock Allowance. *Machines, 9*(3). doi:10.3390/machines9030053

Denkena, B., & Boujnah, H. (2018). Feeling machines for online detection and compensation of tool deflection in milling. *CIRP Annals, 67*(1), 423-426. doi:10.1016/j.cirp.2018.04.110

Denkena, B., Dahlmann, D., & Boujnah, H. (2016). Sensory Workpieces for Process Monitoring – An Approach. *Procedia Technology, 26*, 129-135. doi:10.1016/j.protcy.2016.08.018

Denkena, B., Litwinski, K. M., & Boujnah, H. (2014). Process Monitoring with a Force Sensitive Axis-slide for Machine Tools. *Procedia Technology, 15*, 416-423. doi:10.1016/j.protcy.2014.09.096

Evans, C. J., Hocken, R. J., & Estler, W. T. (1996). Self-Calibration: Reversal, Redundancy, Error Separation, and 'Absolute Testing'. *CIRP Annals, 45*(2), 617-634. doi:10.1016/s0007-8506(07)60515-0

G. Zhang, R. Veale, T. Charlton, B. Borchardt, & Hocken, R. (1985). Error Compensation of Coordinate Measuring Machines. *CIRP Annals, Volume 34*(1), 445-448.

Gao, X., Li, B., Hong, J., & Guo, J. (2016). Stiffness modeling of machine tools based on machining space analysis. *The International Journal of Advanced Manufacturing Technology, 86*(5-8), 2093-2106. doi:10.1007/s00170-015-8336-z

H Asada, & JJE Slotine. (1986). *Robot analysis and control*. New York: Wiley.

International Organization for Standardization. (2005). ISO 230_4, Test code for machine tools — part 4: Circular tests for numerically controlled machine tools. In.

International Organization for Standardization. (2012). ISO 230-1, Test code for machine tools — part 1: Geometric accuracy of machines operating under no-load or quasi-static conditions. In.

International Organization for Standardization. (2014). ISO 3290-1, Rolling bearings- Balls- Part 1: Steel balls. In.

International Organization for Standardization. (2017). ISO 1101, Geometrical product specifications (GPS)-Geometrical tolerancing-Tolerances of form, orientation, location, and run-out. In.

Jiang, Z., Huang, M., Tang, X., Song, B., & Guo, Y. (2021). Elasto-geometrical calibration of six-DOF serial robots using multiple identification models. *Mechanism and Machine Theory, 157*. doi:10.1016/j.mechmachtheory.2020.104211

Joint Committee for Guides in Metrology. Evaluation of measurement data: Guide to the expression of uncertainty in measurement. International Bureau of Weightsand Measures; 2008.

Kono, D., Inagaki, T., Matsubara, A., & Yamaji, I. (2012). *Measurement of contact stiffness for stiffness estimation of machine tool supports.* Paper presented at the Key Engineering Materials.

Kono, D., Inagaki, T., Matsubara, A., & Yamaji, I. (2013). Stiffness model of machine tool supports using contact stiffness. *Precision Engineering, 37*(3), 650-657. doi:10.1016/j.precisioneng.2013.01.010

Kono, D., & Matsubara, A. (2016). Investigation on Direction Dependency of Tool-Workpiece Compliance of Machine Tool. *Procedia CIRP, 46*, 529-532. doi:10.1016/j.procir.2016.03.134

Kono, D., Moriya, Y., & Matsubara, A. (2017). Influence of rotary axis on tool-workpiece loop compliance for five-axis machine tools. *Precision Engineering, 49*, 278-286. doi:10.1016/j.precisioneng.2017.02.016

Kono, D., Nishio, S., Yamaji, I., & Matsubara, A. (2015). A method for stiffness tuning of machine tool supports considering contact stiffness. *International Journal of Machine Tools and Manufacture, 90*, 50-59. doi:10.1016/j.ijmachtools.2015.01.001

Laboratory, R. s. A. T. (2018). Measurement of Machine Tool Static Stiffness. Retrieved from http://www.rcmt.cvut.cz/zkuslab/en/text/36

Laspas, T., Theissen, N., & Archenti, A. (2020). Novel methodology for the measurement and identification for quasi-static stiffness of five-axis machine tools. *Precision Engineering, 65*, 164-170. doi:10.1016/j.precisioneng.2020.06.006

Li, B., Hong, J., & Liu, Z. (2014). Stiffness design of machine tool structures by a biologically inspired topology optimization method. *International Journal of Machine Tools and Manufacture, 84*, 33-44. doi:10.1016/j.ijmachtools.2014.03.005

M. Ebrahimi, R. W. (2000). Analysis, modeling, and simulation of stiffness in machine tool drives. *Computers & Industrial Engineering, 38*.

Majda, P., & Jastrzębska, J. (2021). Measurement uncertainty of generalized stiffness of machine tools. *Measurement, 170*. doi:10.1016/j.measurement.2020.108692

Matsubara, A., Sawamura, R., Asano, K., & Muraki, T. (2014). Non-contact Measurement of Dynamic Stiffness of Rotating Spindle. *Procedia CIRP, 14*, 484-487. doi:10.1016/j.procir.2014.03.012

Matsubara, A., Yamazaki, T., & Ikenaga, S. (2013). Non-contact measurement of spindle stiffness by using magnetic loading device. *International Journal of Machine Tools and Manufacture, 71*, 20-25. doi:10.1016/j.ijmachtools.2013.04.003

Nikolas Theissen, T. L., Károly Szipka, Andreas Archenti. (2018). *Virtual machining simulator: analysis of machine tool accuracy.* Paper presented at the 8th Swedish Production Symposium, SPS 2018, Stockholm, Sweden.

Olvera, D., de Lacalle, L. N. L., Compeán, F. I., Fz-Valdivielso, A., Lamikiz, A., & Campa, F. J. (2011). Analysis of the tool tip radial stiffness of turn-milling centers. *The International Journal of Advanced Manufacturing Technology, 60*(9-12), 883-891. doi:10.1007/s00170-011-3645-3

Pawełko, P., Jastrzębski, D., Parus, A., & Jastrzębska, J. (2021). A new measurement system to determine stiffness distribution in machine tool workspace. *Archives of Civil and Mechanical Engineering, 21*(2). doi:10.1007/s43452-021-00206-6

Portman, V. (2000). Deterministic metrology of platform-type machine tools. *International Journal of Machine Tools and Manufacture, 40*, 1423-1442.

Portman, V. (2008). Stiffness Evaluation of Machines and Robots_ Minimum Collinear Stiffness Value Approach. *Proceedings of the 9th Biennial ASME Conference on Engineering Systems Design and Analysis*, 1-8.

Portman, V. T., Chapsky, V. S., Shneor, Y., & Ayalon, E. (2015). Machine Stiffness Rating: Characterization and Evaluation in Design Stage. *Procedia CIRP, 36*, 111-116. doi:10.1016/j.procir.2015.01.080

Portman, V. T., Shneor, Y., Chapsky, V. S., & Shapiro, A. (2014). Form-shaping function theory expansion: stiffness model of multi-axis machines. *The International Journal of Advanced Manufacturing Technology, 76*(5-8), 1063-1078. doi:10.1007/s00170-014-6261-1

Rahmani, M., & Bleicher, F. (2016). Experimental and Analytical Investigations on Normal and Angular Stiffness of Linear Guides in Manufacturing Systems. *Procedia CIRP, 41*, 795-800. doi:10.1016/j.procir.2015.12.033

Renishaw Ball bar 20 software. (2018).

Rivin, E. I. (2010). *Handbook on Stiffness and Damping in Mechanical Design*. Three Park Avenue, New York, NY 10016, USA: ASME.

Rong Yan, F. P., Bin Li. (2008). A Method of General Stiffness Modeling for Multi-axis Machine Tool. *ICIRA, Part II, LNAI 5315*, 1013-1021.

Salgado, M. A., de Lacalle, L. N. L., Lamikiz, A., Munoa, J., & Sanchez, J. A. (2005). Evaluation of the stiffness chain on the deflection of end-mills under cutting forces. *International Journal of Machine Tools & Manufacture, 45*(6), 727-739. doi:10.1016/j.ijmachtools.2004.08.023

Sarhan, A. A. D., & Matsubara, A. (2015). Investigation about the characterization of machine tool spindle stiffness for intelligent CNC end milling. *Robotics and Computer-Integrated Manufacturing, 34*, 133-139. doi:10.1016/j.rcim.2014.12.001

Sawamura, R., Ikenaga, S., & Matsubara, A. (2012). Development of Dynamic Loading Device for Rotating Spindle of Machine Tools. In Key Engineering Materials (Vols. 523–524, pp. 544–549). Trans Tech Publications, Ltd. https://doi.org/10.4028/www.scientific.net/kem.523-524.544.

Shi, Y., Zhao, X., Zhang, H., Nie, Y., & Zhang, D. (2015). A new top-down design method for the stiffness of precision machine tools. *The International Journal of Advanced Manufacturing Technology, 83*(9-12), 1887-1904. doi:10.1007/s00170-015-7705-y

Shneor, Y., & Portman, V. T. (2010). Stiffness of 5-axis machines with serial, parallel, and hybrid kinematics: Evaluation and comparison. *CIRP Annals, 59*(1), 409-412. doi:10.1016/j.cirp.2010.03.020

Simodrive 611 / Masterdrives mc / 1FT6 synchronous motors. (2005). In: Simense

Stejskal, P. D. a. T. (2020). Analytical and Experimental Research of Machine Tool Accuracy. In Ľ. Š. a. J. Marek (Ed.), *Machine Tools*. IntechOpen.

Stejskal, T., Dovica, M., Svetlik, J., & Demec, P. (2019). Experimental assessment of the static stiffness of machine parts and structures by changing the magnitude of the hysteresis as a function of loading. *Open Engineering, 9*(1), 655-659. doi:10.1515/eng-2019-0078

Stejskal, T., Melko, J., Rjabušin, A., Fedorko, G., Hatala, M., & Molnár, V. (2019). Specific principles of work area stiffness measurement applied to a modern three-axis milling machine. *The International Journal of Advanced Manufacturing Technology, 102*(5-8), 2541-2554. doi:10.1007/s00170-019-03393-y

Stejskal, T., Svetlík, J., Dovica, M., Demeč, P., & Kráľ, J. (2017). Measurement of Static Stiffness after Motion on a Three-Axis CNC Milling Table. *Applied Sciences, 8*(1), 15. doi:10.3390/app8010015

Szipka, K., Laspas, T., & Archenti, A. (2017). Mechanistic Approach for the Evaluation of Machine Tools Quasi-Static Capability. 229-243. doi:10.1007/978-3-319-56430-2_16

Szipka, K., Laspas, T., & Archenti, A. (2018). Measurement and analysis of machine tool errors under quasi-static and loaded conditions. *Precision Engineering, 51*, 59-67. doi:10.1016/j.precisioneng.2017.07.011

Taku YAMAZAKI, A. M., Tomaya FUJITA, Toshiyuki MURAKI, Kohei ASANO, Kazuyuki KAWASHIMA. (2010). Measurement of Spindle Rigidity by using a magnet loader. *Journal of Advanced Mechanical Design, Systems, and Manufacturing, 4*(5), 985-994. doi:10.1299/jamdsm.4.985]

Theissen, N., Laspas, T., Cedergren, S., & Archenti, A. (2021). Measurement for the identification of static and quasi-static rotational stiffness. *Precision Engineering, 72*, 215-223. doi:10.1016/j.precisioneng.2021.04.011

Theissen, N. A., Gonzalez, M., Laspas, T., Archenti, A. (2021). *Measurement and identification of dynamic translational stiffness matrix on machine tools under static preloads*. Paper presented at the European Society for Precision Engineering and Nanotechnology.

Uriarte, L., Herrero, A., Zatarain, M., Santiso, G., Lopéz de Lacalle, L. N., Lamikiz, A., & Albizuri, J. (2007). Error budget and stiffness chain assessment in a micromilling machine equipped with tools less than 0.3mm in diameter. *Precision Engineering, 31*(1), 1-12. doi:10.1016/j.precisioneng.2005.11.010

Vrtiel, Š., Hajdu, Š., & Behúlová, M. (2017). Analysis of the machine frame stiffness using numerical simulation. *IOP Conference Series: Materials Science and Engineering, 266*, 012015. doi:10.1088/1757-899x/266/1/012015

W.J. Lee, & Kim, S. l. (2009). Joint Stiffness Identification of an Ultra-Precision Machine for Machining Large-Surface Micro-Features. *International Journal of Precision Engineering and Manufacturing, 10*(5), 115-121.

Wang, B., Zuo, J., & Wang, M. (2011). Analysis and Compensation of Stiffness in Cnc Machine Tool Feed System. *Journal of Advanced Manufacturing Systems, 10*(01), 77-84. doi:10.1142/s0219686711002004

Y. Kakino, Y.Ihara, Y. Nakatsu, & Okamura, K. (1987). The Measurement of Motion Errors of NC Machine Tools and Diagnosis of their Origins by Using Telescoping Magnetic Ball Bar Method. *CIRP Annals*.

Y. Kakino, Y. I., A. Shinohara. (1993). *Accuracy Inspection of NC Machine Tools by Double Ball Bar Method*. Japan: Hanser Pub Inc

Yamazaki, T., Matsubara, A., & Ikenaga, S. (2012). Measurement of Rigidity Change of Preload Switching Spindle. *International Journal of Automation Technology, 6*(2), 175-179. doi:10.20965/ijat.2012.p0175

Yan Rong, P. F., Chen Wei, Yang Jianzhong, Linsen. (2010). Closed-Loop Stiffness Modeling and Stiffness Performance Analysis for Multi-axis Process System. *ICIRA, Part II, LNAI 6425*, 754-765.

Zoran PANDILOV, V. D. (2010). STATIC AND DYNAMIC STIFFNESS OF CNC MACHINE TOOL SERVO DRIVES. *Journal of Machine Engineering, 10*(4), 106-114.